



Master's thesis
Your Field

Formation of Cores by Merging Supermassive Black Holes

Joonas Suortti

December 24, 2019

Tutor: prof. Peter Johansson

Censors: prof. Peter Johansson
doc. Smythe

UNIVERSITY OF HELSINKI
DEPARTMENT OF PHYSICS

PL 64 (Gustaf Hällströmin katu 2)
00560 Helsingin yliopisto

“Bachelor’s degrees make pretty good placemats if you get them laminated.”

—Jeph Jacques

Tiedekunta — Fakultet — Faculty	Laitos — Institution — Department			
Faculty of Science	Department of Physics			
Tekijä — Författare — Author				
Joonas Suortti				
Työn nimi — Arbetets titel — Title				
Formation of Cores by Merging Supermassive Black Holes				
Oppiaine — Läroämne — Subject				
Your Field				
Työn laji — Arbetets art — Level	Aika — Datum — Month and year	Sivumäärä — Sidoantal — Number of pages		
Master's thesis	December 24, 2019	0 pages		
Tiivistelmä — Referat — Abstract				
Abstract goes here.				
Avainsanat — Nyckelord — Keywords				
Your keywords here				
Säilytyspaikka — Förvaringsställe — Where deposited				
Muita tietoja — övriga uppgifter — Additional information				

Contents

1	Introduction	1
2	Background Theory	2
2.1	Elliptical Galaxies	2
2.1.1	Basic Properties and Classification	2
2.1.2	Photometry	3
2.1.3	Kinematics	5
2.1.4	Formation Models	7
2.2	Core Galaxies	10
2.3	Core Formation Through Black Hole Mergers	12
2.3.1	Dynamical Friction	12
2.3.2	Three-Body Interactions	14
2.3.3	Gravitational Radiation	15
2.3.4	The Final-Parsec Problem	16
2.3.5	Observational Evidence for Core Formation Through SMBH Mergers	17
2.3.6	Black Hole Scaling Relations	18
2.4	Integral-Field Spectroscopy	20
2.4.1	Slow and Fast Rotators	22
2.5	Galactic Dynamics	24
2.5.1	Collisional And Collisionless Systems	24
2.5.2	Potential-Density Models	25
2.6	Regularisation	26
2.7	Post-Newtonian Dynamics	29
3	KETJU	32
3.1	Direct Summation and Tree Codes	32
3.2	Softened Dynamics	35

3.3	AR-CHAIN	37
3.3.1	Algorithmic Regularisation	37
3.3.2	Chained Coordinate System	40
3.3.3	Velocity Dependent PN-Corrections	42
3.3.4	Gragg-Bulirsch-Stoer Extrapolation	43
3.4	Basic Properties of KETJU	44
3.4.1	The Chain Subsystem	45
3.4.2	Perturbative Effects of the Perturber and Tree Particles	47
3.4.3	Particle Mergers	48
3.4.4	Incorporating AR-CHAIN in the GADGET-3 Leapfrog	49
4	Simulating Core Formation Using KETJU	51
4.1	Simulation Details	51
4.2	Core Size Measurements	56
4.3	Velocity Anisotropy	64
4.4	Line-of-Sight Kinematics	67
4.4.1	2D Kinematic Maps	67
4.4.2	The λ_R -parameter	72
4.5	Comparison to Observations	74
5	Conclusions	78
	Bibliography	80

1. Introduction

2. Background Theory

2.1 Elliptical Galaxies

2.1.1 Basic Properties and Classification

Nearly all massive galaxies are elliptical galaxies (Es), which are stellar systems characterised by their ellipsoidal shape, lack of a rapidly rotating disk, and their small or essentially almost non-existent content of cool gas and dust. Furthermore, due to the absence of star formation caused by the lack of dust and cool gas, the stellar population of elliptical galaxies is generally quite old, with a mean age of $\gtrsim 10$ Gyr (Mo et al., 2010). This correlates well with their observed red colours (Cappellari, 2016), as galactic spectra tend to become redder with age.

Elliptical galaxies are included in the Hubble classification of galaxies (Hubble, 1926). In the Hubble "tuning-fork diagram" (figure 2.1), they are located left of the point where the sequence diverges into the two spiral galaxy paths. This means that alongside lenticular galaxies, which are transitional objects between elliptical and spiral galaxies, elliptical galaxies are so-called "early-type galaxies" (ETGs). ETGs are, in fact, often defined simply as galaxies that do not contain spiral arms.

In the Hubble classification, elliptical galaxies are further divided into seven different subcategories according to their observed apparent ellipticity. These categories range from E0 to E7, where the number denotes the ellipticity of the galaxy multiplied by ten and rounded to the nearest integer. The ellipticity of a galaxy is simply the measure of how flattened an observed 2D-projection of a ellipsoidal stellar system is. It can be calculated using the equation:

$$\epsilon = 1 - \frac{b}{a}, \quad (2.1)$$

where a and b are the semi-major and semi-minor axes of a luminosity isophote (i.e. constant luminosity or surface brightness contour), respectively. The larger the ellipticity, the flatter the system ($\epsilon = 0$ denotes a completely spherical galaxy). It

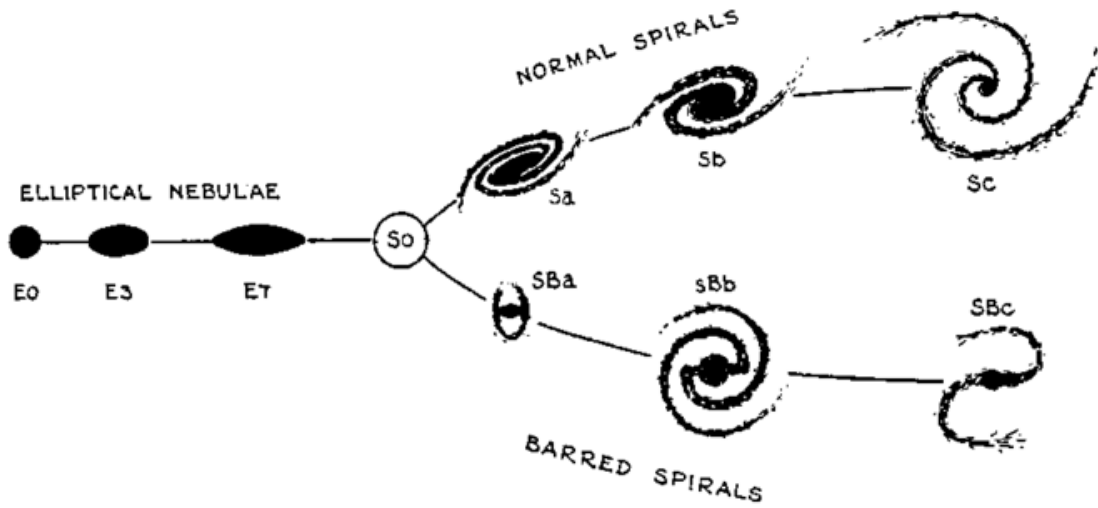


Figure 2.1: The Hubble tuning-fork diagram. The image is originally from Hubble (1936).

is important to note, however, that the ellipticity of a system can depend on the specific isophote from which it is calculated. Since the isophotes of elliptical galaxies generally become flatter the farther they are located from the galactic centre (Binney & Tremaine, 2008), this could result in a single galaxy having multiple ellipticities. To remedy this, the Hubble classification uses the ellipticity at the effective radius (R_e) to determine the subcategory of an elliptical galaxy. The effective radius is the radius of a sphere that encloses half of the total luminosity of the galaxy. Since galaxies do not have clearly defined boundaries, R_e is also often used as a measure of their size.

2.1.2 Photometry

The photometric properties of elliptical galaxies are often described in terms of the surface brightness, which describes the amount of observed luminosity from a unit area. Thus, an important property for studying the general spatial distribution of stellar material in observed elliptical galaxies, is the one-dimensional radial surface brightness profile $I(R)$, where R is the projected distance from the centre of the galaxy. In practice, these profiles can be constructed by calculating the azimuthal averages of the observed surface brightness at every projected radius R (Merritt, 2013).

The observed surface brightness profiles of elliptical galaxies are typically smooth and featureless, declining smoothly as the projected radius grows, until the galaxy is indistinguishable from the background (Binney & Tremaine, 2008).

The observed "power-law"-like profiles are quite similar in shape across all elliptical galaxies, which has led to the formulation of a multitude of models that attempt to describe this general shape. An early example of such a model is the "de Vaucouleurs" power-law profile: $I \propto R^{1/4}$ (de Vaucouleurs, 1948). This model, however, is quite simple, and only represents well the profiles of some elliptical galaxies, namely the bright ellipticals (Merritt, 2013).

Compared to the de Vaucoulers-profile, a more robust and more commonly used model is the Sérsic-profile (Sérsic, 1968):

$$I(R) = I_e \exp\{-b_n [(R/R_e)^{1/n}]\}, \quad (2.2)$$

where R is again the projected distance from the galactic centre, I_e is the surface brightness at the effective radius, n is the so-called Sérsic index ($n = 4$ gives a Sérsic profile which is identical to the de Vaucouleurs profile), and b_n is a shape factor, which is defined so that a circular area with a radius of R_e contains half of the total luminosity of the galaxy. The value for the shape factor can be approximated as $b_n \approx 2n - 0.324$, when $1 \lesssim n \lesssim 10$ (Binney & Tremaine, 2008).

The prominent use of the Sérsic-profile is due to the fact, that it describes the observed surface brightness profiles of many different elliptical galaxies very well for a large range of radii (Merritt, 2013). However, when extrapolated to the central regions of galaxies, the profile often deviates from the observations. The galactic cores either contain "missing" or "extra" light, corresponding to what are often called "cored" or "cuspy" central surface brightness profiles, respectively (e.g. Kormendy et al., 2009).

Whether the central surface brightness profile of an elliptical galaxy is a shallow "cored" profile or a steep "cuspy" profile is seemingly tied to the absolute magnitude of the galaxy. Typically, bright ellipticals ($\mathcal{M}_V \lesssim -22$) have central profiles with missing light, while fainter galaxies ($-22 \lesssim \mathcal{M}_V \lesssim -16$) contain extra light at their centres (Kormendy et al., 2009).

This supposed dichotomy between the brighter and fainter ellipticals also extends to the isophotal shapes of the galaxies. Usually the shapes of the isophotes of elliptical galaxies deviate from exact ellipses, as the brighter ellipticals contain so-called "boxy" isophotes, while the isophotes of the fainter galaxies are typically more "disky" (an illustration of the two isophotal shapes can be seen in figure 2.2) (Mo et al., 2010). Whether the shapes of the isophotes are "boxy" or "disky", can be determined from the Fourier-series of the deviations of the observed isophotes from

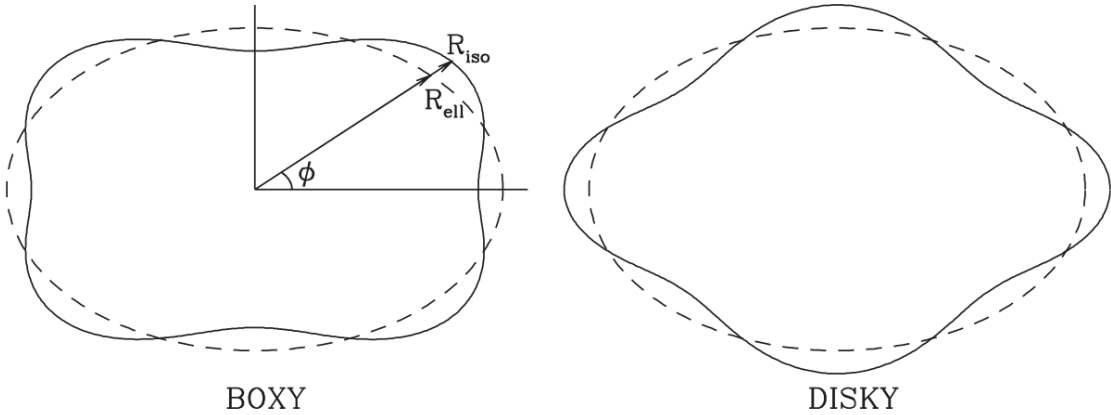


Figure 2.2: A comparison between the isophotal shapes of "boxy" and "disky" galaxies. The solid curves denote the respective isophotal shape, while the dashed lines denote their best-fit ellipses. The markings on top of the picture of the "boxy" isophote illustrate the procedure described by equation 2.3. The figure is adapted from Mo et al. (2010).

their respective best-fit ellipses, which is described by the following formula:

$$\Delta(\phi) = R_{\text{iso}}(\phi) - R_{\text{ell}}(\phi) = a_0 + \sum_{n=1}^{\infty} (a_n \cos(n\phi) + b_n \sin(n\phi)), \quad (2.3)$$

where $R_{\text{iso}}(\phi)$ is the radius of the isophote at the angle ϕ , $R_{\text{ell}}(\phi)$ is the radius of the corresponding perfect ellipse at the same angle, and where a_n and b_n are the Fourier coefficients. If $a_4 < 0$ holds true the isophote is "boxy", and if $a_4 > 0$ holds true the shape of the isophote is deemed "disky".

2.1.3 Kinematics

The divide between bright and faint elliptical galaxies, specified in the previous section, seems to also include the kinematics of the galaxies (discussed in e.g. Mo et al., 2010). The brighter galaxies rotate slowly ($V/\sigma \lesssim 0.1$; where V and σ are the line-of-sight maximum rotational velocity and the velocity dispersion at the centre of the galaxy, respectively), while the rotation of the faint galaxies is faster ($V/\sigma \sim 1$) (Davies et al., 1983; Cappellari et al., 2007). Furthermore, the velocity distributions of the bright "boxy" galaxies are relatively anisotropic, with different degrees of velocity dispersion along their three principal axes, and a large amount of random stellar motion compared to the amount of ordered motion (i.e. small V/σ values). This contrasts with the more isotropic and ordered velocity distributions (thus larger V/σ values) of the fainter and more disk-like galaxies (Kormendy et al., 2009; Krajnović et al., 2008).

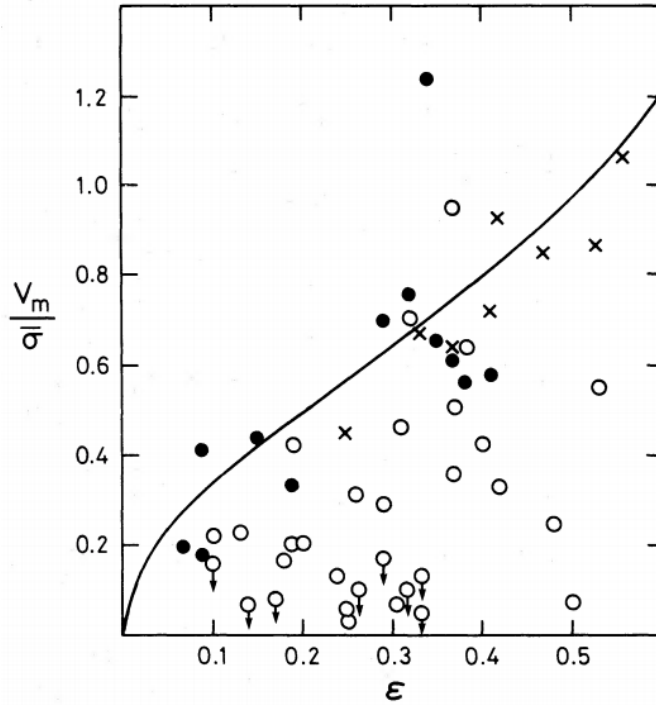


Figure 2.3: Plot of the relation between V/σ and ϵ in observed galaxies. The solid curve is defined by equation 2.4 and shows the expected relation for galaxies with isotropic rotation. The filled circles denote elliptical galaxies with a B -band magnitude of $M_B > -20.5$, while the open circles are for galaxies with $M_B < -20.5$. The crosses stand for bulges of disk galaxies. The figure is originally from Davies et al. (1983).

The more ordered and faster rotation of the fainter galaxies seems to be, at least partly, consistent with rotational flattening. For isotropic rotators, the value of V/σ parameter is expected to approximately follow the equation:

$$\frac{V}{\bar{\sigma}} \approx \sqrt{\frac{\epsilon}{1-\epsilon}}, \quad (2.4)$$

where $\bar{\sigma}$ is the mean velocity dispersion inside half of the effective radius and ϵ is the ellipticity of the galaxy. This gives a relation between the rotation and the expected ellipticity of the galaxy, often noted as the $V/\sigma - \epsilon$ -relation. Figure 2.3 shows the expected $V/\sigma - \epsilon$ relation described by equation 2.4 as a curve, alongside the observed apparent ellipticities and V/σ parameters for elliptical galaxies with a B -band magnitude of either $M_B > -20.5$ (filled circles) or $M_B < -20.5$ (open circles) (Davies et al., 1983). By looking at the figure, it is clear that, when compared to the brighter galaxies, the fainter galaxies are, in general, situated closer to the curve describing the expected relation. This implies that, unlike the boxy bright ellipticals, the fainter disk-like ellipticals are flattened by rotation. The generally weaker

flattening of the brighter galaxies is then usually attributed to their anisotropic velocity distributions, as the galaxy is more extended along the axes where the velocity dispersion is larger.

A further distinction between the bright and relatively faint ellipticals can be drawn from their gravitational potentials. While the "disky" galaxies are assumed to be axisymmetric, with an ellipsoidal shape containing two identical-length semi-principal axes ($A = B \neq C$); the "boxy" galaxies seem to be triaxial, with all of their semi-principal axes having different lengths ($A \neq B \neq C$) (Mo et al., 2010).

The triaxial potential of the bright ellipticals can be identified from the fact, that unlike the fainter ellipticals, bright Es often contain kinematic misalignments, meaning that the position angle of their projected kinematic axis differs from their photometric minor axis. According to Mo et al. (2010), these misalignments can arise as a result of two different effects. A kinematic misalignment might be caused by, a misalignment between the projected and the apparent observed minor axes of the galaxy, which is common for triaxial galaxies due to their asymmetric shape. On the other hand, the deviation in the position angles might also be the result of the observed galaxy having intrinsically misaligned angular momentum, which would be a natural consequence of triaxial potentials supporting rotation around all three axes. Both of these effects require the host galaxy to be triaxial.

Depending on the shape of its gravitational potential, galaxies support different kinds of orbits. Axisymmetric potentials support both so-called tube-orbits, which are orbits that trace a ring-like volume around the axis-of-symmetry; and the cone-shaped saucer-orbits (Merritt, 2013). Triaxial galaxies support at least four different types of orbits, models of which can be seen in figure 2.4. Similarly to axisymmetric potentials these include tube orbits, though in the case of a triaxial potential, they can trace a volume around either the short axis, inner long axis or outer long axis. The fourth orbital type is the box-orbit, which is an orbit that fills a rectangular volume. Stars on box-orbits can move through the centre of the galaxy, and are often the dominant stellar component in triaxial potential models, giving the "boxy" galaxies their characteristic shape (Binney & Tremaine, 2008).

2.1.4 Formation Models

There are two main models for the formation of elliptical galaxies: the monolithic collapse scenario and the merger scenario (Mo et al., 2010). In the monolithic collapse scenario, elliptical galaxies are formed through the collapse and stabilization of some initial condition, which results in the simultaneous formation of the stellar

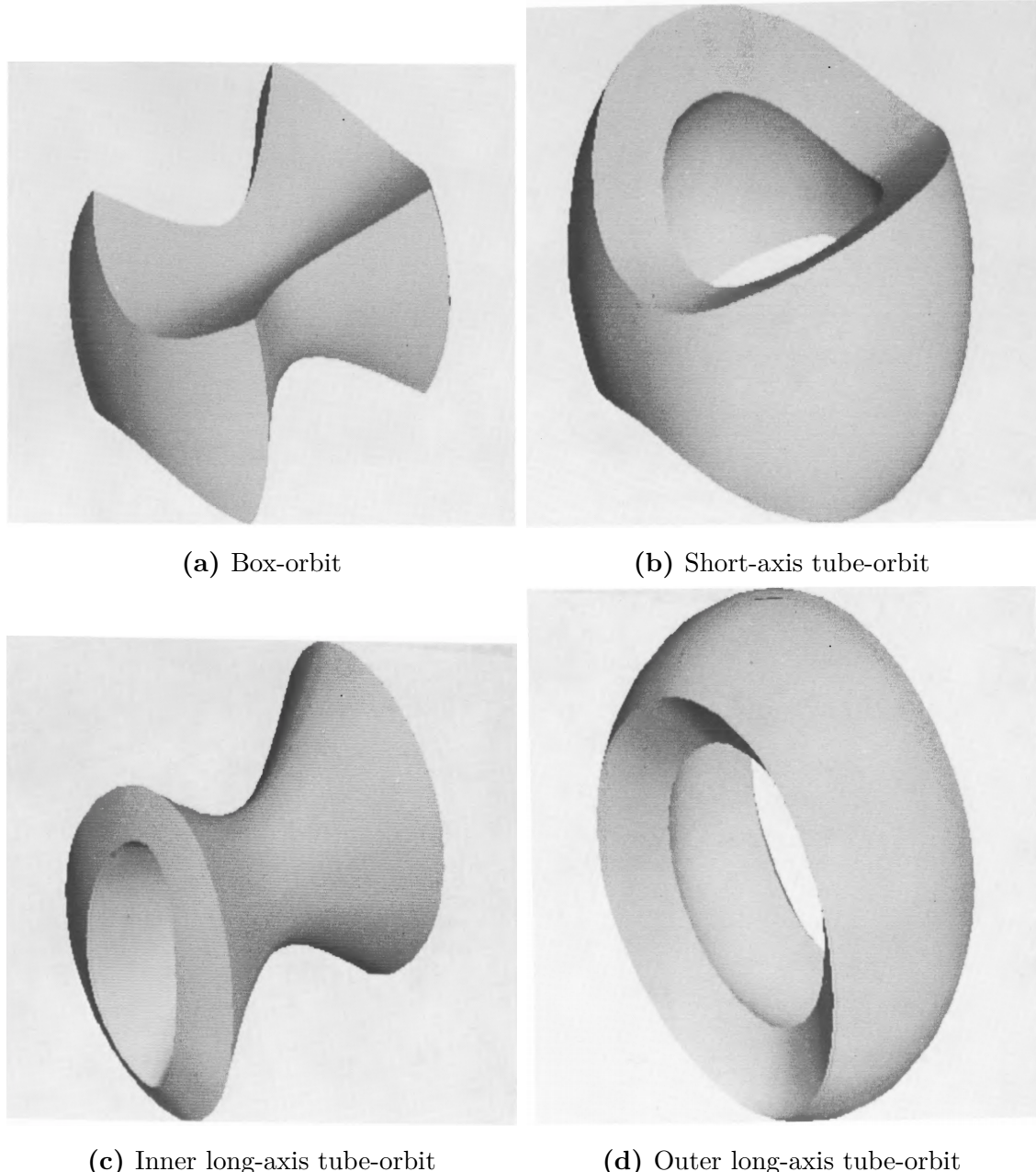


Figure 2.4: Models of the different types of orbits in triaxial potential. The figures are from Statler (1987).

material and the assembly of the galaxy. This collapse can either be "dissipative" or "dissipationless". In a dissipative process the system loses some of its total energy through radiation, while in a dissipationless process the total energy is conserved. In the context of galaxy formation through monolithic collapse, an example of a dissipative process would be, the collapse of some initial condition that contains a gaseous component which turns in to stars as it collapses. A dissipationless collapse then usually necessitates the lack of gaseous components in the initial conditions.

Assuming that the collapse in the monolithic collapse scenario is dissipative, the model in question is able to reproduce several features observed in actual ellipticals, such as the fact that, the ratio of dark matter to baryonic matter is smaller in the centre of the galaxy than in the outer regions (Mo et al., 2010). However, the main problem of the monolithic collapse scenario is that it is not compatible with the current paradigm that expects a Λ *CDM* cosmology for the universe.

The cold dark matter (CDM) cosmology assumes a hierarchical formation for observed structures, and that star formation and the merging of dark matter halos are still on-going processes. This is in stark contrast to the monolithic collapse scenario, where after the initial collapse, the resulting stellar system evolves mostly passively, without experiencing either major galaxy mergers or star-formation.

The merger scenario, on the other hand, suggests that elliptical galaxies are formed through mergers of two or more pre-existing fully formed galaxies (Mo et al., 2010). Thus, the formation of stars and the assembly of the final galaxy are independent of each other. Since the star formation and the assembly of the galaxy are once again largely independent from each other, even this formation scenario can not be reconciled completely with the Λ *CDM* cosmology.

It has also been suggested that elliptical galaxies are formed through a two-phased mechanism that is a combination of both the monolithic collapse and the merging scenarios (e.g. Oser et al., 2010). According to this model, the stellar material in elliptical galaxies is initially (redshift $2 \lesssim z \lesssim 6$) accumulated through dissipative 'in-situ' formation of stars caused by cold gas flows, a process similar to the 'monolithic collapse' scenario. Afterwards ($z \lesssim 3$), the elliptical galaxies are expected to grow as a result of both minor and major galaxy mergers (i.e. the accumulated stars are formed 'ex-situ').

The formation models which include galaxy mergers seem to be more representative of the actual mechanism from which elliptical galaxies have been formed. Thus, the existence of the observed photometric and kinematic dichotomy between the "core" and "cusp" galaxies has been interpreted as differences in their respective

merger progenitor galaxies. Though there are multiple properties that can affect the rotational velocity of the merger remnant (such as the ratio between the masses of the galaxy progenitors in a merger; Naab & Burkert 2003), the dichotomy is usually attributed to the existence of dissipative components in the merging galaxies (Mo et al., 2010).

The fainter Es with "cuspy" central surface brightness profiles are generally thought to have been formed through dissipative mergers of gas-rich progenitor galaxies. In a gas-rich galaxy merger, the gas is expected to accumulate in the centre of the merger remnant galaxy, driven by tidal perturbations during the merger, and resulting in a starburst event (Barnes & Hernquist, 1991). This would account for the extra-light seen in the surface brightness profiles of the faint galaxies (Hopkins et al., 2008), and would deepen the central gravitational potential well, causing the remnant galaxy's velocity dispersion to rise in the core regions (Barnes & Hernquist, 1996). The central accumulation of gas and the subsequent starburst event would also cause the gravitational potential of the galaxy to become more axisymmetric. As box-orbits can only occur in triaxial-potentials, this would cause these fainter elliptical galaxies to have their characteristic disk-like shapes (Naab et al., 2006).

In contrast, the formation mechanism for the "core" galaxies is that of dissipationless "dry" mergers. The formation of massive slowly rotating galaxies is assumed to be a two-stage process, similar to the model proposed by Oser et al. (2010). Initially, the accumulation of stellar mass in "core" galaxies is driven by rapid "in-situ" star formation caused by inflows of cold gas; and afterwards, during redshift $3 > z > 0$, their growth in mass is dominated by major gas-poor ETG mergers (Naab et al., 2009). Since the massive galaxies in major galaxy mergers are expected to contain central supermassive black holes (SMBHs), it is often proposed that the "cores" in the bright ellipticals are a result of a scouring process, where the central binary black hole coalesces and ejects stellar material from the centre of the merger remnant in complex three-body interactions.

2.2 Core Galaxies

While the basic principle of core galaxies being galaxies with "missing" light at their centre is easy to grasp, giving an explicit definition for what exactly constitutes a core galaxy is somewhat more challenging. Core galaxies have been defined as both, galaxies that contain an observed surface brightness profile, defined similarly to the one described in equation 2.7, with an inner logarithmic slope of $\gamma < 0.3$ (Lauer

et al., 1995, 2007a); and as galaxies that have surface brightness profiles that are a combination of a shallow inner profile and a steep outer profile (Kormendy & Bender, 1999). However, the problem with the definition proposed by Lauer et al. (1995) is that Sérsic galaxies with low values for the Sérsic index n can have shallow inner profiles even when their cores do not contain a light deficit (Graham et al., 2003). Meanwhile, Dullo & Graham (2012) argue that the other definition results in a "disconnect with the curved outer Sérsic profile". Graham et al. (2003) suggest that core galaxies should simply be defined by a deficit in the central surface brightness profile, when compared to the inward extrapolation of the outer Sérsic profile.

The size of the core is an important property of core galaxies, as its relation to the other properties of the observed galaxy can be used to derive information about the formation history of both the galaxy and the core itself. Usually the core size is determined by fitting observed one-dimensional surface brightness profiles with some model profile that is a combination of a shallow inner power-law and a steep outer power-law. The radius at which the outer power-law changes into the inner power-law is called the break radius (r_b), and is commonly equated to the radius of the core.

There are two commonly used options for modelling the surface brightness profiles. The first one is the core-Sérsic profile (Graham et al., 2003), which can be expressed using the following equation:

$$\mu(r) = \mu' \left[1 + \left(\frac{r_b}{r} \right)^\alpha \right]^{\gamma/\alpha} \exp \left\{ -b_n [(r^\alpha + r_b^\alpha) / r_e^\alpha]^{1/(\alpha n)} \right\}, \quad (2.5)$$

where r_b is the break radius, γ is the logarithmic slope of the inner power-law, α controls the sharpness of the transition between the two power-laws, b_n , r_e and n are the shape factor, effective half-mass radius and the Sérsic index of the outer Sérsic profile respectively, and the normalization factor μ' is defined by:

$$\mu' = \mu_b 2^{-\gamma/\alpha} \exp \left[b_n \left(2^{(1/\alpha)} r_b / r_e \right)^{1/n} \right], \quad (2.6)$$

where μ_b is the surface brightness at the break radius.

The second option is to use the so called Nuker profile (Lauer et al., 1995):

$$\mu(r) = 2^{(\beta-\gamma)/\alpha} \mu_b \left(\frac{r_b}{r} \right)^\gamma \left[1 + \left(\frac{r}{r_b} \right)^\alpha \right]^{(\gamma-\beta)/\alpha}, \quad (2.7)$$

where r_b is once again the break radius, μ_b is the surface brightness at the break radius, β and γ are the logarithmic slopes of the power-laws inside and outside of the break radius respectively, and α once again describes the sharpness of the transition between the two slopes.

In addition to the model fitting methods, one could also estimate the size of the core by calculating the so-called "cusp radius" r_γ . The cusp radius is the distance from the centre of the galaxy, at which the logarithmic slope of the surface brightness profile equals $\gamma' = -1/2$ (Carollo et al., 1997; Lauer et al., 2007b). This distance provides an estimate for the location where the inner power-law of the profile changes into the outer power-law, and thus r_γ can be equated to the core radius.

2.3 Core Formation Through Black Hole Mergers

As stated before, currently the leading mechanism for the formation of the cores seen in massive ETGs is the ejection of stellar material due to three-body interactions between stars and binary supermassive black holes during SMBH mergers (e.g. Faber et al., 1997; Milosavljević et al., 2002; Mo et al., 2010). Core formation is expected to occur specifically during "dry" ETG mergers, as, due to the lack of gas, they do not contain merger induced star-formation, which would mask the formation of the low-luminosity core.

There are three different, and potentially overlapping, phases for SMBH mergers: the dynamical friction phase, the three-body interaction phase, and the gravitational wave radiation phase (Merritt, 2013). In each of the three phases, a different process removes kinetic energy and shrinks the separation between the coalescing SMBHs.

2.3.1 Dynamical Friction

During the dynamical friction phase, the relative orbits of the central SMBHs of the merging galaxies shrink, due to a change in their kinetic energies by so-called dynamical friction. Originally proposed by Chandrasekhar (1943), it is argued that stars experience a net decelerating gravitational force when moving through a population of field-stars. As the subject star moves through the stellar population, its gravitational influence causes the relative trajectories of nearby field-stars to curve behind it. This causes the concentration of mass to become larger behind the subject star than in front of it. The now asymmetric distribution of mass relative to the subject star, causes the gravitational force opposite to its direction of motion to become stronger than the gravitational force parallel to the motion, resulting in a net decelerating force called dynamical friction. A sketch of this mechanism can be seen in figure 2.5. Alongside stars and other objects made up of baryonic matter,

dark matter also contributes to dynamical friction.

Dynamical friction also applies to the central SMBHs in galaxy mergers, while they move through the stellar population and dark matter halo of the galaxy merging with their host galaxy. Dynamical friction is initially the main mechanism which shrinks the orbits of the SMBHs, causing them to sink into the centre of the galaxy merger. The strength of the dynamical friction force induced onto the SMBHs can be described by the following equation (Binney & Tremaine, 2008):

$$F_{\text{DF}} = M \frac{d\mathbf{v}_\bullet}{dt} = -4\pi G^2 M^2 m \ln \Lambda \int d^3 \mathbf{v}_a f(\mathbf{v}_a) \frac{\mathbf{v}_\bullet - \mathbf{v}_a}{|\mathbf{v}_\bullet - \mathbf{v}_a|^3}, \quad (2.8)$$

where M and \mathbf{v}_\bullet are the mass and velocity of the SMBH, respectively; m and \mathbf{v}_a are the mass and velocity of a field-particle; $f(\mathbf{v}_a)$ is the phase space density (see section 2.5.1) of the field-particles; and $\ln \Lambda$ is described by the equation $\ln \Lambda \simeq \ln \left(\frac{b_{\max}}{b_{90}} \right)$, with b_{\max} and b_{90} being the maximum length and the 90° reflection impact parameters, respectively.

As can be seen from equation 2.8, the strength of the dynamical friction force scales with the mass of the SMBH as $F_{\text{DF}} \propto M^2$. This shows that the time it takes for an object to fall to the centre of a stellar system as a result of a dynamical friction driven inspiral, is dependent on the mass of said object. Thus, in galaxy mergers, only objects that have a large enough mass, such as SMBHs, can fall to the centre of the merger and form cores through three-body interactions. For example, globular clusters, which are old gas-free stellar systems with masses of $M \sim 10^5 M_\odot$ (Binney & Tremaine, 2008), can still be seen orbiting around the nucleus of the Milky Way, implying that the time-scale for their inspiral is longer than the age of the Milky Way.

The effects of dynamical friction continue until the black holes form a so-called "hard binary", which is defined as a binary system with a binding energy that is larger than the kinetic energy of the field stars (Binney & Tremaine, 2008). The formation of a "hard binary" occurs when the relative velocities of the binary black holes become much larger than the velocity dispersion of the surrounding stars. This, in turn, occurs when the coalescing black holes reach a separation of:

$$a = \frac{G\mu}{4\sigma}, \quad (2.9)$$

where μ is the reduced mass defined as: $\mu = M_1 M_2 / (M_1 + M_2)$, where M_1 and M_2 are the masses of the SMBHs; and σ is the velocity dispersion of the surrounding stars (Merritt, 2013).

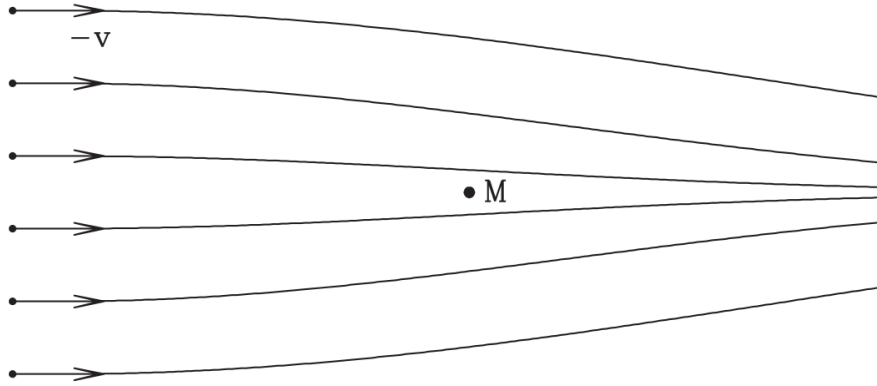


Figure 2.5: A depiction of dynamical friction. The point denoted as M depicts the object moving through the population of field-stars. The smaller dots and the lines are the field-stars and their trajectories, respectively. The arrows depict the velocity ($-v$) of the stars in relation to the mass M . The figure is adapted from Mo et al. (2010).

2.3.2 Three-Body Interactions

The three-body interaction phase of the SMBH merger is the phase that is assumed to cause the actual formation of the core. It starts once the smaller SMBH falls inside the gravitational sphere-of-influence (SOI) of the more massive black hole, resulting in an SMBH binary (Merritt, 2013). The SOI of an SMBH is the spherical region in space, where the gravitational force of the SMBH dominates over the force of the surrounding stars, and which encompasses an amount of stellar mass equivalent to the mass of the black hole. If the velocity dispersion (σ) of the stars near an SMBH is known, the size of the SOI can be determined by comparing σ to the velocity of a circular orbit around the SMBH, giving the following formula for the influence radius (Merritt, 2013):

$$r_{\text{SOI}} \equiv \frac{GM_\bullet}{\sigma^2} \approx 10.8 \left(\frac{M_\bullet}{10^8 M_\odot} \right) \left(\frac{\sigma}{200 \text{ km s}^{-1}} \right)^{-2} \text{ pc}, \quad (2.10)$$

where G is the gravitational constant, and M_\bullet is the mass of the black hole.

During the three-body interaction phase, the orbital energy of the binary is reduced in interactions between the binary and field-stars. Stars that are able to interact strongly with the SMBH binary, can be ejected at high speeds in a "gravitational slingshot" event. The growth in the kinetic energy of the ejected stars happens at the expense of the orbital energy of the SMBH binary, causing the orbit of the binary to shrink. Which stars have a strong enough interaction with the SMBH binary is determined by the loss-cone, a region in phase space (see the *Galactic Dynamics* section for the explanation of phase space) where the angular momentum

of a star fulfils the following condition:

$$L \lesssim [G(M_1 + M_2)a]^{1/2}, \quad (2.11)$$

where M_1 and M_2 are the masses of the binary SMBHs, and a is the semi-major axis of their orbit (Binney & Tremaine, 2008).

2.3.3 Gravitational Radiation

Once the three-body interactions with field-stars have shrunk the orbit of the binary enough, and the separation of the SMBHs has become less than:

$$a = \left\{ \frac{64}{5} \frac{G^3 M_1 M_2 (M_1 + M_2) F(e)}{c^5} \right\}^{1/4}, \quad (2.12)$$

where G is the gravitational constant, M_1 and M_2 are the masses of the black holes, c is the speed of light, and $F(e)$ is an eccentricity-dependent factor; gravitational radiation in the form of gravitational waves becomes a significant factor in the evolution of the binary. This marks the start of the gravitational wave radiation phase of the SMBH merger evolution.

The orbital energy of the binary is radiated away in the form of gravitational waves, causing the semi-major axis of the binary orbit to become smaller. Since the strength of the gravitational radiation is largest when the separation between the SMBHs is at its smallest, the most significant reduction to the kinetic energies of the black holes occurs near the pericentre of the binary orbit. The asymmetry in the decrease of the kinetic energy between the pericentre and the apocentre of the orbit, causes its eccentricity to decrease and start to converge at 0. This effect is analogous to the procedure used to circularise the orbits of satellites, where their orbital motion is decelerated near the pericentre. Due to the decrease in its velocity, the satellite is unable to climb as far out in the gravitational well of the central body as it used to, which causes the distance between the pericentre and apocentre of its orbit to be reduced, resulting in a smaller eccentricity.

In the case of post-Newtonian dynamics (post-Newtonian dynamics is discussed in greater detail in section 2.7) taking into account PN-terms valid at 2.5PN, these changes in the semi-major axis and the eccentricity of the binary orbit, occur at the rates of (Peters, 1964):

$$\left\langle \frac{da}{dt} \right\rangle = -\frac{64}{5} \frac{G^3 M_1 M_2 (M_1 + M_2)}{c^5 a^3 (1 - e^2)^{7/2}} \left(1 + \frac{73}{24} e^2 + \frac{37}{96} e^4 \right), \quad (2.13)$$

and:

$$\left\langle \frac{de}{dt} \right\rangle = -\frac{304}{15} e \frac{G^3 M_1 M_2 (M_1 + M_2)}{c^5 a^4 (1 - e^2)^{5/2}} \left(1 + \frac{121}{304} e^2 \right), \quad (2.14)$$

respectively, when averaged over the orbital period.,

Once enough gravitational energy has been radiated, and the orbit of the black holes has shrunk sufficiently, the SMBHs merge, forming a single black hole. The time it takes for gravitational radiation to cause the coalescence of an SMBH binary, can be calculated using the following equation (Merritt, 2013):

$$t_{\text{gr}} \approx 6 \times 10^6 \frac{(1+q)^2}{q} \left(\frac{a}{0.01 \text{ pc}} \right)^4 \left(\frac{M_1 + M_2}{10^8 M_\odot} \right)^{-3} (1 - e^2)^{7/2} \text{ yr}, \quad (2.15)$$

where $q \equiv M_2/M_1 \leq 1$. This shows that the efficiency of the final SMBH merger phase depends heavily on the separation between the black holes in the binary ($t_{\text{gr}} \propto a^4$), as well as the eccentricity of the binary orbit ($t_{\text{gr}} \propto (1 - e^2)^{7/2}$).

2.3.4 The Final-Parsec Problem

The fact that the gravitational radiation driven coalescence is effective only at very small binary SMBH separations, could provide a problem for the existence of actual SMBH mergers. When the SMBH binaries form at the centres of the galaxies their separation is usually ~ 1 pc. As equation 2.15 shows, assuming that the SMBH masses are $\sim 10^8 M_\odot$, and that the binary orbit is circular ($e = 0$, which is admittedly unrealistic, as the SMBH merger orbits are highly elliptical during most of the merger), the black holes would coalesce in a time-scale far longer than the age of the Universe (the age of the Universe is ~ 13.4 Gyr). Whether three-body interactions can sufficiently decrease the initial binary separation in order for the gravitational radiation driven coalescence to become efficient, is not certain. As seen in equation 2.11, the size of the loss-cone shrinks as the orbit of the binary becomes smaller. This leads to the problem where, both due to its shrinking size and the ejection of mass from the loss-cone, the number of stars that can interact strongly with the binary becomes so small, that the three-body interaction driven coalescence of the SMBHs effectively ceases. This is called "the final parsec problem" (Milosavljević & Merritt, 2003).

Several mechanisms, which attempt to reconcile the "final parsec problem" by "rep populating" the loss-cone, have been proposed. These work by supplying the loss-cone with additional stars that can be ejected, further shrinking the orbit of the binary. One such mechanism is the repopulation of the loss-cone due to two-body relaxation. However, this has been found to be too inefficient, as the relaxation

time scales inside the SOI of the central SMBHs seem to be $\sim 10^{11}$ yr in almost all galaxies, which is larger than the Hubble time (~ 14 Gyr; Faber et al. 1997; Milosavljević & Merritt 2001). Another proposed repopulation mechanism is the secondary slingshot; where the initial interaction between the binary and an orbiting star only moves the star into another bound orbit, from which it may interact with the binary once more (Merritt, 2013). It is also possible that the triaxial geometry of massive elliptical galaxies could account for the repopulation of the loss-cone. Torques resulting from the non-spherical gravitational potential in triaxial galaxies can change the angular momentum of stars, potentially causing some stars outside of the loss-cone to be included in the loss-cone regime (Merritt, 2013; Gualandris et al., 2017). Through simulations, Gualandris et al. (2017) have shown that this "collisionless orbit diffusion" can account for the repopulation of the loss-cone, and they even conclude that: "there is no 'final parsec problem'".

2.3.5 Observational Evidence for Core Formation Through SMBH Mergers

Whether the cores of the galaxies actually form through black hole mergers, depends on how probable the occurrence of these kind of events is. The observed empirical relation between the mass of a central SMBH and the velocity dispersion of its host galaxy (see equation 2.17), has shown that all massive galaxies have supermassive black holes in their centres. Thus, a merger of two massive galaxies would undoubtedly contain two SMBHs.

There have also been some direct observational evidence for SMBH binaries occurring in the centres of galaxies. For example, Rodriguez et al. (2006) observed two active galactic nuclei (AGN) with a projected separation of ~ 7.3 pc in the galaxy NGC 6240. Since AGN are powered by accretion of material onto supermassive black holes, and since the total mass of these supposed BHs in NGC 6240 is $\sim 1.5 \times 10^8 M_\odot$, both of the AGN are inside their gravitational influence radius, and the SMBHs would thus be considered to be a binary. The presence of an SMBH binary has also been observed in the active galaxy OJ 287, where the periodical optical variety of the AGN has been attributed to a smaller SMBH passing through the accretion disk of the larger active black hole (Merritt, 2013).

As for the existence of black hole mergers, recent gravitational wave observations performed using the *Laser Interferometer Gravitational-Wave Observatory* (LIGO, Abbott et al. 2016, 2019), provide unequivocal evidence that at least stellar-

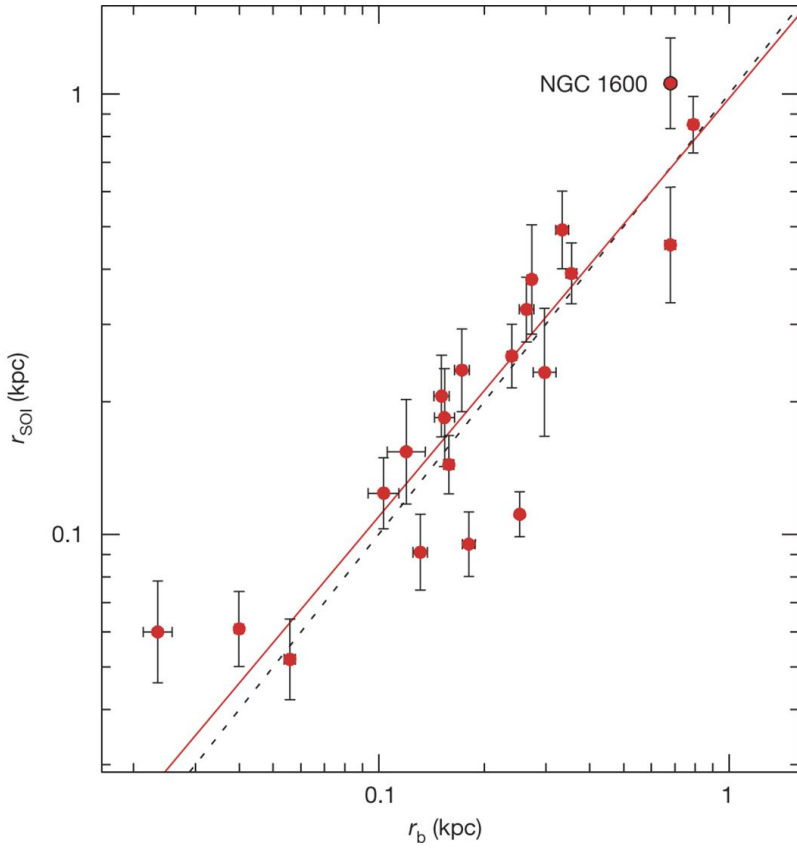


Figure 2.6: Plots of the $M_{\bullet} - r_b$ relation from equation 2.16, alongside the observed data from which the relation has been deduced. The original figure is from Thomas et al. (2016).

mass black hole mergers can occur. Though SMBH mergers have yet to be observed, the fact that black hole mergers have been shown to exist, alongside the aforementioned binary SMBH observations, greatly supports the idea that merging supermassive black holes could play a part in the evolution of some galaxies. Furthermore, taking account the fact that our current cosmological paradigm expects galaxies to have been formed through hierarchical mergers of galaxies, and that all merger progenitor galaxies most likely already contain a central SMBH, it stands to reason that binary SMBHs should exist at some point in most galaxies. Thus, the rarity of binary SMBH observations implies that SMBH mergers are taking place.

2.3.6 Black Hole Scaling Relations

The observed sizes of low-luminosity cores have been found to correlate with the mass of the central SMBH of the galaxy. Both simulations and observations have shown that a relation between the central SMBH mass (M_{\bullet}) and the quantity of the observed mass deficit (M_{def}) exists (Graham, 2004; Merritt, 2006; Dullo & Graham,

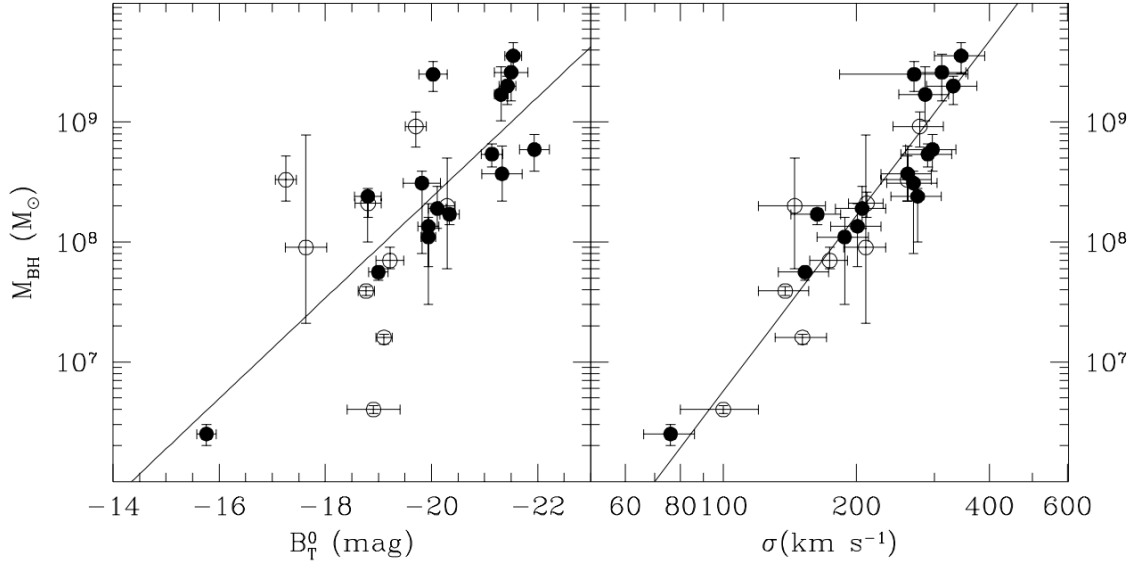


Figure 2.7: Plots of both the $M_\bullet - L_{\text{B,bulge}}$ (left) and $M_\bullet - \sigma$ (right) relations, as given by Ferrarese & Ford (2005). The luminosity is given in B-magnitudes in the plot of the $M_\bullet - L_{\text{B,bulge}}$ relation, and the relation itself differs somewhat from the one described in equation 2.18. The open circles denote observations from the bulges of spiral galaxies, and the filled circles denote observations from elliptical galaxies. The figures are originally from Ferrarese & Ford (2005).

2014). Furthermore, there seems to be a relation between the mass of the SMBH and the radius of the depleted core. Thomas et al. (2016), for example, derive the following scaling relation from observed core sizes and central black hole mass measurements:

$$\log_{10} \left(\frac{M_\bullet}{M_\odot} \right) = (1.17 \pm 0.14) \log_{10} \left(\frac{r_b}{\text{kpc}} \right) + (10.27 \pm 0.51). \quad (2.16)$$

Figure 2.6 shows this relation alongside observed values for the core radius and the corresponding central black hole mass. While there seems to be quite a bit of scatter between the modelled relation and the observed values, the mass of the central SMBH seems to be connected to the properties of the core. Furthermore, similar relations have been observed by, for example, Dullo & Graham (2012).

Though not necessarily proving that the formation of the central SMBH is connected to the development of the core; further evidence that the central black hole is inherently linked to the properties of its host galaxy can be seen in the three main scaling relations of the SMBH mass. These relations include the $M_\bullet - \sigma$ relation (Ferrarese & Ford, 2005):

$$\frac{M_\bullet}{10^8 M_\odot} = (1.66 \pm 0.24) \left(\frac{\sigma}{200 \text{ km s}^{-1}} \right)^{(4.86 \pm 0.43)}, \quad (2.17)$$

where σ is the velocity dispersion; the $M_\bullet - L_{\text{bulge}}$ relation (Marconi & Hunt, 2003):

$$\log_{10} \left(\frac{M_\bullet}{M_\odot} \right) = (1.13 \pm 0.12) \log_{10} \left(\frac{L_{K,\text{bulge}}}{L_{K,\odot}} \right) + (8.21 \pm 0.07), \quad (2.18)$$

where $L_{K,\text{bulge}}$ is the luminosity of the galactic bulge in K -band magnitudes; and the $M_\bullet - M_{\text{bulge}}$ relation (Marconi & Hunt, 2003):

$$\log_{10} \left(\frac{M_\bullet}{M_\odot} \right) = (0.96 \pm 0.07) \log_{10} \left(\frac{M_{\text{bulge}}}{M_\odot} \right) + (8.28 \pm 0.06), \quad (2.19)$$

where M_{bulge} is the mass of the central bulge. Plots for these three relations can be seen in figures 2.7 and 2.8.

The above relations have often been used as evidence for the coevolution of the central black holes and their host galaxies. SMBHs are expected to gather most of their mass through the accretion of gas (Soltan, 1982). However, this gas accretion causes radiative and kinetic feedback-effects in the form of radiation from the accretion disk and outflows formed from the accreted material, respectively. The strength of the feedback is dependent on the gas accretion rate, and as a consequence, the mass of the accreting black hole. If the SMBH is massive enough, the energy released through the feedback-effects can overcome the binding energy ($E_{\text{bulge}} \approx M_{\text{bulge}} \sigma^2$; e.g. Fabian 2012) of the galactic bulge, sweeping away the interstellar gas from the bulge, thus effectively stopping star formation, and further mass accretion by the black hole. Since the binding energy of the bulge is dependent on the mass and the velocity dispersion of the bulge, it is implied that this kind of a self-regulating process could result in the $M_\bullet - \sigma$ and $M_\bullet - M_{\text{bulge}}$ relations. The $M_\bullet - L_{\text{bulge}}$ relation would then naturally arise as a consequence of the bulge-mass relation.

2.4 Integral-Field Spectroscopy

Integral-field spectroscopy (IFS) has become an essential part of studying the kinematic properties of ETGs, as it allows for the spatial analysis of galactic spectra. IFS is done using instruments called "integral-field units", which, in principle, calculate the spectrum of the observed light for each pixel. However, often the signal-to-noise ratio (S/N) of singular pixels is quite poor. To improve the S/N , the pixel measurements are usually combined into so-called "spaxels" (i.e. spatial pixels) using an algorithm, such as the Voronoi-tessellation algorithm (Cappellari & Copin, 2003). This results in IFU-maps similar to figure 2.9.

By creating a histogram out of the observed velocities in the pixels forming a spaxel, the spaxels can show the line-of-sight velocity distribution (LOSVD) of the

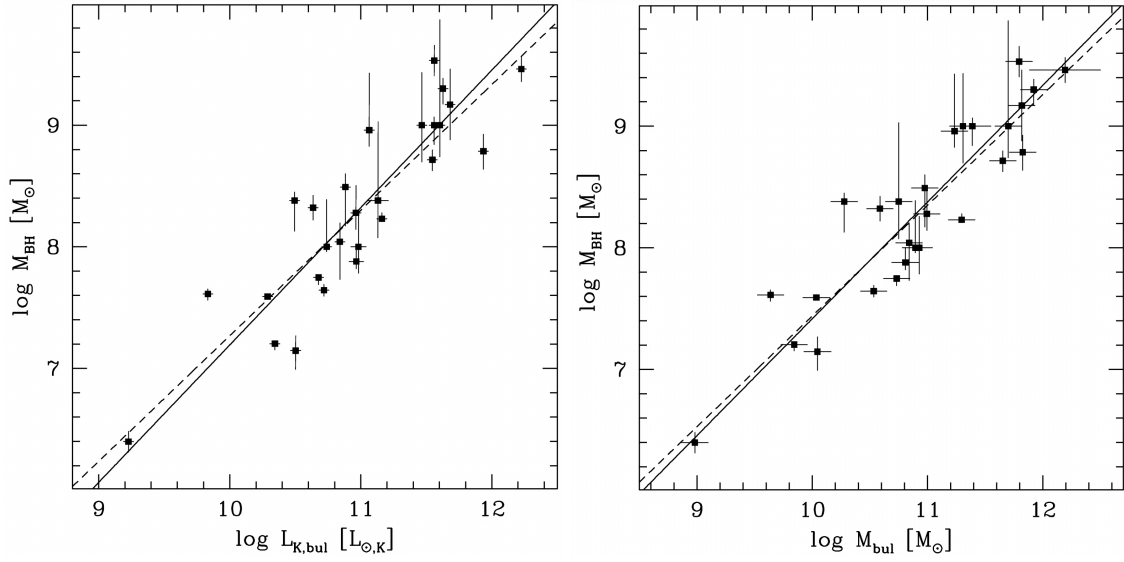


Figure 2.8: Plots of both the $M_{\bullet} - L_{K,\text{bulge}}$ (left) and $M_{\bullet} - M_{\text{bulge}}$ (right) relations, with the observed data. The solid lines describe the relations given by equations 2.18 and 2.19. The dashed lines are simple "least-squares" fits. The figures are adapted from Marconi & Hunt (2003).

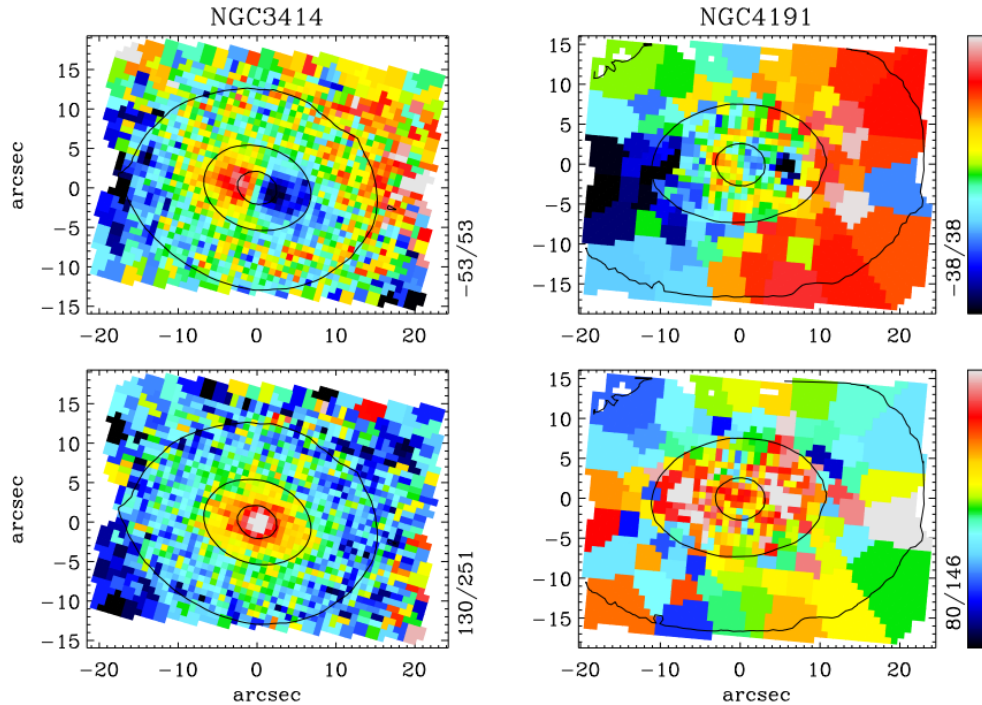


Figure 2.9: IFU-maps of the mean line-of-sight velocities (top figures) and line-of-sight velocity dispersions (bottom figures) from the galaxies NGC 3414 and NGC 4191. The figures are adapted from Krajnović et al. (2011).

regions in the observed galaxy that they encompass. The analysis of the LOSVDs is done by fitting the velocity histogram with some theoretical distribution function. Since the LOSVDs are similar to a Gaussian distribution function but rarely purely Gaussian (Mo et al., 2010), quite often (e.g. the SAURON and ATLAS^{3D} projects, as well as the MASSIVE survey; Bacon et al. 2001; Cappellari et al. 2011; Ma et al. 2014) the fitted distribution function is in the form of the modified Gaussian function (van der Marel & Franx, 1993; Bender et al., 1994):

$$f(v) = I_0 e^{-\gamma^2/2} (1 + h_3 H_3(y) + h_4 H_4(y)), \quad (2.20)$$

where I_0 is a normalization constant, γ is the central slope of the particle density profile, $y = (v - V_{\text{avg}})/\sigma$, and H_3 and H_4 are the third and fourth order Hermite polynomials respectively:

$$H_3(y) = (2\sqrt{2}y^3 - 3\sqrt{2}y) / \sqrt{6}, \quad (2.21)$$

$$H_4(y) = (4y^4 - 12y^2 + 3) / \sqrt{24}. \quad (2.22)$$

The four remaining parameters: the average LOS velocity V_{avg} , the LOS velocity dispersion σ , and the third and fourth order Gauss-Hermite moments h_3 and h_4 , which represent skewness and kurtosis respectively, are usually the parameters that are of interest.

By using IFS, a number of different kinematic features have been observed in ETGs. These features include: areas with low-level velocities or disk-like rotation, as well as regions where the kinematic axis of the galaxy is misaligned with its photometric axis (Emsellem et al., 2007). IFS has also helped identify so-called *Kinematically Distinct Cores* (KDCs), which are central regions of galaxies with an angular momentum that has a different direction compared to the rest of its host. There has also been evidence of *Counter Rotating Cores* (CRCs), which are galactic cores that have a difference of around 180° in the position angle of their angular momentum vector, when compared to their immediate surroundings (Krajnović et al., 2011).

2.4.1 Slow and Fast Rotators

Using LOSVD measurements done with IFS, Emsellem et al. (2007) have defined an explicit way to classify galaxies as either slow or fast rotators. The basis for this classification is the λ_R parameter, which describes the angular momentum of a galaxy, and is defined as:

$$\lambda_R \equiv \frac{\langle R|V| \rangle}{\langle R\sqrt{V^2 + \sigma^2} \rangle}, \quad (2.23)$$

where R is the projected distance from the galactic centre, V is the line-of-sight velocity, σ is the velocity dispersion and $\langle \rangle$ denote that the nominator and denominator in the equation are luminosity weighted means. From binned 2D kinematic maps, such as the ones given by IFS observations, this property can be calculated using the following formula:

$$\lambda_R = \frac{\sum_{i=1}^{N_p} F_i R_i |V_i|}{\sum_{i=1}^{N_p} F_i R_i \sqrt{V_i^2 + \sigma_i^2}}, \quad (2.24)$$

where F_i , R_i , V_i and σ_i are the flux, projected distance from the galaxy centre, velocity and velocity dispersion of the i th bin, and N_p is the number of bins.

Determining whether a galaxy is a fast or a slow rotator using λ_R , is done by comparing the value that the parameter gets at the galaxy's effective radius, to some pre-defined threshold. The originally used threshold is: $\lambda_{Re} < 0.1$, where λ_{Re} is the aforementioned λ_R at the effective radius, and where galaxies fulfilling this condition are classified as slow rotators (Emsellem et al., 2007). A revision of the threshold by Emsellem et al. (2011) takes the ellipticity (ϵ) of the galaxy into account, and defines slow rotators as having $\lambda_{Re} < 0.31\sqrt{\epsilon}$, which accounts for the increased anisotropy in the kinematics of flatter galaxies. An even further refinement of the slow rotator definition has been proposed by Cappellari (2016), where slow rotator galaxies are determined using the following two criteria: $\lambda_{Re} < 0.08 + \epsilon/4$ and $\epsilon < 0.4$. The former criterion of the threshold reduces the risk of misidentifying very round non-regular slow rotators as fast rotators, while the latter makes sure that only sufficiently round galaxies are classified as slow rotators (Cappellari 2016 argues that "genuine" disk-less slow rotators are all rounder than $\epsilon = 0.4$).

Slow rotator galaxies, when defined using the above methods, often contain a KDC, and usually exhibit: anisotropic velocity distributions, little to no large-scale rotation, kinematic misalignments and twists (Emsellem et al., 2007; Cappellari et al., 2007). In contrast, the velocity distributions of fast rotators are isotropic and their kinematic axis is aligned closely with their photometric axis (Emsellem et al., 2007). They also have disk-like kinematics and nearly oblate shapes (Cappellari et al., 2007).

As expected, the dichotomy between slow and fast rotators clearly mirrors the kinematic differences between "boxy" and "disky" ellipticals. This implies that the cored and cuspy galaxies should follow the slow and fast rotator divide as well. Krajnović et al. (2013) find that this indeed does seem to be the case, however there are a few exceptions. Nevertheless, even when accounting for these exceptions, Cappellari (2016) for example, consider the agreement to be good enough, that it

is possible to adequately draw conclusions about the photometry or kinematics of these galaxies.

2.5 Galactic Dynamics

2.5.1 Collisional And Collisionless Systems

The motion of stars in stellar systems is caused by gravitational forces. However, due to the long-range nature of gravity, in large systems with a very large number of stars, the stellar motion is dominated by the gravitational influence of the large number of far-away stars instead of a few strong close encounters. For this reason, when modelling such a system, it is often appropriate to ignore the changes to their orbits caused by specific stellar encounters, and simply approximate their motion as being caused by a smooth continuous gravitational potential. Systems where this approximation is applicable are called "collisionless systems", whereas systems where the modelling of the stellar motion requires knowledge about the gravitational effects caused by distinct massive particles, are called "collisional systems".

A stellar system can be approximated as collisionless if its "relaxation time" is significantly longer than its age. The relaxation time is defined as the time it takes, for the cumulative effect of encounters between a subject star and multiple field stars, to change the orbit of the subject star in such a significant way, that its initial conditions can not be inferred from its current motion. This process is often called "two-body relaxation". The relaxation time of a system can be calculated using the following formula (Binney & Tremaine, 2008):

$$t_{\text{relax}} \simeq \frac{0.1N}{\ln N} t_{\text{cross}}, \quad (2.25)$$

where N is the number of particles in the system, and t_{cross} is the crossing time, which is defined as the time it takes for a typical field-star to cross the system once, and the value of which can be estimated using the radius of the system R and the typical field-star velocity v as $t_{\text{cross}} = R/v$. The relaxation times of galaxies are generally much longer than the age of the Universe (~ 13.8 Gyr). For example, the relaxation time of the solar neighbourhood is $t_{\text{relax}} \simeq 6 \times 10^{14}$ yr. Thus, approximating galaxies as collisionless systems is a valid assumption.

Of specific interest to collisionless systems is the concept of "phase space", as it allows one to model the general motion in stellar systems while neglecting the calculation of the motion of distinct stars. Phase space itself is a six-dimensional

space, where, in addition to the three basic Cartesian position coordinates (x, y, z) , the possible states of a system are described by three velocity coordinates (v_x, v_y, v_z) . If all stars in a system have identical masses, these six dimensions can describe every dynamical state that a star can have, and thus the state of the whole stellar system at a certain time t can be described using the stellar distribution function $f(\mathbf{x}, \mathbf{v}, t)$, which is also known as the phase space density.

In collisionless systems, stellar trajectories are smooth and continuous, making the motion of stars analogous to flowing fluid. Much like how the mass density of a fluid is conserved along the flow, the phase space density $f(\mathbf{x}, \mathbf{v}, t)$ is conserved around a star moving in the phase space. This means that the time-dependent behaviour of the system can be modelled using the "collisionless Boltzmann equation" (Merritt, 2013):

$$\frac{\partial f}{\partial t} + \mathbf{v} \cdot \nabla f - \nabla \phi \cdot \frac{\partial f}{\partial \mathbf{v}} = 0, \quad (2.26)$$

where ϕ is the gravitational potential of the system. By integrating this equation over velocity, it is possible to derive equations which relate the gravitational potential of the stellar system to its moments of velocity distribution. These moments are statistical properties that can often be measured from observations. Thus, by using equation 2.26, one can model the gravitational potential of a galaxy, without the knowledge of specific stellar orbits, from observations of the general stellar dynamics of a galaxy.

2.5.2 Potential-Density Models

When using the "collisionless system"-approximation to model a stellar system, knowledge about its gravitational potential is fundamental. If the mass-density distribution of the galaxy is known, the corresponding potential can be calculated from the Poisson's equation (Binney & Tremaine, 2008):

$$\nabla^2 \phi = 4\pi G \rho, \quad (2.27)$$

where ϕ is the gravitational potential, G is the gravitational constant, and ρ is the aforementioned mass-density distribution. Different types of galaxies can, of course, have different mass distributions, which leads us to the so-called "potential-density models". These models describe galaxies using different density distributions, and then calculate their corresponding gravitational potential using the Poisson's equation. The initial mass-density distribution in the models is often derived in such a way that it is able to account for properties observed in actual galaxies (e.g. the Dehnen model described below).

One of the most popular potential-density models used when approximating elliptical galaxies, is the spherically symmetric Dehnen-model (Dehnen, 1993), which is defined as:

$$\rho(r) = \frac{(3-\gamma)M}{4\pi} \frac{a}{r^\gamma(r+a)^{4-\gamma}}, \quad (2.28)$$

$$\phi(r) = \frac{GM}{a} \times \begin{cases} -\frac{1}{2-\gamma} \left[1 - \left(\frac{r}{r+a} \right)^{2-\gamma} \right] & \gamma \neq 2 \\ \ln \frac{r}{r+a} & \gamma = 2 \end{cases}, \quad (2.29)$$

where M is the total mass, a is the scaling radius, and γ is the central slope of the profile. There are a few reasons why this model in particular is used often. Firstly, the density profile is a combination of two power-laws. This is similar to many observed luminosity and surface brightness profiles in Es (see section 2.1.2), and also many simulated dark-matter profiles (Binney & Tremaine, 2008). Furthermore, when projected, the outer parts of the density profile resembles the empirical "de Vaucouleurs" surface brightness profile. The model is also a generalization of two other commonly used potential-density models, namely the Jaffe-model and the Hernquist-model (for these models $\gamma = 2$ and $\gamma = 1$ respectively Jaffe, 1983; Hernquist, 1990).

2.6 Regularisation

The nature of elliptical galaxy mergers and the formation of merger remnants with cores deficient in light, is such, that simulations of the process must take into account strong interactions between stars and black holes. This leads to a common issue encountered in simulations of collisional systems, namely the singularity at $r = 0$ in the equation of motion (Binney & Tremaine, 2008):

$$\ddot{r} = -GM/r^2, \quad (2.30)$$

where G is the gravitational constant, M is the total mass of the two interacting particles, and r is the distance between the particles. Often, when calculating the orbits of stars, these simulations maintain accuracy by reducing the integration time-step when the accelerations of the objects become large. On extremely close encounters, the singularity in equation 2.30 causes the accelerations of the objects to rise sharply, resulting in smaller and smaller time steps, effectively stopping the simulation from progressing.

The solution to the above issue is so-called regularisation, where the singularity in the equation of motion (equation 2.30) is removed through a coordinate transformation. Two examples of such transformations are given by Binney & Tremaine (2008).

The first example is the "Burdet-Heggie regularisation", which changes the simulation time to the fictitious time: $dt = r d\tau$, and adds the external gravitational field \mathbf{g} to the equation of motion. By applying these changes, it is possible to write the two-body equation of motion as:

$$\mathbf{r}'' - 2E_2 \mathbf{r} = -\mathbf{e} + r^2 \mathbf{g}, \quad (2.31)$$

where \mathbf{r}'' is the second derivative of the position \mathbf{r} with respect to the fictitious time τ , E_2 is the energy of the two-body orbit, and \mathbf{e} is the eccentricity vector. Equation 2.31 is similar to the equation of motion of an harmonic oscillator, and unlike equation 2.30, it does not contain a singularity at $r = 0$.

The second example is the "Kustaanheimo-Stiefel" (KS) regularisation, which converts the equation of motion of the two-body problem, into an equation of motion similar to that of a harmonic oscillator, by transforming the three-dimensional spatial coordinates into four-dimensional coordinates. Like the Burdet-Heggie regularisation, KS-regularisation defines a new fictitious time $dt = r d\tau$ and adds the gravitational field of the other particles to the equation of motion. The spatial coordinate transformation is done by changing the position vector $\mathbf{r} = (x, y, z)$ into a corresponding four-vector $\mathbf{u} = (u_1, u_2, u_3, u_4)$, where:

$$\begin{aligned} u_1^2 &= \frac{1}{2}(x + r) \cos^2 \psi \\ u_2^2 &= \frac{yu_1 + zu_4}{x + r} \\ u_3^2 &= \frac{zu_1 + yu_4}{x + r} \\ u_4^2 &= \frac{1}{2}(x + r) \sin^2 \psi, \end{aligned} \quad (2.32)$$

and where ψ is some arbitrary parameter (Binney & Tremaine, 2008). If ϕ_e is the gravitational potential induced outside the particles outside the two-body problem, the equation of motion becomes as follows:

$$\mathbf{u}'' - \frac{1}{2}E\mathbf{u} = -\frac{1}{4}\frac{\partial}{\partial \mathbf{u}}(|\mathbf{u}|^2\phi_e), \quad (2.33)$$

where \mathbf{u}'' denotes the second fictional time derivative of the four-vector, and E is the energy of the two-body orbit when ϕ_e is taken into account:

$$E = \frac{1}{2}v^2 - \frac{GM}{r} + \phi_e = 2\frac{|\mathbf{u}'|^2}{|\mathbf{u}|^2} - \frac{GM}{|\mathbf{u}|^2} + \phi_e. \quad (2.34)$$

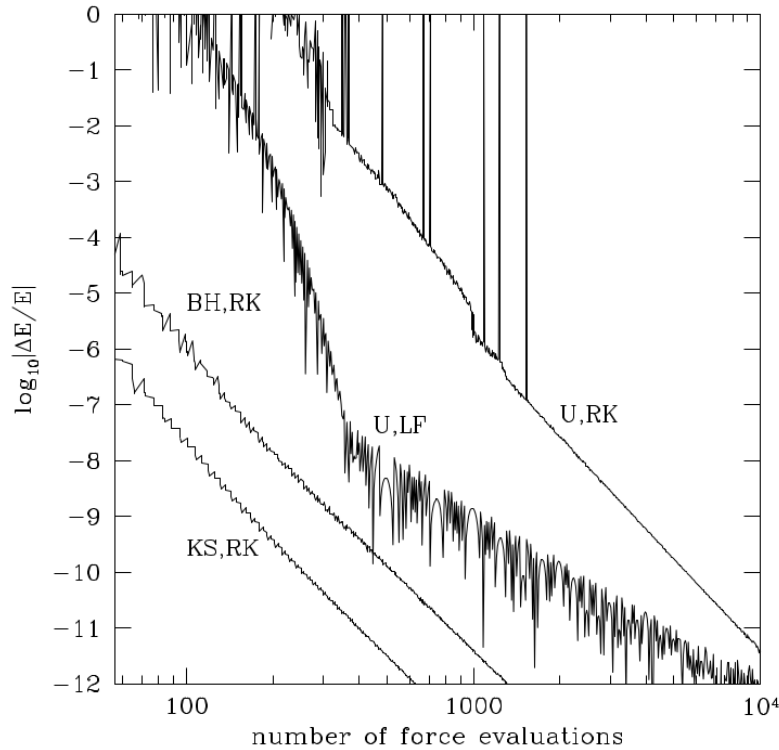


Figure 2.10: Fractional error of the energy of an orbit with an eccentricity of $e = 0.99$, as a function of the number of force calculations per orbit. The errors were calculated after a single pericentre passage of the orbiting object. The multiple graphs denote errors produced by different integrators and regularisation procedures. U , BH and KS denote unregularised, "Burdet-Heggie" and "Kustaaheimo-Stiefel" regularisations, respectively. RK and LF denote "Runge-Kutta" and "Leapfrog" integrators (both defined in chapter 3), respectively. The figure is originally from Binney & Tremaine (2008).

Equation 2.33 is now the equation of motion of a four-dimensional harmonic oscillator with an added external force (Binney & Tremaine, 2008). Furthermore, as the equation in question clearly shows, the regularised form of the equation of motion is well defined even when the new position vector gets the value $\mathbf{u} = 0$, and thus does not contain the same singularity as the basic Cartesian version in equation 2.30. Once this regularised version of the equation of motion has been used to calculate the motion of a particle, its new position in the four-dimensional space can be transferred back to three dimensions using the following relations:

$$\begin{aligned}x &= u_1^2 - u_2^2 - u_3^2 + u_4^2 \\y &= 2(u_1u_2 - u_3u_4) \\z &= 2(u_1u_3 + u_2u_4).\end{aligned}\tag{2.35}$$

Figure 2.10 by Binney & Tremaine (2008) compares the fractional errors in the energies of highly eccentric simulated orbits ($e = 0.99$), integrated in differently regularised (or non-regularised) coordinates, after one pericenter passage. The figure clearly shows how important the removal of the singularity is for the accuracy of the integration of the orbit. In regularized coordinates, the integrators require around an order of magnitude less force evaluations to achieve the same accuracy than in unregularised coordinates. Furthermore, the efficiency of the integration seems to also be affected by the type of regularisation, as the more robust KS-regularisation results in a smaller fractional energy error than the Burdet-Heggie regularisation technique.

2.7 Post-Newtonian Dynamics

When simulating mergers of galaxies that contain central SMBHs, general relativity has to be taken into account, as relativistic effects not only affect the orbits of stars that pass close to the black holes significantly, but are also required for the emission of the gravitational waves that drive the coalescence of the SMBH binary during the final stage of its merger. However, the equations that describe these effects are difficult to solve, and thus inefficient to use in simulations. For example, effects on the motion of particles caused by the distortion of space-time near extremely massive objects, can not be modelled using a fixed linear background or common time-steps between all particles. Due to such complications, the effects caused by general relativity are often approximated using so-called "Post-Newtonian" (PN) dynamics.

PN dynamics is an extension of the basic Newtonian dynamics that approximates the effects that Einstein's general theory of relativity has in the two-body problem, by adding so-called PN-terms to the Newtonian equation of motion. Each term has its own degree, describing increasingly precise relativistic effects. The magnitude of these effects are proportional to the order of $\mathbf{a}_{x\text{PN}} \propto (v^2/c^2)^x$, where x is the degree of the term in question. The resulting equation of motion is similar to:

$$\mathbf{a} = \mathbf{a}_{\text{Newtonian}} + \mathbf{a}_{1\text{PN}} + \mathbf{a}_{2\text{PN}} + \mathbf{a}_{2.5\text{PN}} + \dots, \quad (2.36)$$

where $\mathbf{a}_{\text{Newtonian}}$ is the acceleration from the basic Newtonian equation motion, and $\mathbf{a}_{x\text{PN}}$ are added PN corrections.

Depending on its degree, a PN-term either describes an effect that conserves the energy of the system, or an effect where energy is dissipated through gravitational radiation in the form of gravitational waves (Mora & Will, 2004). Terms that have a degree that is an integer are conservative, while the half-degree terms are radiative and cause the orbit of a two-body system to shrink. For this reason, when simulating black hole mergers, it is imperative to include terms upto at least 2.5PN in the equation of motion.

The actual formulae for the PN-terms are quite long, and are thus not given here. However, they are derived from the expansion of Einstein's equations based on the two approximations that: the objects are assumed to be point masses, and that the equation (Merritt, 2013):

$$\left(\frac{v}{c}\right)^2 \approx \frac{Gm}{c^2r} \ll 1, \quad (2.37)$$

where G is the gravitational constant, c is the speed of light, m is the total mass of the two interacting particles, and v and r are the relative velocity and distance between the particles respectively, holds true. In words, the above equation means that the velocities of the moving objects are assumed to be of the order that is expected for gravitaionally bound systems, and thus significantly slower than the speed of light, and that the objects are never brought near the gravitational radius of one another (Merritt, 2013).

An important caveat to note is that, the point mass assumption of the PN approximation ignores the relativistic effects that the spin of the black hole, alongside its non-spherical shape, has on closely orbiting objects. Thus, in order to take them into account, one needs to add an additional spin PN-term to equation 2.36. The effects caused by the spin of the black hole include orbital precession (i.e. changes in the rotational axis of the orbit), as well as precession of the spin itself (Kidder,

1995). Although a small effect in magnitude, the lack of spherical symmetry in the shape of the spinning BH, on the other hand, results in additional non-radial acceleration for the orbiting object (Merritt, 2013).

3. KETJU

KETJU (Rantala et al., 2017) is a simulation code, designed for efficient and simultaneous modelling of both galactic-scale dynamics and the precise motion of stellar particles near SMBHs. This is achieved through the combined functionality of two integrators with different degrees of efficiency and precision. The global dynamics of the simulated stellar system is calculated using the tree-integrator (section 3.1) of the GADGET-3 simulation code (Springel, 2005), which uses softened dynamics (section 3.2) to calculate the general motion of particles in collisionless systems. The motion of bodies close to the SMBHs is on the other hand calculated using an algorithmically regularised chain method (AR-CHAIN, section 3.3; Mikkola & Merritt 2008).

3.1 Direct Summation and Tree Codes

The simplest way of modelling the gravitational interactions between particles in a system, is to use the "direct summation" method. When using direct summation, the gravitational force acted upon particle α is calculated using the basic Newton's law of gravity:

$$\mathbf{F}_\alpha = \sum_{\beta \neq \alpha} G m_\beta \frac{\mathbf{r}_\beta - \mathbf{r}_\alpha}{|\mathbf{r}_\beta - \mathbf{r}_\alpha|^3}, \quad (3.1)$$

where m_β is the mass of the particle β , and \mathbf{r}_α and \mathbf{r}_β are the vector positions of particles α and β , respectively. Since every particle contributes to the total gravitational force experienced by every other particle, when using this equation to calculate gravitational forces, the number of calculations needed to determine the motion of the entire system scales according to N^2 , where N is the total number of simulated particles. As a result, this method is very inefficient for simulations of systems such as galaxies, which may need millions of particles to adequately describe their internal dynamics. However, similar force-evaluation methods that only scale as $N \ln N$ also exist. One such method, included in GADGET-3 and used in the

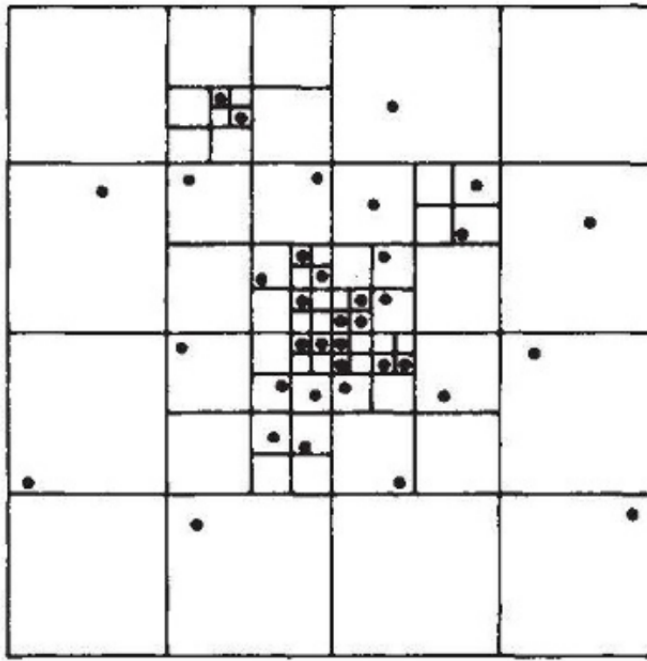


Figure 3.1: A 2D representation of the structure of an oct-tree. The squares represent the nodes and the filled circles denote the location of the simulated particles. This figure is adapted from Barnes & Hut (1986).

KETJU code, is the so-called "tree code".

In tree codes, the gravitational forces experienced by particles are not generated by the other particles themselves, but by so-called "nodes". These nodes are part of a structure called a "tree". In GADGET-3, this structure can be further specified as an "oct-tree", which is constructed as follows. First, the whole simulated system is enclosed in a single cubic volume called the "root" node. This cube is then divided into eight smaller cubic volumes called "child" nodes, and becomes their "parent" node. Next begins a recursive process, where child nodes that contain more than one particle, are divided into their own respective child nodes. Nodes that contain a single particle are thus not divided into child nodes, and are called "leaf" nodes. The above process continues, until every single particle is located inside its own leaf node. The construction of any type of a tree structure follows the same basic principle outlined above. The variations in different tree types, come from the shape of the node-volumes and the number of volumes into which the nodes are subdivided. Figure 3.1 shows a two-dimensional representation of what an oct-tree would look like.

The effect that a node has on the gravitational acceleration of a particle, is calculated with respect to the centre-of-mass of the node in question. In GADGET-

3, the gravitational force of the node is generated by the sum of the masses of the particles inside the node (i.e. the monopole moment of the node; Springel 2005). However, it is also possible to calculate the force as the sum of the forces generated by the multipole moments of the node (Binney & Tremaine, 2008):

$$M_{ij} = \sum_{\alpha} m_{\alpha} x_i^{\alpha} x_j^{\alpha}; \quad M_{ijk} = \sum_{\alpha} m_{\alpha} x_i^{\alpha} x_j^{\alpha} x_k^{\alpha}, \quad (3.2)$$

where m_{α} is the mass of the particle α inside the node; and x_i^{α} , x_j^{α} and x_k^{α} are the components of the position vector of said particle, relative to the centre-of-mass of the node. Although only the quadrupole and octopole moments of the node are shown here, higher order multipole moments could also be used.

Of course, using the gravitational influence of every node to generate the acceleration of a particle would not make sense, as every parent node contains the same particles as its child nodes. Thus, which nodes are considered in the evaluation of the gravitational acceleration of a particle, are determined through a "tree walk". Starting from the root node and moving recursively through its child nodes, if a node fulfils an "opening criterion" it is taken into account in the force calculation, otherwise the walk moves onto its child nodes. The original opening criterion described by Barnes & Hut (1986) is the following:

$$\frac{l}{D} < \theta, \quad (3.3)$$

where l is the length of the node, D is the distance between the particle and the centre-of-mass of the node, and θ is some predetermined opening angle. Once all of the nodes that contribute to the acceleration of the particle have been determined, the gravitational influence that the system has on the motion of the particle can be calculated as the sum of these force contributions.

Using an opening criterion such as the one in equation 3.3, allows one to prioritise accurate calculations for the significant gravitational effects induced by nearby particles. The tree-code treats these neighbouring particles essentially as singular, while dealing with the individually weaker gravitational interactions from faraway particles, as though they were generated by a single bulk of mass.

It is important to note that, in order to maintain accuracy, the tree structure must be reconstructed once the simulated particles have been propagated over a number of time-steps. How often this reconstruction is done, however, depends on the desired accuracy of the simulation. In simulation codes such as KETJU, which need to simulate dynamics with exceptionally high precision, the tree must be built after every integration step. The labour needed for the construction of the

tree scales according to $N \ln N$, as does the number of force calculations (Binney & Tremaine, 2008). However, even accounting for this additional work, when dealing with systems that contain a very large number of simulated particles, the use of the tree code is still far more efficient than the direct summation method, which has an N^2 scaling.

3.2 Softened Dynamics

As equation 3.1 shows, the gravitational force between two massive point-masses starts to grow rapidly as the separation between them decreases. The removal of this divergence in the magnitude of the gravitational force is called "softening" the dynamics. The simplest example of softened dynamics is so-called Plummer softening, where the gravitational potential of a point-mass is described as:

$$\phi = -\frac{GM}{\sqrt{r^2 + \epsilon^2}}, \quad (3.4)$$

and where ϵ is the "softening length". As one can see, using equation 3.4 to describe the gravitational potential causes the potential to converge at a constant value, as the separation $r \rightarrow 0$. However, the gravitational force generated by the Plummer potential is never exactly Newtonian, meaning that the use of this type of softening, inevitably introduces some errors into the motion of the simulated bodies.

The use of softened dynamics is important when simulating the motion of multiple particles in a collisionless system. Usually, in simulations of galactic dynamics, the interacting particles are not representative of singular bodies. Often these particles are orders of magnitude more massive, and significantly less numerous, than for example the stars in a galaxy analogous to the simulated dynamical system. In such cases, the particles are used to depict phase space density; and thus their motion describes the general motion of mass in the system, rather than the trajectories of specific stellar bodies. In fact, the initial positions and velocities of simulated particles are often generated through Monte-Carlo sampling (i.e. random sampling) of the phase space density distribution of the system. Due to their abnormally high mass, strong interactions between two such particles, and the resulting changes in their motion, are possible in the simulated system; even though the process that the interaction represents is completely unphysical. Thus, removing the divergence in the strength of the gravitational force is in fact necessary, when trying to make the simulations of collisionless systems physically accurate.

The tree code in GADGET-3 uses softened dynamics when calculating the

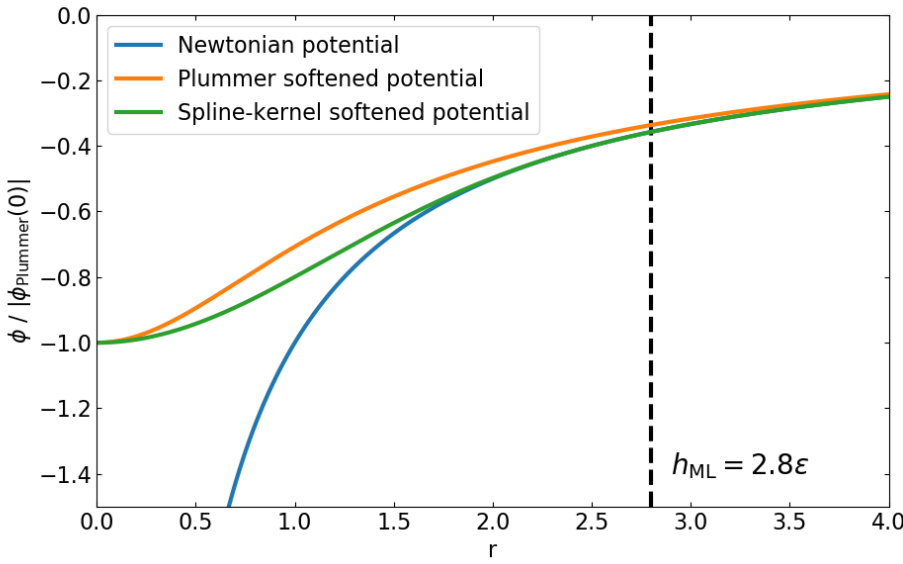


Figure 3.2: Softened and pure Newtonian gravitational potentials as a function of distance. The potential on the y-axis is normalised so that, at $r = 0$ the Plummer softened potential is $\phi_{\text{Plummer}}(0) = -1$. The distance r is given in units, where $G = M = \epsilon = 1$. The spline-kernel softening length is $h_{\text{ML}} = 2.8\epsilon$, and the vertical dashed black line shows the location at which $r = h_{\text{ML}}$.

gravitational forces between particles. In the code, the softening is done using a "Monaghan-Lattanzio" spline kernel (Monaghan & Lattanzio, 1985), which gives an exactly Newtonian gravitational potential outside of the softening length h_{ML} . The equation for the softened gravitational potential in the GADGET-3 tree code is (Springel et al., 2001):

$$\phi(r) = \frac{GM}{h_{\text{ML}}} W\left(\frac{r}{h_{\text{ML}}}\right), \quad (3.5)$$

where W is a spline-kernel defined as:

$$W(u) = \begin{cases} \frac{16}{3}u^2 - \frac{48}{5}u^4 + \frac{32}{5}u^5 - \frac{14}{5} & 0 \leq u < \frac{1}{2} \\ \frac{1}{15}u^{-1} + \frac{32}{3}u^2 - 16u^3 + \frac{48}{5}u^4 - \frac{32}{15}u^5 - \frac{16}{5} & \frac{1}{2} \leq u < 1 \\ -\frac{1}{u} & 1 \leq u \end{cases}. \quad (3.6)$$

The length of h_{ML} is defined as $h_{\text{ML}} = 2.8\epsilon$, where ϵ is the Plummer softening length. This naturally makes the softened gravitational potential fully Newtonian beyond $r = 2.8\epsilon$. In addition, the use of this softening length in particular, also makes the spline-kernel softened potential equivalent to the Plummer-potential at $r = 0$.

Since the spline-kernel softened potential is equivalent to the purely Newtonian potential at distances beyond the softening length h_{ML} , it provides a much more

accurate estimation of galactic dynamics than the Plummer potential. Furthermore, the fact that the spline-kernel softening, similarly to Plummer softening, causes the potential to converge towards a constant value at $r = 0$, it is also applicable in simulations of collisionless systems. Figure 3.2 shows both of these properties. From the figure, one can also see that the spline-kernel softened potential seems to be all around more Newtonian than the Plummer potential, even at distances smaller than the softening length.

3.3 AR-CHAIN

As stated above, KETJU uses the algorithmic regularisation chain code (AR-CHAIN, Mikkola & Merritt 2008) to simulate the dynamics near SMBHs with great accuracy. AR-CHAIN consists of three main components: regularisation of the few-body problem through time-transformed leapfrog integration, reduction of roundoff errors through the use of relative chain-coordinates, and the increase of its accuracy through Gragg-Bulirsch-Stoer extrapolation.

3.3.1 Algorithmic Regularisation

When simulating strong inter-particle interactions, a high numerical accuracy is often maintained through the use of adaptive time-steps. However, this raises the possibility that as the interactions become stronger, the time-steps become infinitesimally small and the simulation effectively stops progressing. Fortunately, this can be circumvented through the use of regularisation (see section 2.6).

In AR-CHAIN, the regularisation procedure employed is so-called "algorithmic regularisation", which is based on two different time-transformations for the equations of motion of the particle position and every other time-dependent variable, respectively. The two fictitious times used in the regularisation are subtly different from each other, but should be identical along the exact solution of the N -body problem. For the particle positions, the time-transformation is given as (Mikkola & Merritt, 2008):

$$ds = [\alpha(T + B) + \beta\omega + \gamma]dt, \quad (3.7)$$

while for the other, velocity-like, variables as:

$$ds = [\alpha U + \beta\Omega + \gamma]dt, \quad (3.8)$$

where s is the new fictitious time; T , U and B , are the kinetic, potential and binding energies ($B = U - T$), respectively; α , β and γ are variables, which determine the

terms that are taken into account in the time-transformation (often, for example in KETJU, these parameters are set as $(\alpha, \beta, \gamma) = (1, 0, 0)$); Ω is an arbitrary function of the particle positions ($\Omega = \Omega(\mathbf{r})$); and the parameter ω is defined by the initial value $\omega(0) = \Omega(0)$, and the time dependence:

$$\dot{\omega} = \sum_i^N \frac{\partial \Omega}{\partial \mathbf{r}} \cdot \mathbf{v}, \quad (3.9)$$

where N is the number of particles in the system. Since the time-transformations should be identical along the exact solution of the N -body equation of motion, it follows that, for the exact solution, the Ω and ω parameters should behave in the same way (i.e. $\Omega(t) = \omega(t)$).

In the KETJU implementation of AR-CHAIN, the parameter β is usually set as $\beta = 0$. This means that Ω and ω do not affect the time-transformation, and thus calculating their values is effectively optional. Still, following the time-evolution and convergence of these parameters is useful, as it allows one to examine how close to the exact solutions the equations of motion are being solved in the simulation, and update the simulation accuracy accordingly.

The function often used for Ω is similar to the potential energy, and is defined as:

$$\Omega = \sum_i^N \sum_{j>i}^N \frac{\Omega_{ij}}{|\mathbf{r}_{ij}|}, \quad (3.10)$$

where \mathbf{r}_{ij} is the distance between particles i and j , and where the parameter Ω_{ij} is equivalent to the mass in the formula of the potential energy. The value of Ω_{ij} can determined using the equation:

$$\Omega_{ij} = \begin{cases} \tilde{m}^2 & m_i m_j < \epsilon_\Omega \tilde{m}^2 \\ 0 & \text{otherwise} \end{cases}, \quad (3.11)$$

where the quantity \tilde{m}^2 is the mean-mass product of the system:

$$\tilde{m}^2 = \frac{2}{N(N-1)} \sum_i^N \sum_{j>i}^N m_i m_j, \quad (3.12)$$

and ϵ_Ω is a user defined parameter. The value of this parameter is set to $\epsilon_\Omega = 10^{-3}$ in KETJU, meaning that only gravitational influences between particles with sufficiently small masses is taken into account when calculating Ω . This is done in order to make sure that small bodies, which have a negligible impact on the total gravitational potential, can still have an effect on the regularisation.

Using the two fictitious time definitions from equations 3.7 and 3.8, allows us to form two sets of regularised equations of motion for the N -body problem. These equations consist of the coordinate equations:

$$\begin{aligned} t' &= \frac{dt}{ds} = 1/(\alpha(T + B) + \beta\Omega + \gamma) \\ \frac{d\mathbf{r}_i}{ds} &= t'\mathbf{v}_i, \end{aligned} \quad (3.13)$$

and the velocity equations:

$$\begin{aligned} \tilde{t}' &= \frac{dt}{ds} = 1/(\alpha U + \beta\omega + \gamma) \\ \frac{d\mathbf{v}_i}{ds} &= \tilde{t}'(\mathbf{a}_i + \mathbf{f}_i) \\ \frac{d\omega}{ds} &= \tilde{t}' \sum_i^N \frac{\partial \Omega}{\partial \mathbf{r}_i} \cdot \mathbf{v}_i \\ \frac{dB}{ds} &= -\tilde{t}' \sum_i^N \frac{\partial T}{\partial \mathbf{v}_i} \cdot \mathbf{f}_i, \end{aligned} \quad (3.14)$$

where \mathbf{a}_i is the N -body acceleration, and \mathbf{f}_i is the acceleration caused by perturbing gravitational forces, generated by bodies outside the N -body system simulated using AR-CHAIN. However, the gravitational force that produces the acceleration of the simulated particles is still Newtonian even in the time-transformed equations, and thus, it is still not defined when $r = 0$. Fortunately, this does not pose any practical problems for the simulations, as the calculations are naturally done using floating point numbers. Thus, the probability for the separation between two point masses being exactly $r = 0$ is so small, that it is likely never to occur.

The final component of the algorithmic regularisation procedure is the leapfrog integrator. Generally, numerical orbit integration procedures consist of two types of steps; so-called "kick" and "drift" steps, where the dynamics of a simulated particle is updated according to the current state of the system, and where the particle is propagated according to its current dynamics, respectively. In the simplest possible integrator, when propagating a system over some time-step Δt , the particles are both kicked and then drifted once (or vice versa) over the whole time-step. In a leapfrog integrator, however, the preceding step is divided into two smaller steps over half of the total time-step, which are then calculated before and after the second step. We can help visualise this difference, by using $\mathbf{X}(\Delta t)$ and $\mathbf{V}(\Delta t)$ to notate the drift and kick steps, respectively. For the simple integrator, a single time-step would be:

$$\mathbf{X}(\Delta t)\mathbf{V}(\Delta t), \quad (3.15)$$

while a leapfrog time-step could be written as:

$$\mathbf{X}(\Delta t/2)\mathbf{V}(\Delta t)\mathbf{X}(\Delta t/2). \quad (3.16)$$

Depending on which of the steps is divided into two, the integrator can either be a so-called "kick-drift-kick" (DKK) leapfrog, or a "drift-kick-drift" (DKD) leapfrog. The variant described by equation 3.16 is the DKD leapfrog, which is also the version used by KETJU (Rantala et al., 2017).

Using the time-transformation detailed above, a leapfrog integrator, and setting (α, β, γ) to $(1, 0, 0)$; AR-CHAIN is able to calculate exact two-body orbits, up to numerical accuracy (Mikkola & Merritt, 2008). However, simply using the algorithmic regularisation does not provide enough accuracy to calculate precise motion near SMBHs. Thus, it is imperative to improve the numerical accuracy of the integration through both, the usage of chain coordinates (section 3.3.2), and an extrapolation method (section 3.3.4).

3.3.2 Chained Coordinate System

Apart from simple arithmetic operations with integers, all calculations done by computers contain roundoff errors, due to the finite accuracy of floating point numbers. The effects caused by these errors can be significant when subtracting two numbers that have similar and very large values, from each other. To reduce the size of the roundoff error, AR-CHAIN uses a chain coordinate system to calculate gravitational interactions between nearby particles, where instead of using, for example, centre-of-mass coordinates to calculate the gravitational forces, the relative positions between particles and their closest neighbour are used. This naturally decreases the size of the subtracted values, as the relative distance between two particles is likely significantly shorter, than their respective distances from the centre-of-mass of the system.

The chain coordinate system is constructed as follows. First, the particles that have the shortest distance from each other are identified. These particles are designated as the "tail" and the "head" of the chain. Next, the particle that is closest to either the head or the tail is added to the chain. This particle then becomes the new head or tail. This step is iterated over, until every particle in the system is included in the chain, and the construction of the chain is thus deemed finished.

Once the chain has been formed, and the particles have been renamed from 1 to N according to their position in the chain, $N - 1$ relative position and velocity

vectors can be calculated using the following (Mikkola & Merritt, 2008):

$$\begin{aligned}\mathbf{X}_k &= \mathbf{r}_{k+1} - \mathbf{r}_k \\ \mathbf{V}_k &= \mathbf{v}_{k+1} - \mathbf{v}_k.\end{aligned}\tag{3.17}$$

In the chained coordinate system, the basic equations of motion thus become:

$$\begin{aligned}\dot{\mathbf{X}}_k &= \mathbf{V}_k \\ \dot{\mathbf{V}}_k &= \mathbf{A}_{k+1} - \mathbf{A}_k + \mathbf{f}_{k+1} - \mathbf{f}_k,\end{aligned}\tag{3.18}$$

where \mathbf{f} is the acceleration caused by external gravitational perturbations, and \mathbf{A} is the total Newtonian gravitational acceleration induced by the other particles in the chain system, defined as:

$$\mathbf{A}_k = - \sum_{j \neq k} m_j \frac{\mathbf{r}_{jk}}{|\mathbf{r}_{jk}|^3}.\tag{3.19}$$

The parameter \mathbf{r}_{jk} in this equation, is the relative position from the subject particle k to particle j . Using the chain coordinate system, this vector is as a sum of the chain distances from j to k . However, naturally the sum of inter-particle vectors is seldom equivalent to the exact separation between two arbitrary particles in Cartesian coordinates. The errors caused by this can be significant for particles that are far from each other in the chain. Thus, the use of chain coordinates improves the numerical accuracy of the acceleration, only when used for particles that are sufficiently close to each other. For faraway particles, the distance should still be determined using the basic Cartesian positions. Taking all this into account, the position vector \mathbf{r}_{jk} is determined as follows (e.g. Rantala et al., 2017):

$$\mathbf{r}_{jk} = \begin{cases} \mathbf{r}_j - \mathbf{r}_k & |j - k| > N_d \\ \sum_{i=\min\{j,k\}}^{\max\{j,k\}-1} \text{sign}(j - k) \mathbf{X}_i & |j - k| \leq N_d \end{cases},\tag{3.20}$$

where N_d denotes the maximum number of chain distances that can be used to determine the separation between two particles. Mikkola & Merritt (2008) find that $N_d = 2$ produces the best results, and as such, the KETJU implementation of AR-CHAIN uses this same value.

In the chain coordinates, the time-transformed coordinate equations of motion can be written as:

$$\begin{aligned}t' &= \frac{dt}{ds} = 1/(\alpha(T + B) + \beta\Omega + \gamma) \\ \frac{d\mathbf{X}_i}{ds} &= t' \mathbf{V}_i,\end{aligned}\tag{3.21}$$

while the velocity equations are:

$$\begin{aligned}\tilde{t}' &= \frac{dt}{ds} = 1/(\alpha U + \beta \omega + \gamma) \\ \frac{d\mathbf{V}_i}{ds} &= \tilde{t}'(\mathbf{A}_i + \mathbf{f}_i) \\ \frac{d\omega}{ds} &= \tilde{t}' \sum_i^N \frac{\partial \Omega}{\partial \mathbf{X}_i} \cdot \mathbf{V}_i \\ \frac{dB}{ds} &= -\tilde{t}' \sum_i^N \frac{\partial T}{\partial \mathbf{v}_i} \cdot \mathbf{f}_i.\end{aligned}\tag{3.22}$$

Using the chained variables in the equations of motion is not always convenient (Mikkola & Merritt, 2008). Thus, for example, the time-derivative of the binding energy (see final equation of the set in equation 3.22) is still evaluated using Cartesian velocities.

3.3.3 Velocity Dependent PN-Corrections

Since KETJU can be used to simulate dynamics near supermassive black holes, it takes relativistic effects into account, in the form of post-Newtonian corrections up to order 3.5PN (Rantala et al., 2017). As relativistic effects are dependent on the relative momentum between objects, the velocity of the simulated particle has to be considered, when applying the PN-corrections to its equations of motion. This results in the following equation of motion for the velocity of a particle:

$$\frac{d\mathbf{V}_i}{ds} = \tilde{t}'(\mathbf{A}_i + \mathbf{f}_i + g_i(\mathbf{v}_i)),\tag{3.23}$$

where $g(\mathbf{v}_i)$ describe the additional acceleration experienced by the particle due to velocity dependent PN effects. In the case of an SMBH, it might also be useful to take into account how general relativity affects the spin of the particle. The equation of motion of the spin is:

$$\frac{d\mathbf{S}_i}{ds} = \tilde{t}' \mathbf{S}_{\text{PN},i} \times \mathbf{S}_i,\tag{3.24}$$

where \mathbf{S}_i and $\mathbf{S}_{\text{PN},i}$ are the spin of the particle and the spin PN-correction, respectively.

The fact that the addition of the velocity dependent acceleration causes the time-derivative of the velocity to be dependent on itself, means that it can not be integrated using conventional methods. In KETJU, this integration problem is solved through expanding the position-velocity phase space to include an "auxiliary velocity" \mathbf{w}_i , and using its chained counterpart \mathbf{W}_i when necessary (Rantala et al.,

2017). This allows one to separate the calculation of the time-derivative of the velocity from the velocity itself, by instead, using the auxiliary velocity when applying the accelerative PN-corrections (Hellström & Mikkola, 2010; Pihajoki, 2015).

The addition of w_i to the phase space modifies the leapfrog integration-step slightly. At the beginning of the kick-step, both auxiliary velocities are set equal to their "physical" counterparts. Next, the physical velocities are kicked over half a time-step, while using the auxiliary velocities in the velocity dependent acceleration term. The new physical velocities are then used to update the auxiliary parameters over the whole time-step. Finally, the physical velocities are integrated over the remaining half-time-step, by applying the previously calculated auxiliary velocities for the velocity dependent terms. This gives an accurate value for the velocity, after the time-step Δt .

Using a notation similar to the one used for the basic leapfrog algorithm for the above velocity integration steps, the velocity dependent kick step can be written as:

$$\mathbf{V}(\Delta t/2)\mathbf{W}(\Delta t)\mathbf{V}(\Delta t/2). \quad (3.25)$$

Thus, a single DKD leapfrog time-step, where velocity dependent forces are calculated with the help of auxiliary velocities is:

$$\mathbf{X}(\Delta t/2)\mathbf{V}(\Delta t/2)\mathbf{W}(\Delta t)\mathbf{V}(\Delta t/2)\mathbf{X}(\Delta t/2). \quad (3.26)$$

Of course, while the use of auxiliary variables has only been discussed in terms of integrating the time-derivative of the velocity in this section, the procedure can also be used to solve other equations of motion. For example, the same self-dependence problem caused by the addition of PN-terms, extends to the time-derivative of the spin of the black hole, as seen in equation 3.24. This issue can then be resolved, by expanding the phase space to include the auxiliary spin (\mathbf{Z}).

3.3.4 Gragg-Bulirsch-Stoer Extrapolation

The final component in the high precision AR-CHAIN algorithm is the "Gragg-Bulirsch-Stoer" (GBS; Gragg 1965; Bulirsch & Stoer 1966) extrapolation method, the use of which is crucial for the high numerical accuracy of the algorithm. The basic principle behind GBS-extrapolation is that; when integrating a function over a single time-interval, the integral is calculated multiple times, each time subsequently dividing the time-step into two times as many shorter steps. When increasing the number (n) of these substeps, the integration accuracy increases, and the results

should start to converge toward the exact solution. This exact solution can be estimated, by extrapolating the previously calculated results, and finding out what the solution would be at $n \rightarrow \infty$, i.e. when the length of time described by the subdivisions of the original integration time-step is infinitesimally small.

Implementing the GBS-extrapolation algorithm works as follows. Every time the function is integrated over the original integration interval using a different n , the results are extrapolated at $n \rightarrow \infty$ to get an approximation of the exact solution. In order to extrapolate the results, they are expressed as a function of the length of time described by the individual n substeps used to calculate their value; that is, as a function of: $\Delta t = h/n$, where h is the length of the initial integration time-step. Then, either a polynomial or a rational function is fitted onto these results. The value of the fit at $\Delta t = 0$, now corresponds to the supposed exact solution of the integral at $n \rightarrow \infty$.

Whether the extrapolated result is good enough to be considered "exact", is determined by the user-specified error tolerance parameter η_{GBS} , which should fulfil the condition:

$$\eta_{\text{GBS}} \leq \left| \frac{T_{k+1} - T_k}{T_k} \right|, \quad (3.27)$$

where T_k are previously extrapolated solutions to the integral, k denoting the number of approximate integral solutions used in the extrapolation procedure when calculating the solution in question. The algorithm continues to iterate over k , calculating a new approximate solution of the integral using $n = 2^k$ substeps, and adding it to extrapolation procedure in order to get a more accurate value for the exact solution at $n \rightarrow \infty$, until equation 3.27 holds true. Alternatively, if k exceeds some predefined maximum value k_{\max} , the process starts from the beginning; the difference now being that, the initial integration interval is divided into two new initial intervals. The value that is able to fulfil the error tolerance condition, is then deemed the exact solution of the integral.

3.4 Basic Properties of KETJU

In KETJU, the galactic dynamics is simulated as interactions between particles that represent either; the mass concentration of stars, dark matter or gas; or singular supermassive black holes. The combined functionality of the GADGET-3 tree code and the AR-CHAIN integrator, is then achieved by dividing these simulated particles into three different types: chain particles, perturber particles, and tree particles. The dynamics of the chain particles are simulated using the AR-CHAIN

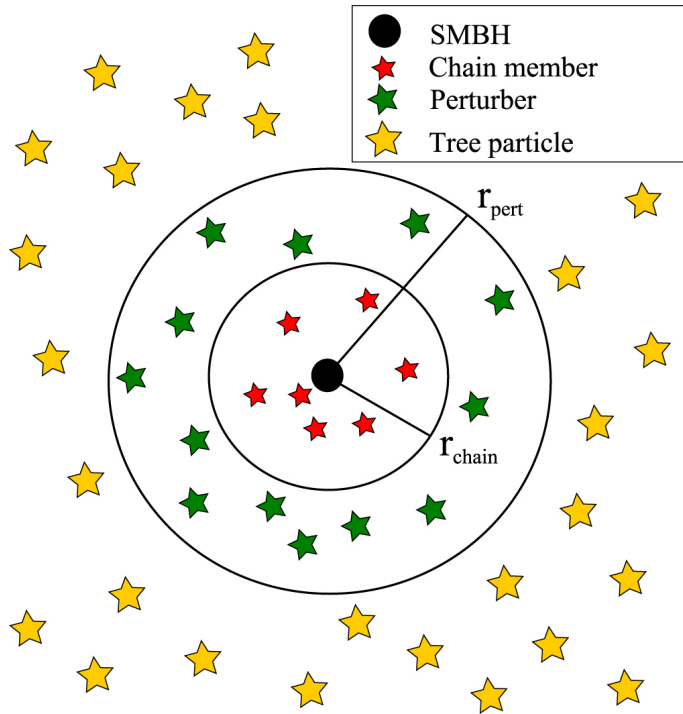


Figure 3.3: An illustration of the way KETJU divides the simulated particles into three different types. The red stars denote the chain particles, while the green and yellow stars show perturber and tree particles, respectively. The black dot is the SMBH particle, and the circles correspond to the regions, which determine the particle type. This figure is adopted from Rantala et al. (2017).

algorithm, and they correspond to the stars near an SMBH as well as the SMBH itself. The perturber and the tree particles, on the other hand, are propagated using the GADGET-3 tree code, and they describe the general dynamics of the simulated stellar system at larger scales. The difference between the perturbers and the tree particles is that, the former are located close enough to the SMBH particle to have a significant individual effect on the dynamics of the chain particles. The type of a particle is determined by its distance from an SMBH. However, as of the current version of the KETJU code, only stellar and SMBH particles can be categorised as chain particles. An illustration of the different particle type regions around an SMBH particle can be seen in figure 3.3.

3.4.1 The Chain Subsystem

In simulations that deal with supermassive black holes, it is of utmost importance, that the dynamics of the SMBH particles are never softened. Softened gravitational potentials naturally induce weaker gravitational interactions, reducing the strength of effects such as dynamical friction, and thus unnaturally lengthening the time-scale

of the SMBH binary inspiral and merger. In KETJU, the non-softened interactions between the SMBH particles are enforced through the combined use of a "chain subsystem", the internal dynamics of which are calculated using the AR-CHAIN, and "Monaghan-Lattanzio" (ML) spline-kernel softening (see section 3.2).

A chain subsystem is made up of an SMBH particle and its surrounding chain particles. Whether a stellar particle is included in the subsystem as a chain particle, is determined through a variable called the "chain radius", defined as (Rantala et al., 2017):

$$\frac{r_{\text{chain}}}{1 \text{ kpc}} = \lambda \times \frac{M_{\bullet}}{10^{10} M_{\odot}}, \quad (3.28)$$

where M_{\bullet} is the mass of the SMBH particle, and λ is a user-specified parameter. If the distance from a stellar particle to an SMBH particle is smaller than the chain radius, it is naturally included in the chain subsystem of the black hole in question. Additionally, the condition $r_{\text{chain}} > h_{\text{ML}}$ (where $h_{\text{ML}} = 2.8\epsilon$ is the "Monaghan-Lattanzio" softening length employed in KETJU) is taken into account when determining the length of the chain radius. Since the dynamics of particles beyond the softening length is exactly Newtonian when using ML-softening, this ensures that gravitational interactions between SMBHs and stars, as well as other SMBHs, are always non-softened.

In the tree code, the chain subsystem behaves as a single collisionless "macro particle". The motion of this macro particle is calculated using the centre-of-mass properties of the subsystem. In order to get the centre-of-mass acceleration of the subsystem, the tree-accelerations of all of the particles included in the chain are calculated. This means that, somewhat counter-intuitively, even though the chain particles are propagated in the tree as a single macro particle, they are "seen" as separate by the other tree-particles.

Since every SMBH has its own regularised region, if two SMBH particles are close enough to each other, it is possible for two chain subsystems to merge. This occurs, when the volumes of the subsystems intersect. A merged chain subsystem behaves similarly to a basic regularised region, where all of the chain particles are included in a single chain in the AR-CHAIN algorithm. In the case of a merged subsystem, the inclusion of stellar particles as chain particles is determined by checking the condition for both SMBHs.

3.4.2 Perturbative Effects of the Perturber and Tree Particles

When calculating the precise motion of the chain particles in the regularised regions around SMBHs, it is important to take into account tidal perturbation caused by the gravitational influence of the other particles in the simulated stellar system. Both the aforementioned perturber and tree particles induce tidal perturbations, however, the way these effects are considered when propagating the chain particles, depends on the respective particle type. When calculating these effects, the gravitational forces induced by the softened gravitational potential (equation 3.5) of the tree-code are used.

The perturber particles are located outside of the regularised region, but lie close enough to the chain particles to have a significant individual perturbative effect on their equations of motion. In KETJU, a tree-particle is deemed to be a perturber, if it is located inside the "perturber radius" (Rantala et al., 2017):

$$r_{\text{pert},i} = \gamma \left(\frac{m_i}{M_\bullet} \right)^{1/3} r_{\text{chain}}, \quad (3.29)$$

where m_i is the mass of a potential perturber particle, and γ is a user-specified parameter, that is set so, that $r_{\text{pert},i} = 2r_{\text{chain}}$ for the lowest-mass simulated particles. Naturally, chain subsystems can be perturbed by other chain subsystems. In case this happens, the perturbative subsystems are resolved, and the gravitational effects of individual chain particles are calculated.

Since the perturber particles are located close to the chain subsystem, the tidal perturbation induced by them depends significantly on their location in respect to the chain particles. This is problematic when calculating the trajectories of the chain particles using AR-CHAIN, as the integration time-steps used in the algorithm are smaller than the time-step used for the propagation of the perturber particles (see section 3.4.4), making the perturbers effectively stationary during the AR-CHAIN integration procedure. To remedy this, the time-evolution of the position of the perturber particles is estimated using following quadratic equation:

$$\mathbf{r}(t) = \mathbf{r}(t_0) + \mathbf{v}(t_0)\Delta t + \frac{1}{2}\mathbf{a}(t_0)(\Delta t)^2, \quad (3.30)$$

where t_0 is the moment in simulation time, at which the AR-CHAIN integration procedure starts; $\mathbf{r}(t_0)$, $\mathbf{v}(t_0)$ and $\mathbf{a}(t_0)$ are the initial position, velocity and acceleration of a perturber particle, respectively; and Δt is the time elapsed from t_0 , i.e. $\Delta t = t - t_0$. The tree particles, on the other hand, are estimated to be stationary

during the whole integration time-step. This approximation is valid, as the scale of the tree-particle region is so large, that small variations in the positions of the individual particles do not have a significant effect on the total perturbative force (Ahmad & Cohen, 1973).

Naturally, as the perturber and tree particles exert a gravitational force onto the chain particles, they must experience an equal and opposing force from the particles in the subsystem (as stated by Newton's third law). This is taken into account in KETJU, by substituting the gravitational acceleration induced by the chain subsystem macro particle onto the perturbative particle, with the total gravitational force from the individual chain particles. This gravitational force is calculated with the direct summation method (see section 3.1), using Monaghan-Lattanzio spline-kernel softening (equation 3.5).

3.4.3 Particle Mergers

In KETJU simulations, it is possible for an SMBH particle to merge with a stellar particle or another SMBH particle. Whether the merger event occurs, is determined by two possible criteria. The first criterion compares the gravitational wave coalescence time-scale for an SMBH binary to the tree code time-step, and is thus only relevant for SMBH-SMBH mergers. The coalescence time-scale can be approximated using (Rantala et al., 2017):

$$t_c \sim -\frac{a}{4\dot{a}}, \quad (3.31)$$

where a is the semi-major axis of the binary orbit, and \dot{a} is its time derivative, which (as shown in section 2.3.3) can be calculated using post-Newtonian corrections at order 2.5PN as:

$$\left\langle \frac{da}{dt} \right\rangle = -\frac{64}{5} \frac{G^3 M_1 M_2 (M_1 + M_2)}{c^5 a^3 (1 - e^2)^{7/2}} \left(1 + \frac{73}{24} e^2 + \frac{37}{96} e^4 \right). \quad (3.32)$$

If the condition $t_c < s_1 \Delta t_{\text{tree}}$, where $s_1 > 1$ is a temporal safety factor (usually $s_1 = 10$), holds true; the two SMBH particles are merged.

The second criterion is based on the relative position of the two particles. For two SMBHs, the merger event is set to occur, if their separation is smaller than:

$$r_{\min,S} = 6 \left(\frac{2GM_{\bullet,1}}{c^2} + \frac{2GM_{\bullet,2}}{c^2} \right), \quad (3.33)$$

which corresponds to the sum of the Schwarzschild-radii (i.e. the distance from a black hole at which the escape velocity is equivalent to the speed of light) of the binary pair multiplied by six. The seemingly arbitrary multiplication of the condition,

comes from the fact that the use of PN dynamics is based on the approximation that $v/c \ll 1$. At small binary separations, the orbital velocities of the SMBHs naturally rise, which might invalidate the use of the PN-approximation. Through testing, Rantala et al. (2017) find that PN-dynamics is still valid at distances corresponding to equation 3.33.

In the case of an SMBH - stellar particle merger however, depending on which of the parameters is larger; the minimum particle separation is determined either using the Schwarzschild radius of the SMBH, or the tidal disruption radius (i.e. the distance from the black hole, where its gravitational force tears an orbiting star apart). The minimum distance between two such particles is determined by following equation:

$$r_{\min,T} = \max \left\{ \frac{12GM_\bullet}{c^2}, s_2 R_\odot \left(\frac{M_\bullet}{M_\odot} \right)^{1/3} \right\}, \quad (3.34)$$

where M_\odot and R_\odot are the solar mass and radius, respectively, and $s_2 > 1$ is the spatial safety factor.

The particle mergers are checked before every integration time-step. If either of the SMBH-SMBH merging conditions are met, the simulated particles are replaced by a new particle with the following properties (Rantala et al., 2017):

$$\begin{aligned} M &= M_1 + M_2 \\ \mathbf{r} &= (M_1 \mathbf{r}_1 + M_2 \mathbf{r}_2)/M \\ \mathbf{v} &= (M_1 \mathbf{v}_1 + M_2 \mathbf{v}_2)/M \\ \mathbf{L} &= \frac{M_1 M_2}{M} (\mathbf{r}_2 - \mathbf{r}_1) \times (\mathbf{v}_2 - \mathbf{v}_1) \\ \mathbf{S} &= \mathbf{L} + \mathbf{S}_1 + \mathbf{S}_2, \end{aligned} \quad (3.35)$$

where \mathbf{L} is the angular momentum, and \mathbf{S} is the spin of the SMBH (however, note that in KETJU simulations (e.g. chapter 4), the spin is often not taken into account, as its effects on the stellar dynamics is not significant). If an SMBH particle and a stellar particle merge, however, the stellar particle is simply removed from the simulation.

3.4.4 Incorporating AR-CHAIN in the GADGET-3 Leapfrog

The GADGET-3 tree-code integrator used in KETJU, is a KDK-leapfrog (Springel, 2005). Implementing the regularised chain region in the leapfrog integration works as follows. The first step, before starting the integration cycle itself, is naturally to

determine the particle types for all particles in the simulated system and find the chain subsystem macro particles.

Next, the particles that have been determined as tree, perturber or macro particles, are then kicked and drifted, as expected in a KDK-leapfrog. After the drift-step, the chain particles are propagated using the chain integrator. Once the AR-CHAIN algorithm has concluded its calculations, the final kick step of the GADGET-3 leapfrog takes place. Lastly, the force corrections on the peruturbing particles, necessitated by the Newton's third law, are taken into account.

The GADGET-3 leapfrog in KETJU, uses individual adaptive time-steps for different particles, the lengths of which can be determined using:

$$\Delta t_{\text{grav}} = \left(\frac{2\eta\epsilon}{|\mathbf{a}|} \right)^{1/2}, \quad (3.36)$$

where \mathbf{a} is the acceleration of a particle, ϵ is the gravitational softening length, and η is a user-specified error tolerance parameter. These time-steps are then rounded down to the nearest discrete power-of-two time-step:

$$\Delta t_n = 2^n \Delta t_{\min}, \quad (3.37)$$

where Δt_{\min} is the smallest possible time-step allowed by the simulation.

The basic procedure for determining the time-steps for individual particles in GADGET-3, is used for the tree-particles in KETJU. The chain subsystem macro particles and the individual chain particles that are integrated using the AR-CHAIN algorithm, are placed onto the smallest tree time-step found. This time-step is used as the initial integration interval in the AR-CHAIN integration. Using the smallest time-step from the tree code for the chain particles, ensures that they are active at all times during the simulation, and that they are on the smallest time-step, if they happen to leave the chain region. The perturber particles are also placed on the smallest tree particle time-step. This is done in order to make sure that they are synchronised with the chain particles.

4. Simulating Core Formation Using KETJU

In this chapter I study the formation of cored galaxies in galaxy mergers. The analysis focuses on the results from galaxy merger simulations run by Rantala et al. (2018) using the KETJU code. In all but one simulation, the merger progenitor galaxies contain central supermassive black holes. During the merger event the SMBHs form a hard binary. These binaries are a likely source for the observed low-luminosity cores, as they can eject stars from the galactic centre through complex three-body interactions. Here I determine if there is a connection between the central binary SMBH and the existence of a core deficient in light, and if the simulated KETJU results agree with observations of cored galaxies.

4.1 Simulation Details

The simulation sample run by Rantala et al. (2018) includes seven different equal-mass mergers of two identical galaxies. The merger progenitor galaxies (named BH-0 - BH-6) used in the different simulations consist of equal mass stellar particles and equal mass dark matter particles, where the mass of the stellar particles differ from the mass of the dark matter particles. The progenitors are gas free (i.e. the simulations describe so-called "dry" mergers), and all of them but one contains an SMBH at their centre.

The initial conditions (ICs) of the merger progenitor galaxies are modelled as multicomponent, spherically symmetrical stellar systems. They consist of the three aforementioned components: stellar particles, dark matter particles and a central SMBH. The central SMBH is simply modelled as a single point mass, and is located at the origin of the internal coordinate system of the host galaxy. The stellar and dark matter components, on the other hand, consist of multiple particles which are distributed according to the spherically symmetric Dehnen density-potential model

(Dehnen 1993; see equations 2.28 and 2.29 in section 2.5.2). An important difference in the models used for the stellar and dark matter particles, is the value of the central slope (γ) of the mass-density profile. For stellar particles we set the γ -parameter to $\gamma = 3/2$, while for the dark matter particles the value of $\gamma = 1$ is used.

When constructing the multicomponent ICs for the progenitor galaxies, the positions of the stellar and dark matter particles are determined through their respective cumulative mass profiles. These mass profiles are derived using the aforementioned Dehnen density-potential model, and can be written as:

$$M(r) = 4\pi \int_0^r \rho(r)r^2 dr = M \left(\frac{r}{r+a} \right)^{3-\gamma}, \quad (4.1)$$

where $\rho(r)$ is the density profile of the model (equation 2.28).

In equation 4.1, the value of the scaling radius (a) is determined quite differently for the stellar and dark matter particle distributions. One way of calculating a is to derive the formula for the half-mass radius from the cumulative mass profile. This gives us the equation:

$$r_{1/2} = a \left(2^{1/(3-\gamma)} - 1 \right)^{-1}, \quad (4.2)$$

from which a can be solved easily. However, in order to get a value for a , one now needs to know the half-mass radius of the particle distribution. Fortunately, the half-mass radius of the stellar population can be determined through drawing an equivalence between it and the effective radius of the galaxy. If the galaxy, for which we are trying to determine the scaling radius, has a constant mass-to-light ratio, its mass and light profiles are proportional to each other. In this case, the properties described by the two profiles are analogous, which means that the half-mass radius and the effective radius are equivalent to each other. In cases, such as our simulations, where only the 2D projection of the effective radius is known, the three dimensional half-mass radius can be approximated using the following formula:

$$R_e \approx \frac{3}{4} r_{1/2}, \quad (4.3)$$

where R_e is the aforementioned 2D projected effective radius. Thus, knowing the effective radius of the galaxy allows one to determine the stellar scaling radius a_* , by using both equation 4.2 and 4.3.

The scaling radius of the dark matter particle distribution can be derived using the dark matter fraction (f_{DM}) inside the stellar half-mass radius. The dark matter fraction describes the fraction of the total mass inside radius r that is contributed

by dark matter, and is defined by the following equation:

$$f_{\text{DM}}(r) = \frac{M_{\text{DM}}(r)}{M_{\star}(r) + M_{\text{DM}}(r)}. \quad (4.4)$$

With the above equation, one can get the dark matter scaling radius by substituting the cumulative mass profiles in the equation with the one from equation 4.1 when $r = r_{1/2}$, and using equation 4.2 to define the stellar half-mass radius. This gives us the following formula for calculating the dark matter scaling radius:

$$a_{\text{DM}} = r_{1/2} \left[\sqrt{\frac{2M_{\text{DM}}}{M_{\star}}} \left(\frac{1}{f_{\text{DM}}(r_{1/2})} - 1 \right) - 1 \right]. \quad (4.5)$$

Finally, applying the half-mass radius approximation from equation 4.3 allows us to calculate the dark matter scaling radius as follows:

$$a_{\text{DM}} \approx \frac{4}{3} \left[\sqrt{\frac{2M_{\text{DM}}}{M_{\star}}} \left(\frac{1}{f_{\text{DM}}(r_{1/2})} - 1 \right) - 1 \right] R_e. \quad (4.6)$$

If the positions of the particles in the simulated progenitor galaxies are known, their velocities can be determined using the Eddington's formula (Binney & Tremaine, 2008). The different particles thus have the following distribution function in the position-velocity phase space:

$$f_i(\varepsilon) = \frac{1}{\sqrt{8\pi^2}} \int_{\Phi_T=0}^{\Phi_T=\varepsilon} \frac{d^2\rho_i}{d\Phi_T^2} \frac{d\Phi_T}{\sqrt{\varepsilon - \Phi_T}}, \quad (4.7)$$

where ρ_i is the Dehnen-model density profile (equation 2.28) for the particle type in question, and Φ_T is the total gravitational potential ($\Phi_T = \Phi_{\star} + \Phi_{\text{DM}} + \Phi_{\bullet}$). The variable ε is the relative energy:

$$\varepsilon = -\Phi_T + \Phi_0 - \frac{1}{2}v^2, \quad (4.8)$$

where v is the velocity of the particle, and Φ_0 is a chosen zero point for the potential. This zero point is usually chosen so that, $f > 0$ for $\varepsilon > 0$, and that $f = 0$ for $\varepsilon \leq 0$. In the case of our simulations the zero point is set as $\Phi_0 = 0$, since the galaxies are modelled in isolation, and extend in principle to infinity.

The general procedure for generating the multicomponent ICs of the progenitor galaxies is as follows. The positions of the stellar and dark matter particles are generated using the inverse of their respective cumulative mass function described in equation 4.1. Afterwards, using equation 4.7, tabulated values for the distribution functions of the two particle types are calculated into a lookup table. The velocities of the particles are then sampled by interpolating these tabulated distribution

function values. Finally, the central SMBH is placed in the centre of the progenitor galaxy.

The physical parameters used for generating the progenitor galaxies in this set of simulations according to the aforementioned procedure, are given in table 4.1 under "Common physical properties". As the name implies, they are identical across every simulated progenitor galaxy. This means that as far as their stellar and dark matter particle populations are concerned, the progenitors are identical.

The values for these common properties are motivated by observations and dynamical simulations of NGC 1600 (Rantala et al., 2018). NGC 1600 is a massive ($M_* \approx 8.3 \times 10^{11} M_\odot$) early-type cored galaxy with a large observed core radius ($r_b \approx 2.15$ arcsec, which corresponds to a physical length of ~ 0.667 kpc at the distance of 64 Mpc) and a central supermassive black hole with a mass of $\sim 1.7 \times 10^{10} M_\odot$ (Thomas et al., 2016). By using these values for the physical properties of the simulated merger progenitors, the resulting merger remnant should in principle be as similar as possible to NGC 1600.

Figure 4.1 shows an example profile for the stellar mass density distribution of the simulated progenitor galaxies. The profile is calculated from a stellar particle distribution produced using the same multicomponent IC generation procedure described previously in this section. The physical properties used in the generation of the distribution are mostly identical to the ones seen in table 4.1. The only difference being, that the values used for the number of stellar and dark matter particles are only 10% of the ones seen in the table. After the particles have been generated, the density profile is calculated by moving the stellar particles of the progenitor galaxy into their centre-of-mass coordinates, dividing them into logarithmic bins, and calculating the mass density inside the respective bins.

Table 4.1 also shows the masses of the central SMBHs in each of the seven progenitor galaxies. The SMBH mass is the only physical property that changes from one progenitor to another. Six of the progenitor galaxies (BH-1 - BH-6) contain central supermassive black holes, with masses varying from $8.5 \times 10^8 M_\odot$ to $8.5 \times 10^9 M_\odot$. A merged binary of two of the largest SMBHs in the table, is equivalent in mass to the observed central SMBH in NGC 1600. The seventh progenitor (BH-0) does not contain an SMBH in its centre, and the merger simulation containing these progenitors is simply included for the sake of comparison.

The seven merger simulations thus comprise of mergers of two identical progenitor galaxies with properties described in table 4.1. These galaxies are merged on a nearly parabolic orbit with an initial separation of $d = 30$ kpc. This kind of

Common physical properties					
M_\star [$\times 10^{10} M_\odot$]	R_e [kpc]	M_{DM} [$\times 10^{10} M_\odot$]	$f_{\text{DM}}(r_{1/2})$	N_\star	N_{DM}
41.5	7	7500	0.25	4.15×10^6	1.0×10^7
M_\bullet [$\times 10^9 M_\odot$]					
BH-0	BH-1	BH-2	BH-3	BH-4	BH-5
-	0.85	1.7	3.4	5.1	6.8
BH-6					7.5

Table 4.1: Physical properties of the seven different progenitor galaxies used in the simulations by Rantala et al. (2018).

M_\star : Stellar mass

R_e : 2D projected Effective radius

M_{DM} : Dark matter halo mass

$f_{\text{DM}}(r_{1/2})$: The fraction of dark matter mass from the total mass inside the half-mass radius

N_\star : Number of stellar particles

N_{DM} : Number of dark matter particles

M_\bullet : Central SMBH Mass

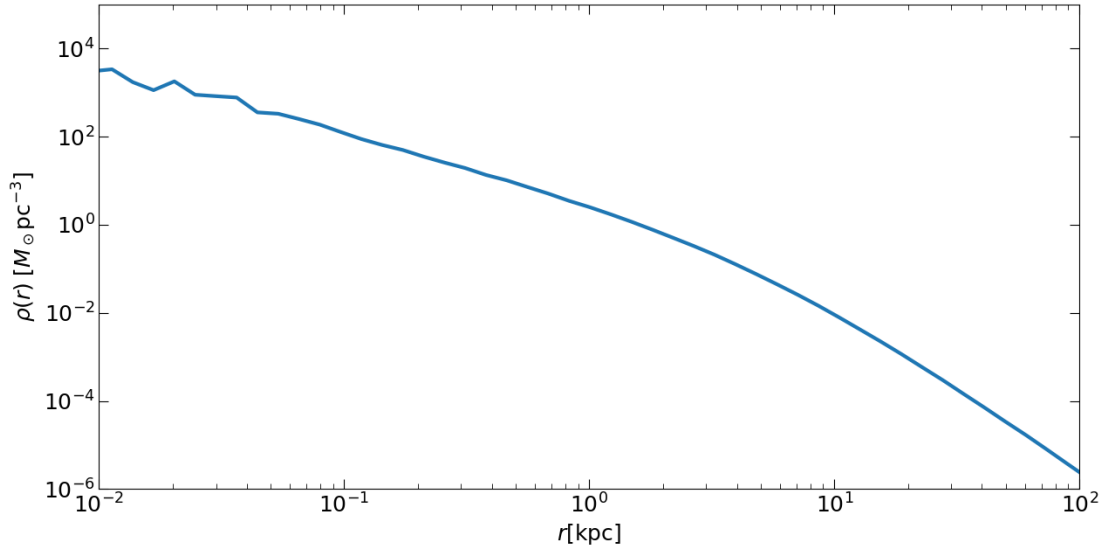


Figure 4.1: An example of the mass density profile of the progenitor galaxies. The initial conditions for the profile in question were the same as in table 4.1; with the exception of the number of dark matter and stellar particles, which were only 10% of their respective values. The noise in the left-side of the profile is caused by this low particle sample.

orbit makes the approach of the galaxies swift, and causes the stellar cusps to merge before $t \sim 300$ Myr.

The simulation data that I will be analysing, comes in the form of snapshots of the merger remnants. These snapshots are taken at the simulation time of ~ 2 Gyr. At this point the progenitor galaxies have merged into a single merger remnant, however, their central SMBHs have not yet merged and still exist in the form of a central binary. The snapshots contain the positions, velocities and masses of every particle.

4.2 Core Size Measurements

In order to test if a galaxy is cored, I calculate its surface brightness profile and check if the centre of the galaxy is deficient in light.

The surface brightness profiles are calculated from the merger remnant snapshots using the following procedure. First, the coordinate system is changed to centre-of-mass coordinates, and the stellar particles are projected onto a 2D plane. Next, we calculate the mass inside logarithmically spaced radial bins, and get a radial surface mass density profile. This is repeated 100 times from random viewing angles, which naturally results in 100 slightly different density profile projections. These profiles are then averaged azimuthally, which results in a smooth surface mass density profile. Finally, by assuming a mass-to-light ratio for the stellar particles, the surface mass density profile can be turned into a surface brightness profile (Rantala et al., 2018).

Determining the mass-to-light ratios of the stellar particles in the simulated merger remnants is problematic, as the simulations do not contain information about their ages and metallicities. The only properties that the stellar particles have are their position, velocity, and a mass that is identical for all of them. These are not enough to make valid, physically accurate, assumptions on their specific mass-to-light ratios. For this reason, a constant mass-to-light ratio of $M/L = 4$ is used. This is equivalent to the ratio derived from dynamical modelling of NGC 1600 by Thomas et al. (2016). Thus, the use of this particular M/L in the analysis of the simulation results, fits in well with the already established desire of similarity between the physical properties of the simulated merger remnants and NGC 1600.

Figure 4.2 shows the surface brightness profiles of every simulated merger remnant. Studying the curves, one can already see that, the presence of central SMBHs in the merger progenitors causes a clear brightness deficit near the centre of

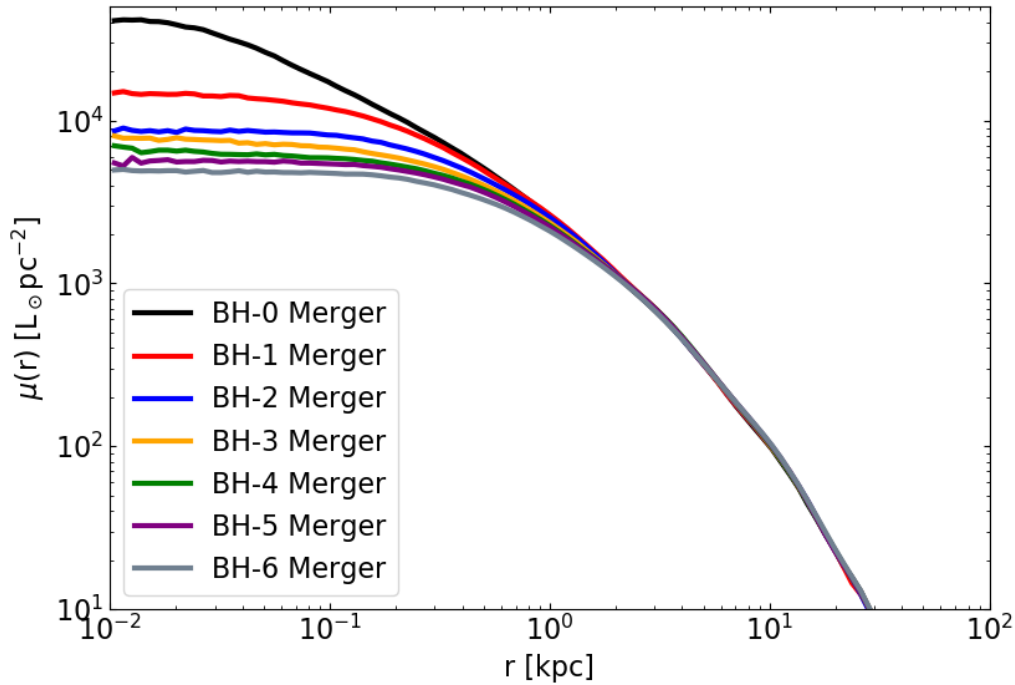


Figure 4.2: Surface brightness profiles from every simulated merger remnant. These were calculated by dividing the stellar particles in the simulated galaxy remnants into 100 radial logarithmic bins, and averaging the surface brightnesses inside these bins through 100 random viewing angles. The luminosity of the particles was estimated by assuming a constant mass-to-light ratio of $M/L = 4$.

the merger remnant. In addition, there is a systematic effect which shows that the larger the mass of the central black hole binary, the larger the amount of missing light in the core.

The lack of light in the surface brightness profiles reveals the presence of cores; however, determining the precise sizes of the cores requires us to find the exact locations where the profiles start to deviate from a Sérsic-profile fit (see section 2.2 for further discussion). Thus, we calculate the core radii of the merger remnants by using the "Levenberg-Marquardt" fitting algorithm to fit both a core-Sérsic model (equation 2.5) and a Nuker model (equation 2.7) to their surface brightness profiles. For the most part, the initial guesses used for the values of the fitting parameters in the fitting algorithm, were determined through trial-and-error, as well as knowledge of their likely order of magnitude. This was not the case for the Sérsic-index (n) in the core-Sérsic profile however. In order to reduce degeneracy between the fitting parameters, n was fixed to $n = 4$ for all core-Sérsic profile fits.

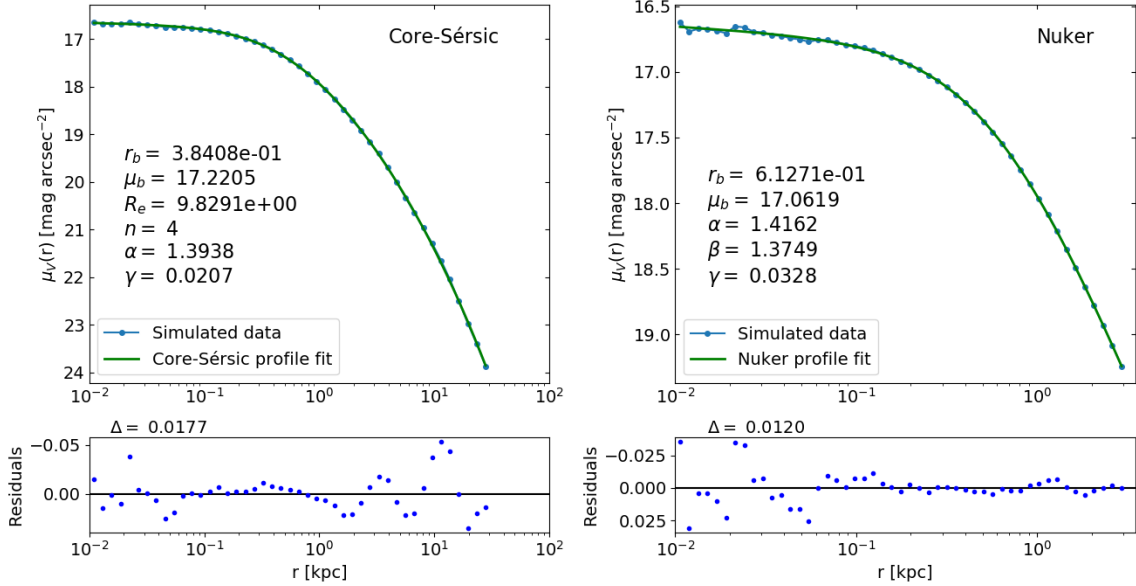


Figure 4.3: Core-Sérsic and Nuker profile fits of surface brightness profiles calculated from the BH-3 merger remnant (left and right figures respectively). The best fit parameters are shown on the figures and are in the same units as the axes (i.e. r_b and R_e in kilo-parsecs, and μ_b in V-band magnitudes per arc-second squared). The relative residuals of the fits are plotted under their respective figures. The delta (Δ) shows the root-mean-square of the residuals.

Figure 4.3 shows a comparison between the core-Sérsic and Nuker profile fits for the BH-3 merger (refer to table 4.1), while figures 4.4 and 4.5 show these fits for every simulated remnant containing an SMBH binary. The values of the best-fit parameters are shown on the figures. The units of the surface brightness are changed from $L_\odot \text{ pc}^{-2}$ to mag arcsec $^{-2}$ (where mag is the magnitude in the V-band) using the common conversion formula:

$$\mu = M_\odot + 21.572 - 2.5 \log(I), \quad (4.9)$$

where M_\odot is the absolute magnitude of the Sun in a specific spectral band (in our case the V-band magnitude of 4.83 is used), and I is the surface brightness in $L_\odot \text{ pc}^{-2}$. The relative residuals of the fits are plotted under their respective surface brightness profiles.

The root-mean-square of the relative residuals of the fits are comparable to the values seen in profile fits of observed surface brightness profiles: $\Delta \approx 0.02 \text{ mag arcsec}^{-2}$ (Dullo & Graham, 2012). However, while the RMS of the residuals show that the fits describe the surface brightness profiles rather well, most of the fits have large residual scatter near the centre of the merger remnant. This scatter is especially noticeable in the Nuker fits, since in order to get sensible values for the fitting parameters, the fitting range needs to be concentrated in the galactic centre (in our

analysis, the fitting range used for the Nuker profile was: $\sim 0.04 - 3$ kpc, which is an order of magnitude lower compared to the range used for the core-Sérsic fit: $\sim 0.04 - 60$ kpc).

The larger central residual scatter is most likely not indicative of any kind of physical structure in the merger remnant cores; but simply a result of the logarithmic spacing of the bins in the surface brightness profiles. The bins near the centre inherently contain less particles than the outer bins. When calculating the 100 projected surface brightness profiles from random viewing angles, this causes the variations in binned luminosities to be larger in the central bins, resulting in a final averaged profile that contains small jumps as well as small dips in its central luminosity. These arbitrary inconsistencies naturally cause the residuals of the fits to be scattered in a random way near the centre of the simulated galaxy. Unfortunately, remedying this problem by using bins that have a constant number of particles did not yield satisfactory results, due to the total number of particles being extremely small near the centre.

Interestingly, all of the core-Sérsic fits show a peak in the size of the residuals at around ~ 10 kpc. Once again, this residual property is probably just a small anomaly in the simulations and not indicative of any physical structure that could be found in actual merger remnants. However, the fact that this residual anomaly appears in the surface brightness profile of every simulation, indicates that; even though the masses of the SMBHs in the merger progenitors have a large effect on the central regions of the merger remnant, the outer regions are left relatively unaffected. In fact, the central SMBH binary only affects the outer regions of the merger remnant through stellar particles that have been ejected from the galactic centre.

All of the significant residual variations between the profile fits of the simulated merger remnant galaxies are concentrated near their respective centres. This implies that the results of the different simulations vary significantly from each other only due to the formation of a central SMBH binary, since the similar shapes of the outer regions of the residual plots can be explained through the limited range of the gravitational spheres-of-influence (SOI) of the binaries. The 2D projected radii of the SOI of the simulated SMBH binaries can be seen in table 4.2. These radii were calculated by finding the radius of a sphere (centred at the centre-of-mass of the host galaxy) that contains the amount of stellar mass equivalent to the mass of the SMBH binary. The projected sizes of the radii were determined through a similar relation to the one described in equation 4.3.

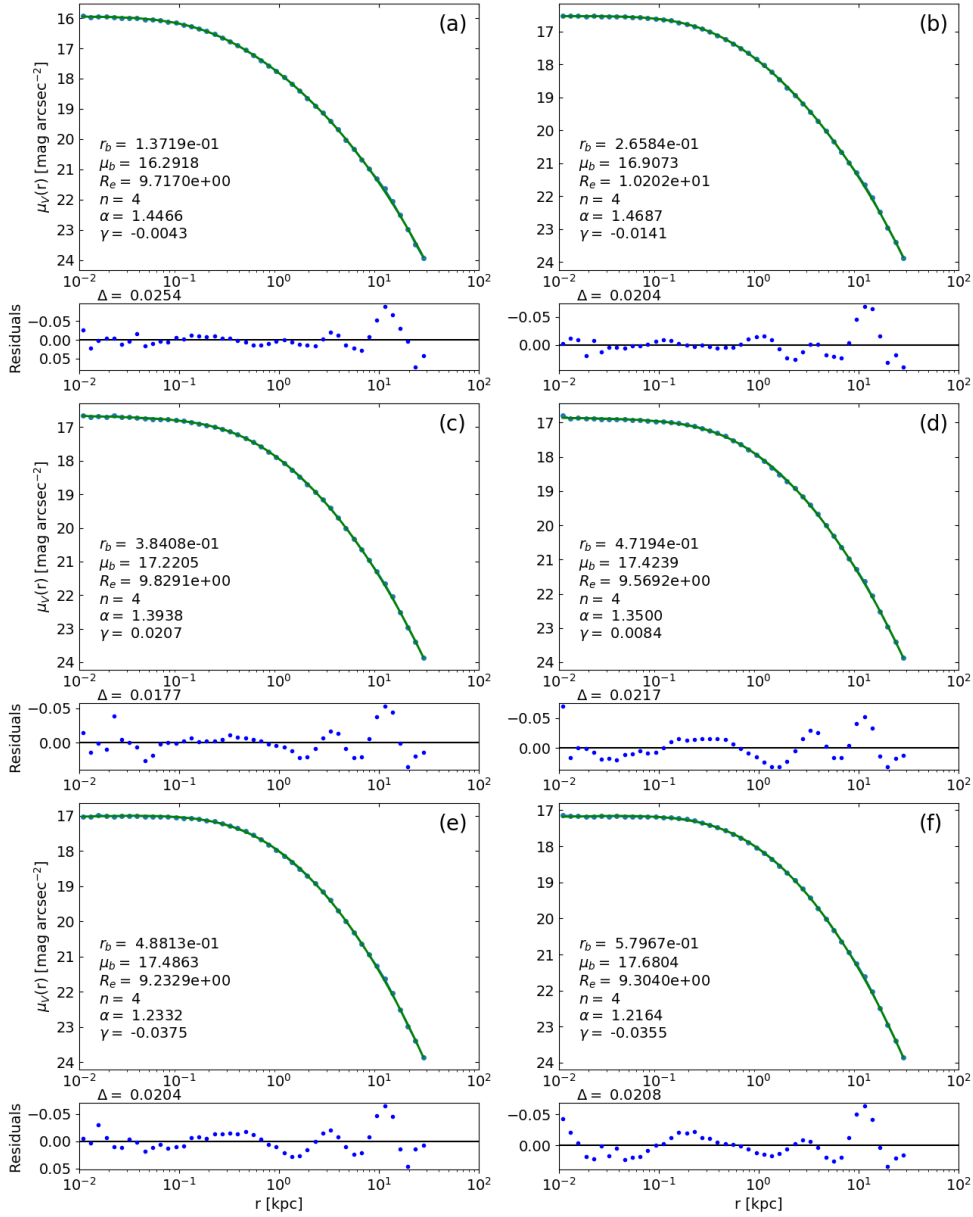


Figure 4.4: Core-Sérsic profile fits of the binned surface brightness profiles of all of the individual simulated merger remnants with progenitors that contained central supermassive black holes. The letters (a)-(f) denote the different snapshots ((a): BH-1 merger, (b): BH-2 merger, (c): BH-3 merger, (d): BH-4 merger, (e): BH-5 merger, (f): BH-6 merger).

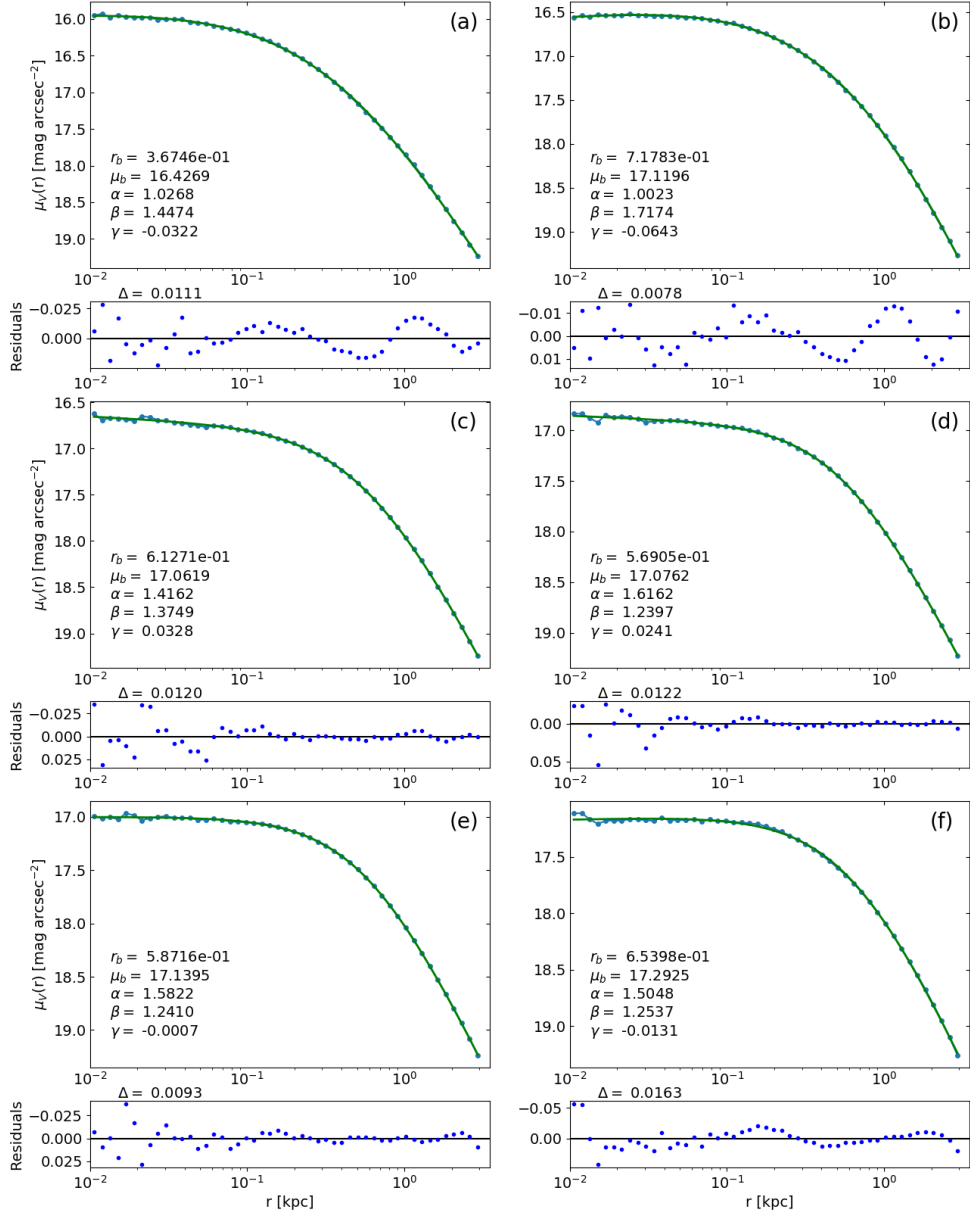


Figure 4.5: Nuker profile fits of the binned surface brightness profiles of all of the individual simulated merger remnants with progenitors that contained central supermassive black holes. The letters (a)-(f) denote the different merger remnants ((a): BH-1 merger, (b): BH-2 merger, (c): BH-3 merger, (d): BH-4 merger, (e): BH-5 merger, (f): BH-6 merger).

Simulation	r_{SOI} [kpc]
BH-1 merger	0.143
BH-2 merger	0.256
BH-3 merger	0.394
BH-4 merger	0.515
BH-5 merger	0.620
BH-6 merger	0.757

Table 4.2: Estimations of the projected radii of the spheres-of-influence (r_{SOI}) for every SMBH binary. They were calculated by finding the radius of, a sphere that contains the amount of stellar mass equivalent to the mass of the binary, inside the binary’s host merger remnant. The 2D projections of the radii were determined by using a relation similar to the one described in equation 4.3.

Figures 4.4 and 4.5 show that the core radius estimate depends quite strongly on the used model. Whether the core-Sérsic or the Nuker model is better for estimating the size of the core is still a matter of debate (Lauer et al., 2007a; Dullo & Graham, 2012). While the RMS of the relative residuals seems to be consistently (although just marginally) smaller when using the Nuker model, the best-fit value for r_b has been found to be strongly dependent on the fitting range (Graham et al., 2003). Furthermore, in order to get sensible values for every parameter of the Nuker model, its fitting range has to be narrowed down closer to the galactic centre. An example of a parameter that requires such a fitting range is the α -parameter. Rantala et al. (2018) find that, when trying to fit the Nuker model over the same radial range as the core-Sérsic model, the parameter in question gets values of $\alpha \lesssim 1$, which as Graham et al. (2003) explain, may prevent the model from describing the profile as a combination of two power-laws. This dependence that the parameters have on the model fitting range, shows that the core radius estimations of the Nuker model can be inconsistent.

In addition to the core radii derived through model fitting, we provide a third estimation for the size of the core, by calculating the cusp radius r_γ (see section 2.2) for all of the merger remnants with central SMBH binaries (BH-1 - BH-6 mergers). These are derived by calculating the gradient of the surface brightness profiles, and using a function minimization algorithm (Nelder & Mead, 1965) to minimize the difference $\left| \frac{d\mu(r)}{dr} - \left(-\frac{1}{2} \right) \right|$. This allows us to find the radius, at which the gradient gets the value $-1/2$.

Figure 4.6 compares the core radius estimates from each of the three meth-

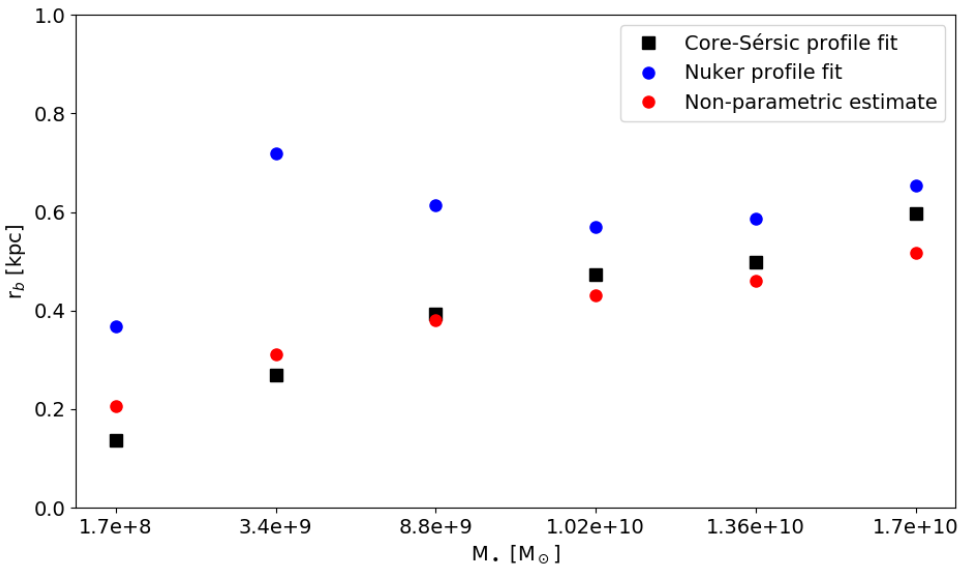


Figure 4.6: Comparison of the different core radius estimates of the merger remnants. These estimates were derived through three different methods: Core-Sérsic profile fitting (black squares), Nuker profile fitting (blue circles) and finding the "cusp radius" (red circles). The x-axis shows the masses of the central SMBH binaries in the merger remnants.

ods for every simulated merger remnant. The break radii from the Nuker fits are consistently larger than the other core radius estimates. They also have, in general, the largest deviations from the other core radii, and even contain two values that seem to break the trend of the core radius growing with the central SMBH binary mass (these being the break radii for the BH-2 and BH-3 mergers). Similar larger than expected Nuker core radii can be seen in the analysis of the simulations by Rantala et al. (2018). Like in figure 4.6, the difference in the Nuker break radii and the other core radius estimates for the two mergers with the smallest and third smallest central SMBH binaries, are significantly larger than for the other mergers. The fact that these large deviations are present in both our analysis and the analysis by Rantala et al. (2018), further implies that, due to its high dependence on the fitting range, the Nuker model can provide inconsistent values for the break radius. However, when excluding these few Nuker break radii, a clear trend of the size of the core growing with the merger progenitors' central SMBH masses can be seen.

The fact that the size of the core is dependent on the mass of the central SMBH binary is clear evidence towards the cores being formed through a scouring process by the binary black holes. Binaries with larger masses have larger gravitational spheres-of-influence (table 4.2), which naturally leads to the ejection of stellar particles that

orbit farther away from the galactic centre (the larger SMBH binary mass also causes the stellar material to be ejected at a larger velocity).

This positive correlation between the core size and the SMBH binary mass has also been identified in independent measurements of the break radius and the central SMBH mass in cored galaxies (e.g. de Ruiter et al., 2005; Lauer et al., 2007b; Thomas et al., 2016). The fact that this effect can be seen, not only in the simulations, but also in the observations, makes it clear that merging SMBH binaries are a likely source for the observed cores.

Alongside the size of the core, the surface brightness deficit also becomes larger as the central SMBH binary mass grows (figure 4.2). This can be explained through the concept of the loss-cone. The condition that defines the loss-cone (equation 2.11) shows, that the maximum angular momentum at which a star can interact strongly with the binary, grows alongside the masses of the black holes. This means that, a larger SMBH binary mass causes more of the orbiting stellar particles to be located in the strong interaction range; as not only does the loss-cone widen, allowing for the ejection of particles with orbits more parallel to the plane of the binary; but the maximum velocities, at which a stellar particle can interact strongly with the binary, also become larger. Thus, a more massive central SMBH binary naturally results in the ejection of a larger number of stellar particles, which then leads to the growth of the central surface brightness deficit.

4.3 Velocity Anisotropy

Another method of studying whether a galaxy has formed a core through core scouring by binary black holes, is to study the velocity anisotropy profile defined in Binney & Tremaine (2008) as:

$$\beta(r) = 1 - \frac{\sigma_\theta^2 + \sigma_\phi^2}{2\sigma_r^2} = 1 - \frac{\sigma_t^2}{\sigma_r^2}, \quad (4.10)$$

where σ_θ , σ_ϕ and σ_r are one-dimensional velocity dispersions in the spherical coordinates, and $\sigma_t = \sqrt{(\sigma_\theta^2 + \sigma_\phi^2)/2}$ is the tangential velocity dispersion. This β -parameter describes the ratio of tangential velocity dispersion in the stellar system to the radial velocity dispersion and, as such, provides information about the nature of the stellar orbits around the black hole binary. A negative value for β shows an abundance of tangential orbits, whereas a positive β corresponds to an abundance of radial orbits.

Figure 4.7 shows β -profiles calculated from all of the final merger remnant snapshots using equation 4.10. In order to get the velocity dispersions, the stellar

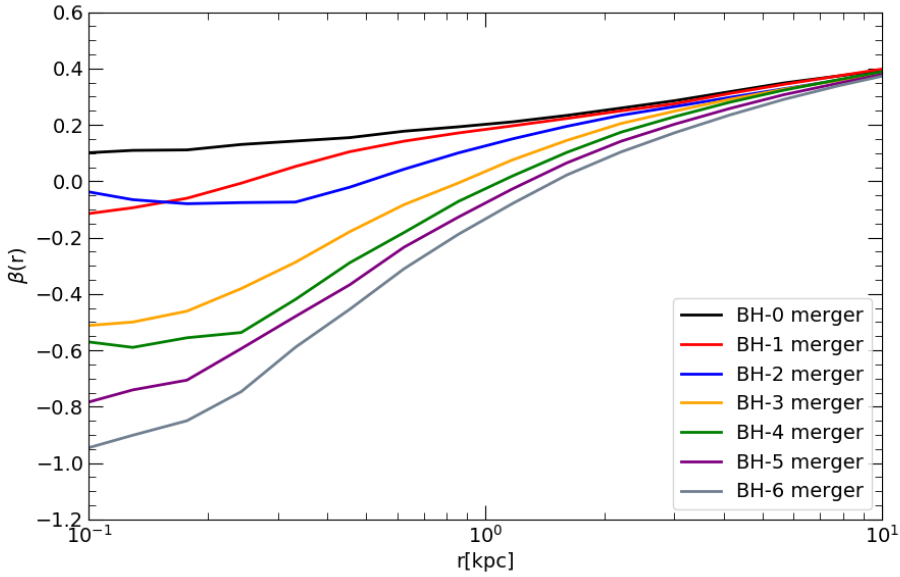


Figure 4.7: Velocity anisotropy (β) profiles for every simulated merger remnant. The profiles are calculated from the velocity dispersions in radial logarithmic bins, using equation 4.10. Going from the outer regions to the central regions of the merger remnants, the profiles of the remnants with SMBH binaries go from being radially dominated to being tangentially dominated.

particles of the remnants were first divided into logarithmic bins, and their velocities were changed from a Cartesian to a spherical coordinate system. Next, the root-mean-squares, which correspond to the velocity dispersions, of the different spherical velocity components were calculated for each bin separately, resulting in a β -value for every bin. Plotting these values gives us the aforementioned profiles in figure 4.7.

According to the β -profiles, the outer areas of the remnants are dominated by radial orbits (positive β), while the majority of orbits near the centre are tangential (negative β). As the initial merger progenitors used in the simulations contained isotropic β -profiles ($\beta = 0$), an area with negative β in the merger remnant would imply that the stars on radial orbits have been lost from the system. It has been shown that hardening black hole binaries can eject stars on highly radial orbits from the galactic core, which results in the central region becoming dominated by mostly tangential orbits (and thus a negative β). The ejected stars can then, in turn, cause the outer orbits to become more radial (Quinlan & Hernquist, 1997; Milosavljević & Merritt, 2001; Thomas et al., 2014).

Figure 4.7 clearly shows that the presence of an SMBH binary has an effect

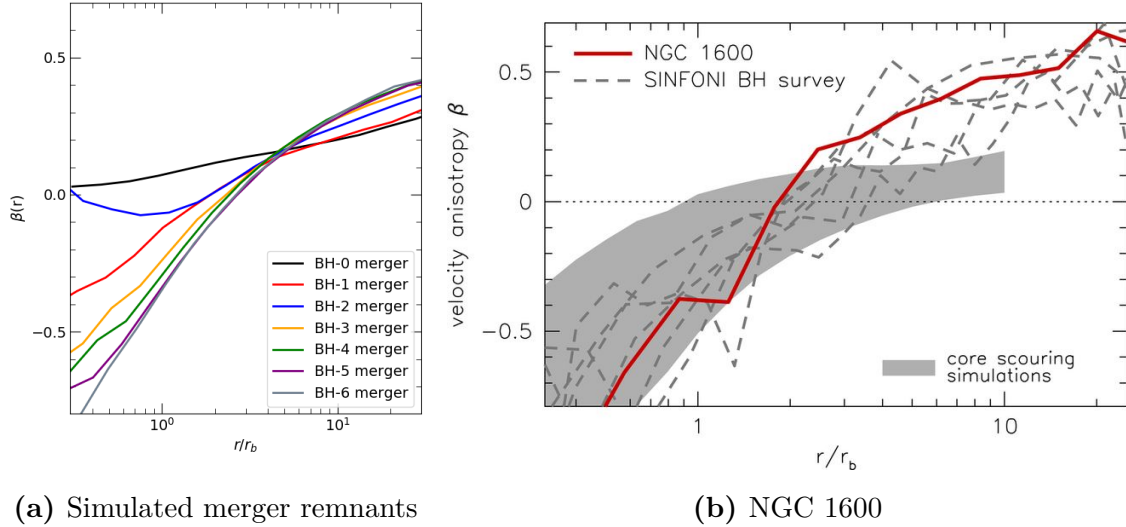


Figure 4.8: (a): The β -profiles of the simulated merger remnants as a function of distance from the centre, scaled by their respective break radius. For the merger remnant without a core (BH-0), the value used for the break radius is $r_b = 1$ kpc. The profile for the BH-2 merger shows an increase in the value of β near the centre of the merger remnant, which is simply the same increase seen in figure 4.7, amplified by the break radius scaling. (b): β -profile of NGC 1600, alongside profiles of galaxies from the SINFONI black hole survey (Saglia et al., 2016) and the range of possible anisotropies found in N-body simulations of the core scouring mechanism (Thomas et al., 2016).

on the shape of the β -profiles. Not only is the slope of the profile steeper for merger remnants which contain a more massive central SMBH binary, but the only merger with a profile that is completely dominated by radial velocity dispersion, is the one without a central SMBH binary (the BH-0 merger). The shapes of these profiles make sense in the context of ejection of stellar particles by hardening black hole binaries. The larger the mass of the SMBH binary, the larger its gravitational sphere-of-influence, which results in more of the radially orbiting stellar particles being ejected.

Figure 4.8 shows, both the observed β -profile of NGC 1600 and the profiles from our simulated merger remnants. The profiles in the figure are scaled by the core radius of the respective galaxy. Even by eye, it can clearly be seen that the β -profiles from both the simulations and the observations of NGC 1600 are similar to each other (not counting the anomalous profile for the BH-2 merger). However, looking closely at the values on the axes of the plots, the observed profile of NGC 1600 seems to be somewhat steeper when compared to the simulated ones.

According to Rantala et al. (2018), the kinematics being more tangential close to the core in NGC 1600 than in the simulations, could be caused by further adia-

batic growth of the merged central SMBH’s mass. Young (1980) shows that black holes that grow adiabatically through, for example accretion of gas, can cause the surrounding stellar orbits to become more tangential. If the time scale of the mass growth is smaller than the relaxation time scale of the galaxy while also being larger than the dynamical time scale of the stellar system, the growth can be considered adiabatic. This results in the conservation of the angular momentum and the radial action of the stellar orbits (radial action being one of the momenta in the canonical Hamiltonian coordinates called *angle-action variables*; Binney & Tremaine 2008), which, due to the now higher gravitational potential induced by the central black hole, causes the orbits to become more circular. Although this effect is not strong enough to account for the entire shape of the β -profile (Thomas et al., 2016), it could certainly be a reason for the more tangentially dominated core regions seen in the observations.

As for the outer region of the β -profile of NGC 1600, it is possible, that the reason why it is more radially dominated than the outer parts of any of the simulated merger remnants, is due to the lack of minor-mergers in the simulations (Rantala et al., 2018). These minor-mergers would deposit all of their mass in the outer regions of the galaxy, and would thus disrupt only the outer stellar orbits, making some of the more tangential of these orbits more radial. Furthermore, they would not contribute to the destruction of radial orbits near the centre of the galaxy, as the smaller progenitor galaxy would not contain a central SMBH.

4.4 Line-of-Sight Kinematics

4.4.1 2D Kinematic Maps

In order to make sure that the KETJU simulations produce results that are in agreement with observations, I also analyse the line-of-sight (LOS) kinematics of the simulated merger remnants. The analysis is focused on the four different LOS velocity distribution (LOSVD) parameters: the average LOS velocity V_{avg} , the velocity dispersion σ , and the h_3 and h_4 parameters (see section 2.4).

The above LOSVD-properties are calculated using a Python-script (Matteo Frigo, internal communication), which makes use of the Voronoi tessellation algorithm by Cappellari & Copin (2003). It provides binned statistics of the LOS velocities, and forms 2D kinematic maps similar to ones provided by integral-field units (IFU-maps), in order to help visualise the LOSVD properties. First, when

using the script, the "line-of-sight" is defined as the intermediate axis of the merger remnant, after which a 2D line-of-sight projection of the remnant is produced, by orienting it accordingly using the inertia tensor. The 2D projection is then divided into "spaxels" using the aforementioned Voronoi tessellation algorithm. The shape and size of the spaxels are determined so that each one contains the same signal-to-noise ratio, which in our simulated case is defined as the number of stellar particles. The LOS-velocities inside the spaxels are then made into a histogram, into which the modified Gaussian function described in equation 2.20 is fitted. This gives the values of the LOSVD parameters: V_{avg} , σ , h_3 and h_4 for the spaxel in question. Finally, the values of the spaxels are plotted, resulting in 2D Voronoi binned IFU-maps of all of the four parameters.

Figure 4.9 shows the voronoi binned 2D maps of the four LOS velocity distribution parameters for the simulated BH-0 merger (no central SMBH) and the BH-6 merger (largest central SMBH), as well as for two observed galaxies NGC 3414 and NGC 4111, which are known slow and fast rotators, respectively. The contours, which are added to help visualise the shape of the galaxy, denote flux isophotes of the merger remnants, and have a spacing of one magnitude. Similar maps for the rest of the simulated merger remnants can be seen in figure 4.10. Figure 4.10 shows the IFU-maps of the four LOS-velocity parameters for the rest of the simulated merger remnants.

The IFU-maps in figures 4.9 and 4.10 show that the average LOS velocities of the simulated merger remnants are far from isotropic, with most of the remnants that contain central binary SMBHs showcasing KDCs. Some of the simulated remnants (BH-4 - BH-6 mergers) even contain a clear counter rotating structure inside the KDC (Rantala et al., 2019). These features, alongside the relatively low average LOS-velocities, imply that all of the merger remnants are likely slow rotators. Since slow rotator galaxies are assumed to have been formed through gas-poor "dry" mergers, processes not unlike the ones simulated in our simulations, this is a somewhat expected result.

The velocity dispersion maps in figures 4.9 and 4.10 show a clear connection between the mass of the central SMBH binary and the velocity dispersion at the centre of the galaxy. The presence of an SMBH binary causes the formation of a central velocity dispersion peak in the σ -distribution, the strength of which correlates positively with the mass of the binary. Furthermore, as the mass of the SMBH binary grows, the size of the area with the highest velocity dispersion in the galaxy also grows. Additionally, the growing binary mass seems to cause the high- σ area to get

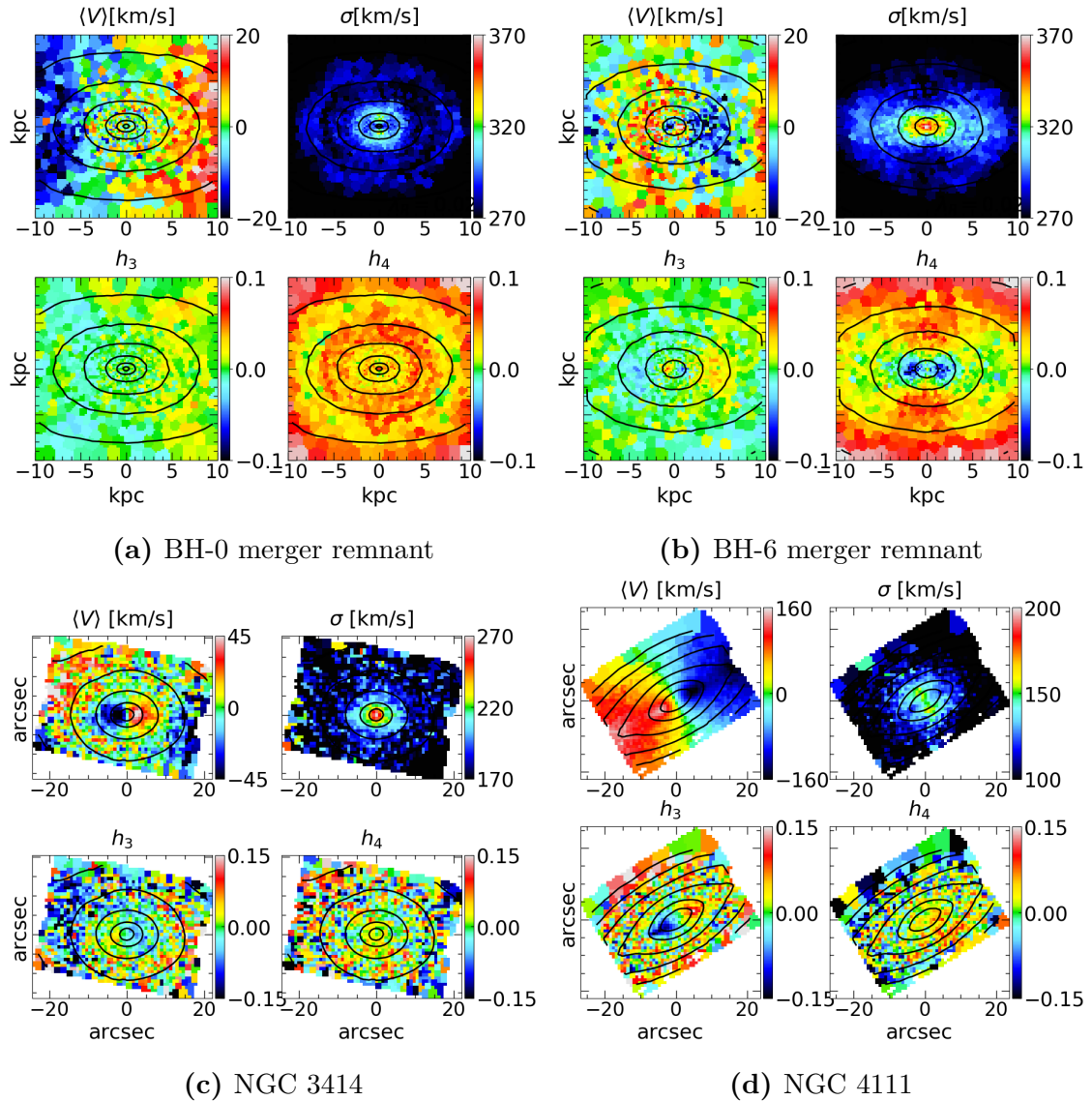


Figure 4.9: IFU-maps of average LOS-velocities, velocity dispersion, h_3 parameters and h_4 parameters from two simulated merger remnants and two observed galaxies. The four maps in figure (a) are from the BH-0 merger, and the four in figure (b) are the BH-6 merger. Figures (c) and (d) show IFU-maps of known slow (NGC 3414) and fast rotator (NGC 4111) galaxies from the ATLAS^{3D} survey (Emsellem et al., 2004; Cappellari et al., 2011; Krajnović et al., 2011).

more and more aligned with the major-axis of the galaxy. Most of these effects can easily be identified when comparing the IFU-maps of the different simulated merger remnants from figure 4.10. The formation of the velocity dispersion peak, which is simply caused by the presence of the SMBH binary, is clearly demonstrated in the IFU-maps of the BH-0 and BH-6 merger remnants in figure 4.9. The positive correlation between the mass of the central SMBH (or in the case of the simulations: central SMBH binary) and the velocity dispersion of its host galaxy, is a clear indication of the $M_{\bullet} - \sigma$ relation discussed in section 2.3.6, and which has been observed in a multitude of galaxies with central SMBHs, both cored and non-cored (Ferrarese & Merritt, 2000).

Apart from the BH-0 merger remnant, the h_3 -parameter values in the IFU-maps of the simulated merger remnants show an anti-correlation with the average LOS-velocity. Indeed, Krajnović et al. (2011) have found that, while the anti-correlation between the LOS velocities and the h_3 -parameter is mostly found in fast rotators (see central region of the fast-rotator NGC 4111 in figure 4.9), some galaxies with CRCs also exhibit this behaviour. Thus, this anti-correlation can be seen in for example the slowly rotating NGC 3414 in figure 4.9. Looking at the simulated merger remnants, this anti-correlation seems to be more pronounced in the remnants that contain a more massive the central SMBH binary. Furthermore, the larger binary mass seems to also make the counter-rotating central regions in the remnants clearer. Thus, there is a clear correlation between the degree of anti-correlation and the existence of CRCs in the simulated remnants, making the simulated KETJU results once again agree with observations.

The h_4 -parameter roughly corresponds to the velocity anisotropy parameter β , where a negative value of h_4 identifies areas with a large tangential velocity dispersion, and a positive identifies areas with a more radial velocity dispersion (Gerhard, 1993; Gerhard et al., 1998; Thomas et al., 2007). Comparing the β -profiles from figure 4.7 with the h_4 IFU-maps from figures 4.9 and 4.10, this certainly seems to be the case. For the merger remnants with central SMBH binaries, both the β and the h_4 values are largely positive in the outer regions of the galaxy, while being negative closer to their centres. The h_4 map of the BH-0 merger is then positive all around, exactly like its β -profile. The h_4 maps of NGC 3414 and NGC 4111 (figure 4.9) do not contain any specific structures and seem to be completely isotropic. As the negative h_4 -areas in the IFU maps of the simulated merger remnants are likely caused by core scouring, and as neither of the observed galaxies are cored galaxies (Lauer et al., 2007a); they most likely have not experienced such a process, making

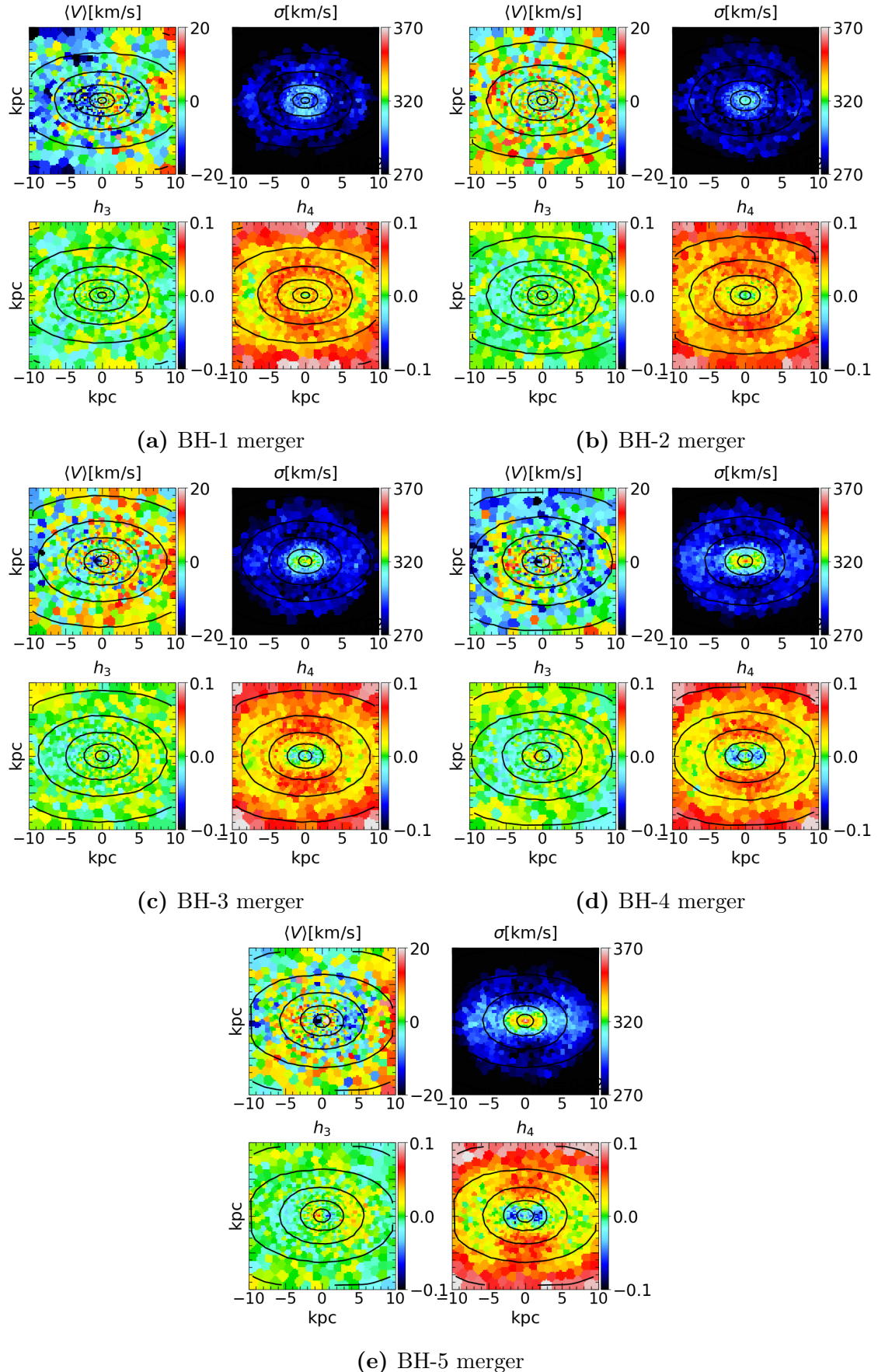


Figure 4.10: IFU-maps of average LOS-velocities, velocity dispersion, h_3 parameters and h_4 parameters from four simulated merger remnants: BH-1, BH-2, BH-3, BH-4 and BH-5 mergers.

the lack of clear structures understandable.

4.4.2 The λ_R -parameter

Further analysis of the kinematics of the simulated merger remnants can be done by studying the λ_R parameter (equation 2.23), which allows us to determine whether the galaxies are slow or fast rotators. We use the Voronoi binned statistics from the IFU-maps to calculate λ_R at the effective radius (λ_{Re}). These are then compared to the three slow rotator thresholds described in section 2.4.1:

$$\begin{aligned}\lambda_{Re} &< 0.1, \\ \lambda_{Re} &< 0.31\sqrt{\epsilon_e}, \\ \lambda_{Re} &< 0.08 + \epsilon_e/4,\end{aligned}\tag{4.11}$$

where ϵ_e is the ellipticity of the remnant at the effective radius.

As two of the three slow rotator thresholds require us to know the ellipticity of the galaxy, I wrote a program in Python that calculates ellipticities of the simulated merger remnants. These ellipticity calculations are done using a method described in Zemp et al. (2011), which uses the shape tensor:

$$\mathbf{S} = \frac{\int_V \rho(\mathbf{r})\omega(\mathbf{r})\mathbf{rr}^T dV}{\int_V \rho\mathbf{r} dV},\tag{4.12}$$

where \mathbf{r} is position from the galactic centre, $\rho(\mathbf{r})$ is the mass density, V is the volume of an enclosed ellipsoid with the elliptical radius r_{ell} , and where the weighting function $\omega(\mathbf{r}) = 1$. The eigenvalues of the shape tensor correspond to $a^2/3$, $b^2/3$ and $c^2/3$; where a , b and c are the semi-principal axes. The parameters a and b correspond to the semi-major and semi-minor axes, respectively, and can be used to calculate the ellipticity (equation 2.1).

Simply calculating the shape tensor and getting the correct eigenvalues is not possible, as the elliptical radius r_{ell} is defined, in part, using the axis ratios a/b and a/c :

$$r_{\text{ell}} = \sqrt{x_{\text{ell}}^2 + \frac{y_{\text{ell}}^2}{(b/a)^2} + \frac{z_{\text{ell}}^2}{(c/a)^2}}.\tag{4.13}$$

This means that we have to turn the calculation into an iterative process by starting with $b/a = c/a = 1$ for the initial value of r_{ell} , and calculating new shape tensor eigenvalues using previously gained axis ratios until the values of the ratios start to converge, and the difference between two subsequent axis ratios falls below some pre-defined convergence criterion.

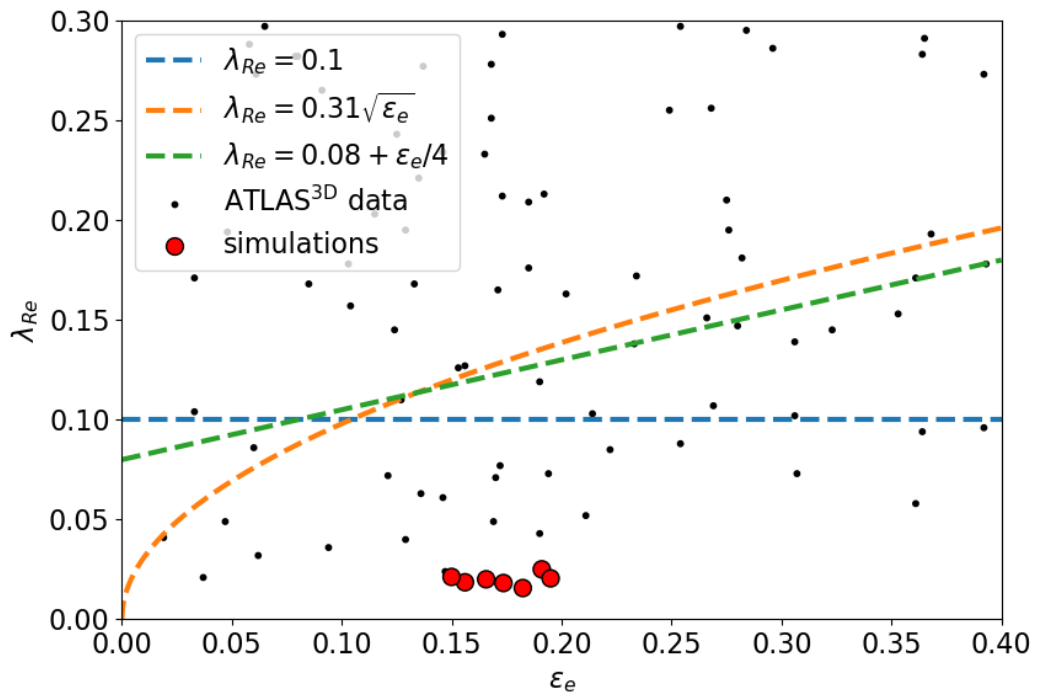


Figure 4.11: Values of the λ_{Re} -parameter of galaxies, plotted against their ellipticity at the effective radius. The red dots correspond to the simulated merger remnants, whereas the black dots correspond to galaxies observed in the ATLAS^{3D}-survey (Cappellari et al., 2011; Emsellem et al., 2011). The dashed lines display different slow rotator thresholds as a function of ellipticity (Emsellem et al., 2007, 2011; Cappellari, 2016).

Plotting λ_{Re} and ϵ_e against each other (the ellipticity is calculated using $r_{\text{ell}} = R_e$, and a convergence criterion of a difference smaller than 10^{-3} between consequent axis ratios), alongside the slow rotator thresholds and observed values from the ATLAS^{3D}-survey (Cappellari et al., 2011), gives us figure 4.11. Regardless of the threshold used for differentiating between slow and fast rotators, the figure shows that, all of the simulated merger remnants are clearly classified as slow rotators. This agrees well with the kinematic anisotropies seen in the IFU-maps, which also implied a slow rotator classification for the remnants.

4.5 Comparison to Observations

As the physical properties of the merger progenitors are modelled after NGC 1600, it is interesting to see how the results from the simulations compare with actual observations of the galaxy. While I will be comparing the observations mainly to the BH-6 merger remnant, as the mass of the SMBH binary in the simulated galaxy is equivalent to the observed and modelled mass of the central SMBH in NGC 1600 ($M_\bullet = 1.7 \times 10^{10} M_\odot$) (Thomas et al., 2016); I will also be comparing the observed properties of the cored massive elliptical galaxy NGC 4472 to the simulated BH-1 merger remnant. Both of the latter galaxies have similar central black hole masses (or in the case of the simulated remnant, black hole binary mass), as well as similar total stellar masses. Thus, comparing their other physical properties could provide some interesting insight into the formation of cores.

Figure 4.12 shows core-Sérsic profile fits of the surface brightness profiles from the BH-1 and BH-6 mergers, and compares them to the profile fits from the observed core galaxies NGC 4472 and NGC 1600 respectively. Not only do the shapes of the compared photometric profiles follow each other closely in both cases, the best-fit parameters are also quite closely related (table 4.3).

Another comparison between some of the properties of the four galaxies can be seen in table 4.4. Most importantly, the table shows that the kinematic properties of the simulated merger remnants and the kinematic properties of NGC 1600 are very similar. On the other hand, compared to the three other galaxies, the spin parameter and line-of-sight velocity of NGC 4472 are almost an order of magnitude larger. Furthermore, like the simulated galaxies, NGC 1600 can easily be identified as a slow rotator by its λ_e parameter and ellipticity, while NGC 4472 seems to be classified as a fast rotator.

Before drawing conclusion from these results, it is important to know that,

	BH-1 merger	NGC 4472	BH-6 merger	NGC 1600
r_b [kpc]	0.137	0.151	0.579	0.667
μ_b [mag arcsec $^{-2}$]	16.29	16.48	17.68	18.00
R_e [kpc]	9.717	16	9.304	16.04
n	4	5.6	4	5.83
α	1.45	3.05	1.22	2.09
γ	0.00	0.06	-0.04	0.03

Table 4.3: Best-fit parameters of the core-Sérsic profile fits seen in figure 4.12. The best-fit parameters of NGC 4472 are from Rusli et al. (2013a), while the parameters for NGC 1600 are given in Thomas et al. (2016). n is the Sérsic index, α controls the sharpness of the transition between the inner and outer profiles, and γ is the slope of the inner profile.

whether NGC 4472 is in fact classified as a fast rotator is not known for certain. Emsellem et al. (2011) found a significantly lower value for its spin parameter ($\lambda_e = 0.077$), which would easily classify the object as a slow rotator. The value used in this analysis comes from the more recent MASSIVE-survey (Ma et al., 2014; Veale et al., 2017), in which some of the inaccuracies of the previous observations were shown (e.g. not taking into account a large enough region of the observed galaxy). Conceding to some possible biases in their own calculations, Veale et al. (2017) ultimately classify NGC 4472 as an intermediate case between slow and fast rotators.

It is impressive, that the simulation of the BH-6 merger is able to reproduce both the kinematic properties and the shape of the surface brightness profile of NGC 1600 so well. Since the simulation describes a dry major merger event between two massive ETG with central SMBHs, the results imply that this process could be the formation mechanism behind core galaxies.

Interestingly, since the BH-6 merger has extremely similar kinematic properties with the BH-1 merger and NGC 1600, it can be assumed that the mass of the central SMBH binary does not affect the rotation of its host galaxy in any significant way. This suggests that, as far as the merger progenitors are concerned, it is the properties other than their central SMBH mass (i.e. them being massive gas-poor ETGs) that determine the stellar kinematics in the final merger remnant. As for NGC 4472, since both its λ_e and LOS velocity are about an order of magnitude larger compared to the three other galaxies, it can be argued that its formation history must be quite different when compare to the other galaxies. However, due to the ambiguity of whether NGC 4472 is a fast rotator and whether its spin parameter is biased towards large values, the possibility that the galaxy has also formed through a dry ETG merger, should not be ruled out.

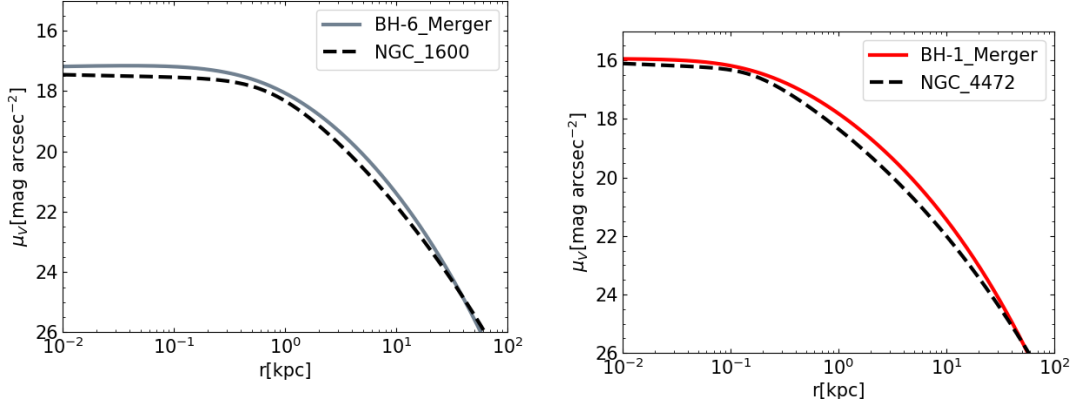


Figure 4.12: Comparison between core-Sérsic profile fits from observed galaxies and simulated merger remnants, where the surface brightness is given in V-band magnitudes. The figure on the left compares the profile of the BH-6 merger remnant (the merger remnant whose progenitors containing the largest central SMBH masses) to NGC 1600; while the figure on the right compares the profiles of the BH-1 merger remnant (the remnant with progenitors that had the smallest SMBH masses) and NGC 4472. The parameters for plotting the core-Sérsic profile of NGC 1600 were taken from Thomas et al. (2016), with the units being changed to the above, by assuming $V - R = 0.5$ (the same assumption being done in Lauer et al. (2007a)), and by using the distance $D = 64\text{Mpc}$ (Thomas et al., 2016) to define the relation between arc seconds and parsecs. The parameters for the profile of NGC 4472 were from Rusli et al. (2013a). All of the best-fit parameters can be found in table 4.3

Earlier in this chapter it was shown that there is a clear positive correlation between the central SMBH binary masses and the size of the core radii in the simulated merger remnants. However, the facts that the core radius sizes for the BH-1 merger remnant and NGC 4472 are comparable and that many of their other properties are quite different, imply that, not only is there a correlation, the SMBH binary mass might be the only property that affects the size of the core in any significant way. If this is true, it is very strong evidence that the cores are formed through a scouring process by binary SMBHs.

Galaxy	M_* [$\times 10^{11} M_\odot$]	M_\bullet [$\times 10^{10} M_\odot$]	R_e [kpc]	μ_e [mag/arcsec 2]	n	V_{LOS} [km/s]	σ_e [km/s]	λ_e	ϵ_e
(1)	(2)	(3)	(4)	(5)	(6)	(7)	(8)	(9)	(10)
BH-6 merger	8.3	1.7	10.722	21.54	4	5.61	278	0.0213	0.15
NGC 1600	8.3	1.7	~ 16	~ 22.8	5.83	7.1	293	0.026	0.32
BH-1 merger	8.3	0.17	9.879	21.42	4	5.49	274	0.021	0.195
NGC 4472	6.03	0.25	14.33	22.72	5.6	45.4	258	0.197	0.172

Table 4.4: Comparisons between the physical properties of the simulated BH-1 and BH-6 merger remnants and the observed galaxies NGC 1600 and NGC 4472 respectively. The properties described in the columns are explained below, alongside the sources for their values in NGC 1600 and NGC 4472.

- (1) Name of the galaxy.
- (2) Total stellar mass. NGC 1600: Thomas et al. (2016), NGC 4472: Veale et al. (2018).
- (3) Central SMBH / central SMBH binary mass. NGC 1600: Thomas et al. (2016), NGC 4472: Rusli et al. (2013b).
- (4) Effective radius. The values used for the simulated mergers are estimated by calculating the half-mass radius in three dimensions, and using equation 4.3 to get the approximate two dimensional effective radius. This is done instead of using the core-Sérsic profile best-fit parameter, since the core-Sérsic R_e only takes into account the specific fitting radius. NGC 1600: Thomas et al. (2016), where the value is changed from arc seconds to kpc by assuming that the galaxy is located at the distance of $D = 64$ Mpc; NGC 4472: Veale et al. (2017).
- (5) Surface brightness at the effective radius. The values for all of the galaxies are calculated from the core-Sérsic fits. The profile fits best-fit parameters are from table 4.3.
- (6) Sérsic index. NGC 1600: Thomas et al. (2016), NGC 4472: Rusli et al. (2013a).
- (7) Mean line-of-sight velocity inside the effective radius. For the the simulated mergers these values are calculated from their respective IFU maps as the mean of the V_{LOS} -values from the Voronoi-bins inside the effective radius. NGC 1600 and NGC 4472: Bender et al. (1994).
- (8) Velocity dispersion inside the effective radius. As with V_{LOS} , this value comes from the mean velocity dispersion of the Voronoi bins inside the effective radius in the IFU-maps for the simulated mergers. NGC 1600 and NGC 4472: Veale et al. (2017).
- (9) Spin parameter at the effective radius. NGC 1600 and NGC 4472: (Veale et al., 2018).
- (10) For the simulated mergers and NGC 4472: ellipticity of the galaxy at the effective radius. For NGC 1600: luminosity weighted ellipticity. NGC 1600: Goulaud et al. (2018), NGC 4472: Emsellem et al. (2011).

5. Conclusions

In this Master’s thesis, I have studied the formation of low-luminosity galactic cores in mergers of gas-free elliptical galaxies that contain a supermassive black hole in their respective centres. I analysed results from seven galaxy merger simulations done using the KETJU code, a combination of both the GADGET-3 tree code and the AR-CHAIN integrator, that can simulate both general galactic dynamics as well as precise stellar motion near SMBHs, simultaneously. Each simulation run contained two identical galaxies, the difference between the different runs being in the mass of the central SMBH.

I considered whether the cores are formed as a result of SMBH mergers. This analysis was based on calculations of the surface brightness and velocity-anisotropy profiles of the simulated merger remnants, as well as their line-of-sight velocity distributions in the form of 2D Voronoi binned kinematic maps. These properties were then compared to theoretical expectations and observations. Correlations between properties of the remnants, such as the core radius and binary mass relation, were also considered.

I find that the simulation results do point toward the cores being formed due to SMBH mergers. Barring two of the core radii derived using the Nuker-model, the sizes of the cores in the simulated merger remnants have a clear positive correlation with the SMBH binary mass, which is the most fundamental indication that the core formation is inherently linked to the central binary. Furthermore, neglecting the clearly anomalous velocity anisotropy profile of the BH-2 merger, the β -profiles seem to be affected as expected by changes in the masses of the black holes used in the simulations, with larger mass SMBHs resulting in steeper and generally more tangentially dominated profiles. The simulations also seem to produce general galactic kinematics similar to observations. The 2D kinematic maps show kinematic properties often seen in slow rotator galaxies, a classification into which the simulated merger remnants are expectedly determined to be included in. Since the results seem to agree well with the theoretical expectations of the SMBH

merger core formation model, and at most contain a few anomalous data points, I would consider this theses to be successful in its aims.

An especially i

Bibliography

- Abbott, B. P. et al. (2016). Observation of Gravitational Waves from a Binary Black Hole Merger. *Physical Review Letters*, 116(6):061102.
- Abbott, B. P. et al. (2019). GWTC-1: A Gravitational-Wave Transient Catalog of Compact Binary Mergers Observed by LIGO and Virgo during the First and Second Observing Runs. *Physical Review X*, 9(3):031040.
- Ahmad, A. & Cohen, L. (1973). A numerical integration scheme for the N-body gravitational problem. *Journal of Computational Physics*, 12:389–402.
- Bacon, R. et al. (2001). The SAURON project - I. The panoramic integral-field spectrograph. *Monthly Notices of the Royal Astronomical Society*, 326(1):23–35.
- Barnes, J. & Hut, P. (1986). A hierarchical $O(N \log N)$ force-calculation algorithm. *Nature*, 324(6096):446–449.
- Barnes, J. E. & Hernquist, L. (1996). Transformations of Galaxies. II. Gasdynamics in Merging Disk Galaxies. *The Astrophysical Journal*, 471:115.
- Barnes, J. E. & Hernquist, L. E. (1991). Fueling Starburst Galaxies with Gas-rich Mergers. *The Astrophysical Journal Letters*, 370:L65.
- Bender, R., Saglia, R. P., & Gerhard, O. E. (1994). Line-of-sight velocity distributions of elliptical galaxies. *Monthly Notices of the Royal Astronomical Society*, 269:785–813.
- Binney, J. & Tremaine, S. (2008). *Galactic Dynamics: Second Edition*. Princeton University Press.
- Bulirsch, R. & Stoer, J. (1966). Numerical treatment of ordinary differential equations by extrapolation methods. *Numerische Mathematik*, 8(1):1–13.

- Cappellari, M. (2016). Structure and Kinematics of Early-Type Galaxies from Integral Field Spectroscopy. *Annual Review of Astronomy and Astrophysics*, 54:597–665.
- Cappellari, M. & Copin, Y. (2003). Adaptive spatial binning of integral-field spectroscopic data using Voronoi tessellations. *Monthly Notices of the Royal Astronomical Society*, 342(2):345–354.
- Cappellari, M. et al. (2007). The SAURON project - X. The orbital anisotropy of elliptical and lenticular galaxies: revisiting the $(V/\sigma, \epsilon)$ diagram with integral-field stellar kinematics. *Monthly Notices of the Royal Astronomical Society*, 379(2):418–444.
- Cappellari, M. et al. (2011). The ATLAS^{3D} project - I. A volume-limited sample of 260 nearby early-type galaxies: science goals and selection criteria. *Monthly Notices of the Royal Astronomical Society*, 413:813–836.
- Carollo, C. M. et al. (1997). Ellipticals with Kinematically Distinct Cores: V - I Color Images with WPFC2. *The Astrophysical Journal*, 481(2):710–734.
- Chandrasekhar, S. (1943). Dynamical Friction. I. General Considerations: the Coefficient of Dynamical Friction. *The Astrophysical Journal*, 97:255.
- Davies, R. L. et al. (1983). The kinematic properties of faint elliptical galaxies. *The Astrophysical Journal*, 266:41–57.
- de Ruiter, H. R. et al. (2005). Are radio galaxies and quiescent galaxies different? Results from the analysis of HST brightness profiles. *Astronomy and Astrophysics*, 439(2):487–496.
- de Vaucouleurs, G. (1948). Recherches sur les Nebuleuses Extragalactiques. *Annales d'Astrophysique*, 11:247.
- Dehnen, W. (1993). A Family of Potential-Density Pairs for Spherical Galaxies and Bulges. *Monthly Notices of the Royal Astronomical Society*, 265:250.
- Dullo, B. T. & Graham, A. W. (2012). Sizing up Partially Depleted Galaxy Cores. *The Astrophysical Journal*, 755(2):163.
- Dullo, B. T. & Graham, A. W. (2014). Depleted cores, multicomponent fits, and structural parameter relations for luminous early-type galaxies. *Monthly Notices of the Royal Astronomical Society*, 444(3):2700–2722.

- Emsellem, E. et al. (2004). The SAURON project - III. Integral-field absorption-line kinematics of 48 elliptical and lenticular galaxies. *Monthly Notices of the Royal Astronomical Society*, 352:721–743.
- Emsellem, E. et al. (2007). The SAURON project - IX. A kinematic classification for early-type galaxies. *Monthly Notices of the Royal Astronomical Society*, 379(2):401–417.
- Emsellem, E. et al. (2011). The ATLAS^{3D} project - III. A census of the stellar angular momentum within the effective radius of early-type galaxies: unveiling the distribution of fast and slow rotators. *Monthly Notices of the Royal Astronomical Society*, 414:888–912.
- Faber, S. M. et al. (1997). The Centers of Early-Type Galaxies with HST. IV. Central Parameter Relations. *The Astronomical Journal*, 114:1771.
- Fabian, A. C. (2012). Observational Evidence of Active Galactic Nuclei Feedback. *Annual Review of Astronomy and Astrophysics*, 50:455–489.
- Ferrarese, L. & Ford, H. (2005). Supermassive Black Holes in Galactic Nuclei: Past, Present and Future Research. *Space Science Reviews*, 116(3-4):523–624.
- Ferrarese, L. & Merritt, D. (2000). A Fundamental Relation between Supermassive Black Holes and Their Host Galaxies. *The Astrophysical Journal*, 539(1):L9–L12.
- Gerhard, O. et al. (1998). Breaking the degeneracy between anisotropy and mass: the dark halo of the E0 galaxy NGC6703. *Monthly Notices of the Royal Astronomical Society*, 295(1):197–215.
- Gerhard, O. E. (1993). Line-of-sight velocity profiles in spherical galaxies: breaking the degeneracy between anisotropy and mass. *Monthly Notices of the Royal Astronomical Society*, 265:213.
- Goulaud, C. F. et al. (2018). The MASSIVE Survey. IX. Photometric Analysis of 35 High-mass Early-type Galaxies with HST WFC3/IR. *The Astrophysical Journal*, 856(1):11.
- Gragg, W. B. (1965). On Extrapolation Algorithms for Ordinary Initial Value Problems. *SIAM Journal on Numerical Analysis*, 2(3):384–403.
- Graham, A. W. (2004). Core Depletion from Coalescing Supermassive Black Holes. *The Astrophysical Journal Letters*, 613(1):L33–L36.

- Graham, A. W. et al. (2003). A New Empirical Model for the Structural Analysis of Early-Type Galaxies, and A Critical Review of the Nuker Model. *The Astronomical Journal*, 125(6):2951–2963.
- Gualandris, A. et al. (2017). Collisionless loss-cone refilling: there is no final parsec problem. *Monthly Notices of the Royal Astronomical Society*, 464(2):2301–2310.
- Hellström, C. & Mikkola, S. (2010). Explicit algorithmic regularization in the few-body problem for velocity-dependent perturbations. *Celestial Mechanics and Dynamical Astronomy*, 106(2):143–156.
- Hernquist, L. (1990). An Analytical Model for Spherical Galaxies and Bulges. *The Astrophysical Journal*, 356:359.
- Hopkins, P. F. et al. (2008). Dissipation and Extra Light in Galactic Nuclei. I. Gas-Rich Merger Remnants. *The Astrophysical Journal*, 679(1):156–181.
- Hubble, E. P. (1926). Extragalactic nebulae. *The Astrophysical Journal*, 64:321–369.
- Hubble, E. P. (1936). *Realm of the Nebulae*. Yale University Press.
- Jaffe, W. (1983). A simple model for the distribution of light in spherical galaxies. *Monthly Notices of the Royal Astronomical Society*, 202:995–999.
- Kidder, L. E. (1995). Coalescing binary systems of compact objects to (post)^{5/2}-Newtonian order. V. Spin effects. *Physical Review D*, 52(2):821–847.
- Kormendy, J. & Bender, R. (1999). The Double Nucleus and Central Black Hole of M31. *The Astrophysical Journal*, 522(2):772–792.
- Kormendy, J. et al. (2009). Structure and Formation of Elliptical and Spheroidal Galaxies. *The Astrophysical Journal Supplement Series*, 182(1):216–309.
- Krajnović, D. et al. (2008). The SAURON project - XII. Kinematic substructures in early-type galaxies: evidence for discs in fast rotators. *Monthly Notices of the Royal Astronomical Society*, 390(1):93–117.
- Krajnović, D. et al. (2011). The ATLAS^{3D} project - II. Morphologies, kinematic features and alignment between photometric and kinematic axes of early-type galaxies. *Monthly Notices of the Royal Astronomical Society*, 414(4):2923–2949.

- Krajnović, D. et al. (2013). The ATLAS^{3D} Project - XXIII. Angular momentum and nuclear surface brightness profiles. *Monthly Notices of the Royal Astronomical Society*, 433(4):2812–2839.
- Lauer, T. R. et al. (1995). The Centers of Early-Type Galaxies with HST.I.An Observational Survey. *The Astronomical Journal*, 110:2622.
- Lauer, T. R. et al. (2007a). The Centers of Early-Type Galaxies with Hubble Space Telescope. VI. Bimodal Central Surface Brightness Profiles. *The Astrophysical Journal*, 664(1):226–256.
- Lauer, T. R. et al. (2007b). The Masses of Nuclear Black Holes in Luminous Elliptical Galaxies and Implications for the Space Density of the Most Massive Black Holes. *The Astrophysical Journal*, 662(2):808–834.
- Ma, C.-P. et al. (2014). The MASSIVE Survey. I. A Volume-limited Integral-field Spectroscopic Study of the Most Massive Early-type Galaxies within 108 Mpc. *The Astrophysical Journal*, 795(2):158.
- Marconi, A. & Hunt, L. K. (2003). The Relation between Black Hole Mass, Bulge Mass, and Near-Infrared Luminosity. *The Astrophysical Journal Letters*, 589(1):L21–L24.
- Merritt, D. (2006). Mass Deficits, Stalling Radii, and the Merger Histories of Elliptical Galaxies. *The Astrophysical Journal*, 648(2):976–986.
- Merritt, D. (2013). *Dynamics and Evolution of Galactic Nuclei*. Princeton University Press.
- Mikkola, S. & Merritt, D. (2008). Implementing Few-Body Algorithmic Regularization with Post-Newtonian Terms. *The Astronomical Journal*, 135(6):2398–2405.
- Milosavljević, M. et al. (2002). Galaxy cores as relics of black hole mergers. *Monthly Notices of the Royal Astronomical Society*, 331(4):L51–L55.
- Milosavljević, M. & Merritt, D. (2001). Formation of Galactic Nuclei. *The Astrophysical Journal*, 563(1):34–62.
- Milosavljević, M. & Merritt, D. (2003). The Final Parsec Problem. In Centrella, J. M., editor, *The Astrophysics of Gravitational Wave Sources*, volume 686 of *American Institute of Physics Conference Series*, pages 201–210.

- Mo, H., van den Bosch, F. C., & White, S. (2010). *Galaxy Formation and Evolution*. Cambridge University Press.
- Monaghan, J. J. & Lattanzio, J. C. (1985). A refined particle method for astrophysical problems. *Astronomy and Astrophysics*, 149(1):135–143.
- Mora, T. & Will, C. M. (2004). Post-Newtonian diagnostic of quasiequilibrium binary configurations of compact objects. *Physical Review D*, 69(10):104021.
- Naab, T. & Burkert, A. (2003). Statistical Properties of Collisionless Equal- and Unequal-Mass Merger Remnants of Disk Galaxies. *The Astrophysical Journal*, 597(2):893–906.
- Naab, T., Johansson, P. H., & Ostriker, J. P. (2009). Minor Mergers and the Size Evolution of Elliptical Galaxies. *The Astrophysical Journal Letters*, 699(2):L178–L182.
- Naab, T., Khochfar, S., & Burkert, A. (2006). Properties of Early-Type, Dry Galaxy Mergers and the Origin of Massive Elliptical Galaxies. *The Astrophysical Journal Letters*, 636(2):L81–L84.
- Nelder, J. A. & Mead, R. (1965). A Simplex Method for Function Minimization. *The Computer Journal*, 7(4):308–313.
- Oser, L. et al. (2010). The Two Phases of Galaxy Formation. *The Astrophysical Journal*, 725(2):2312–2323.
- Peters, P. C. (1964). Gravitational Radiation and the Motion of Two Point Masses. *Physical Review*, 136(4B):1224–1232.
- Pihajoki, P. (2015). Explicit methods in extended phase space for inseparable Hamiltonian problems. *Celestial Mechanics and Dynamical Astronomy*, 121(3):211–231.
- Quinlan, G. D. & Hernquist, L. (1997). The dynamical evolution of massive black hole binaries — II. Self-consistent N-body integrations. *New Astronomy*, 2(6):533–554.
- Rantala, A. et al. (2017). Post-Newtonian Dynamical Modeling of Supermassive Black Holes in Galactic-scale Simulations. *The Astrophysical Journal*, 840(1):53.
- Rantala, A. et al. (2018). The Formation of Extremely Diffuse Galaxy Cores by Merging Supermassive Black Holes. *The Astrophysical Journal*, 864(2):113.

- Rantala, A. et al. (2019). The Simultaneous Formation of Cored, Tangentially Biased, and Kinematically Decoupled Centers in Massive Early-type Galaxies. *The Astrophysical Journal Letters*, 872(2):L17.
- Rodriguez, C. et al. (2006). A Compact Supermassive Binary Black Hole System. *The Astrophysical Journal*, 646(1):49–60.
- Rusli, S. P. et al. (2013a). Depleted Galaxy Cores and Dynamical Black Hole Masses. *The Astronomical Journal*, 146(6):160.
- Rusli, S. P. et al. (2013b). The Influence of Dark Matter Halos on Dynamical Estimates of Black Hole Mass: 10 New Measurements for High- σ Early-type Galaxies. *The Astronomical Journal*, 146(3):45.
- Saglia, R. P. et al. (2016). The SINFONI Black Hole Survey: The Black Hole Fundamental Plane Revisited and the Paths of (Co)evolution of Supermassive Black Holes and Bulges. *The Astrophysical Journal*, 818(1):47.
- Soltan, A. (1982). Masses of quasars. *Monthly Notices of the Royal Astronomical Society*, 200:115–122.
- Springel, V. (2005). The cosmological simulation code GADGET-2. *Monthly Notices of the Royal Astronomical Society*, 364(4):1105–1134.
- Springel, V., Yoshida, N., & White, S. D. M. (2001). GADGET: a code for collisionless and gasdynamical cosmological simulations. *New Astronomy*, 6(2):79–117.
- Statler, T. S. (1987). Self-consistent Models of Perfect Triaxial Galaxies. *The Astrophysical Journal*, 321:113.
- Sérsic, J. L. (1968). *Atlas de Galaxias Australes*. Observatorio Astronomico, Universidad Nacional de Cordoba.
- Thomas, J. et al. (2007). Dynamical modelling of luminous and dark matter in 17 Coma early-type galaxies. *Monthly Notices of the Royal Astronomical Society*, 382(2):657–684.
- Thomas, J. et al. (2014). The Dynamical Fingerprint of Core Scouring in Massive Elliptical Galaxies. *The Astrophysical Journal*, 782(1):39.
- Thomas, J. et al. (2016). A 17-billion-solar-mass black hole in a group galaxy with a diffuse core. *Nature*, 532(7599):340–342.

- van der Marel, R. P. & Franx, M. (1993). A New Method for the Identification of Non-Gaussian Line Profiles in Elliptical Galaxies. *The Astrophysical Journal*, 407:525.
- Veale, M. et al. (2017). The MASSIVE Survey - V. Spatially resolved stellar angular momentum, velocity dispersion, and higher moments of the 41 most massive local early-type galaxies. *Monthly Notices of the Royal Astronomical Society*, 464(1):356–384.
- Veale, M. et al. (2018). The MASSIVE survey - VIII. Stellar velocity dispersion profiles and environmental dependence of early-type galaxies. *Monthly Notices of the Royal Astronomical Society*, 473(4):5446–5467.
- Young, P. (1980). Numerical models of star clusters with a central black hole. I - Adiabatic models. *The Astrophysical Journal*, 242:1232–1237.
- Zemp, M. et al. (2011). On Determining the Shape of Matter Distributions. *The Astrophysical Journal Supplement*, 197(2):30.